Resonance Raman Studies of Oxygenated Forms of Myoglobin and CYP2B4 and Their Mutants

Ying Wang
Marquette University

RESONANCE RAMAN STUDIES OF OXYGENATED FORMS OF MYOGLOBIN AND CYP2B4 AND THEIR MUTANTS

By

Ying Wang, B.Sc., M.S.

A Dissertation submitted to Faculty of the Graduate School,
Marquette University,
in Partial Fulfillment of the Requirements for
the Degree of Doctor of Philosophy

Milwaukee, Wisconsin

August 2016

ABSTRACT

RESONANCE RAMAN STUDIES OF OXYGENATED FORMS OF MYOGLOBIN AND CYP2B4 AND THEIR MUTANTS

Ying Wang, B.Sc., M.S.

Marquette University, 2016

Important oxidative heme enzymes use hydrogen peroxide or activate molecular oxygen to generate highly reactive peroxo-, hydroperoxo- and feryl intermediates resulting from heterolytic O-O bond cleavage. Members of the cytochrome P450 superfamily catalyze difficult chemical transformations, including hydroxylations and C-C bond cleavage reactions. In mammals, these enzymes function to reliably produce important steroids with the required high degree of structural precision. On the other hand, certain other mammalian P450s serve a different role, efficiently metabolizing xenobiotics, including pharmaceuticals and environmental pollutants. Though so important, the precise mechanisms involved in such transformations are incompletely understood, because of difficulties in structurally characterizing the fleeting intermediates. This dissertation exploits a unique combination of techniques to address this issue, cryoradiolytically reducing the relatively stable dioxgen adducts to generate and trap the reactive species at low temperatures, followed by resonance Raman (rR) spectroscopic interrogation to effectively characterize key molecular fragments within these crucial intermediates. One essential goal of this work is to evaluate the rR spectral response to structural variations of such species employing an accessible model that can be systematically manipulated. Myoglobin (Mb) serves this purpose, because its readily accessible site-directed mutants are useful for investigating the effects of heme site environment on the structure and function of heme proteins. In the present work, horse heart Mb and 6 site-directed mutants are employed to study the effects of active site environment on the structure and behavior of the Fe-O-O and Fe=O fragments of the peroxo-, hydroperoxo- and ferryl forms that can arise. In addition, successful efforts were made to structurally define the Fe-O-O fragment of the dioxgen adduct of the mammalian drug-metabolizing Cytochrome P450 2B4 (CYP2B4) and explore its interaction with cytochromeb_5. Much effort in this work was devoted to developing effective strategies to trap the especially unstable dioxygen adduct of CYP2B4. Corresponding studies of two key CYP2B4 mutants, E301Q and F429H, were also conducted, where the former mutation alters distal pocket interactions, while the F429H variant alters the strength of the trans-axial thiolate linkage that can modify the strength of the Fe-O and O-O linkages of the Fe-O-O fragments.

ACKNOWLEDGEMENTS

Ying Wang, B.Sc., M.S.

My heartfelt thanks go to Professor James R. Kincaid for his continued mentorship throughout my time in his research group. I will forever be grateful for his guidance and his major contribution to my career development. I would like to also express my appreciation to my Committee members, Professors Daniel S. Sem, Michael. D. Ryan and Adam Fiedler for useful discussions throughout my studies, writing of this dissertation and being flexible in time for my research meeting, annual review and thesis defense. I am so grateful to Professor Michael, D. Ryan for kindly offering his UV-vis instrument in my research. Also I am thankful to Dr. James Anderson and Dr. Daniel S. Sem for their help during the production of proteins and offering me to use their equipment in their lab. I would also like to thank Dr. Piotr Mak for his guidance, help, his patience and time during my research time. Without his help, I could not finish my research. My sincere gratitude is also extended to my group members, Drs. K. Czarnecki and P. Mak for introducing me to resonance Raman spectroscopy and continued technical advice and support. Also thanks to my peer group members, Qianhong Zhu, Remigio Usai, Yinlin Liu, for their help.

Finally, I would like to express my heartfelt thanks to my husband for his unconditional support and help for my academic success. Also I would like to thank my little sons for their company during all my time in Milwaukee and their love. I also would like to thank my family members and friends for believing in me and encouraging me continuously.

TABLE OF CONTENTS

LIST OF TABLES

LIST OF FIGURES

Chapter 1. General Introduction

1.1 General introduction to heme proteins

Heme proteins are one of the most versatile groups of proteins existing in living cells, performing a wide range of functions that are vital to aerobic life.[1-5] They are metalloproteins containing a heme prosthetic group, the most commonly encountered being the protoheme group shown in Figure 1, which is bound to the protein via axial ligands provided by the protein; these are usually histidyl imidazole, cysteine thiolate or sometimes the phenolate groups of tyrosine. The aromatic macrocycle of the heme, containing four pyrrole rings, is called a porphyrin. Heme iron can be five or six coordinated, with five coordinate forms typically being high spin (HS) and six coordinate forms usually being low spin (LS). For instance, in globins, the fifth (or proximal) heme-iron ligand is the imidazole ring of a histidine residue and the trans-axial heme-iron position is available for dioxygen molecule binding. [1].

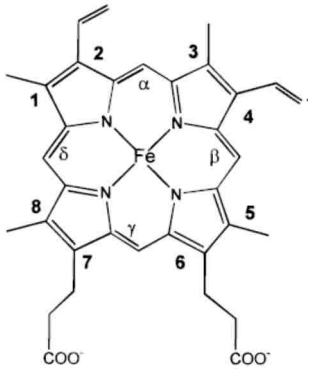

Figure 1.1.1 Structure of protoheme IX (iron protoporphyrin IX, heme b) [4]

The functions of heme proteins vary from case to case. Based on the different functions, the heme proteins can be further classified into several categories. A few of those of interest in this work are discussed below.

1.1.1 Globins

Hemoglobin and myoglobin cooperate in the transport and storage of oxygen in vertebrates. The concentration of hemoglobin is very high in red blood cells and myoglobin is plentiful in aerobic muscle tissue. As shown in Figure1.1.1.1, the O_2 binding affinity of hemoglobin in muscle and lung is more related to the O_2 partial pressure than that of Myoglobin. The tetrameric hemoglobin molecule can cooperatively bind O_2 in areas of high oxygen concentration so it gets nearly saturated in the lungs. The blood stream then transports oxy-hemoglobin to areas of low oxygen concentration in respiring tissues where it is released and the high affinity myoglobin can bind and store it until required for oxidative phosphorylation [5, 6].

Sperm whale myoglobin and horse hemoglobin were the first two protein structures determined to high resolution by X-ray crystallography and both have long been used as models for many types of studies of protein structure and function and for testing various new biophysical methods, as is the case in this dissertation, where myoglobins are being used to help explore the structural sensitivity of resonance Raman spectroscopy for studies of reactive enzymatic intermediates. [2, 3, 7].

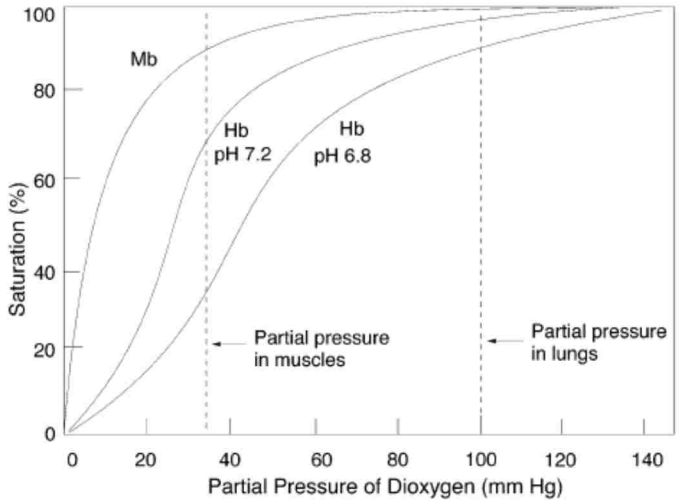

Figure 1.1.1.1 Equilibrium fraction of oxyMb and oxyHb as a function of the O_2 partial pressure. The O_2 affinity of Hb is subject to both homoallosteric control (i.e., the affinity depends on the O_2 concentration, or partial pressure) and heteroallosteric control (the effect of H^+ is shown as an example) [6].

1.1.2. Signal proteins

A particular heme signalling protein, soluble gyanylyl cyclase (sGC) is interesting to mention here, because comparing it to myoglobin (which is studied in this dissertation) allows one to understand how protein structure can affect heme properties and function so strongly. Like myoglobin, this protein has a protoheme prosthetic group that is bound by a single histidine residue. What is interesting is that it is also a ferrous protein that binds NO, but not O_2, even when the concentration of NO is very low and the concentration of O_2 is very high. [8. 9]. Basically, this is because there is no H-bonding residue in the distal pocket of sGC to stabilize O_2 binding; myoglobin and hemoglobin have a distal pocket histidine for this purpose. It is also important that the protein chain in sGC has an overall structure that gives a much weaker bond between the iron and the

proximal histidine; as will be seen later, the ν(Fe-N) stretching mode (of the proximal histidine) in myoglobin occurs at ~220 cm^{-1}, but the same bond for sGC has a ν(Fe-N) frequency of only 205 cm^{-1}. This bond is so weak that when sGC binds NO, the trans-axial histidine ligation to heme iron is broken, giving a five coordinate ferrous NO adduct. **[10, 11]** This breaking of the Fe-N(histidine) bond causes a big change in proximal side structure and this change is transmitted through the protein to a remote region and causes activation of enzymatic activity at that site that produces cGMP, another neurotransmitter [12, 13]. Figure 1.1.2.1 shows how the sGC catalyzes guanosine 5P-triphosphate (GTP) to cyclic guanosine 3P,5P-monophosphate (cGMP) [14].

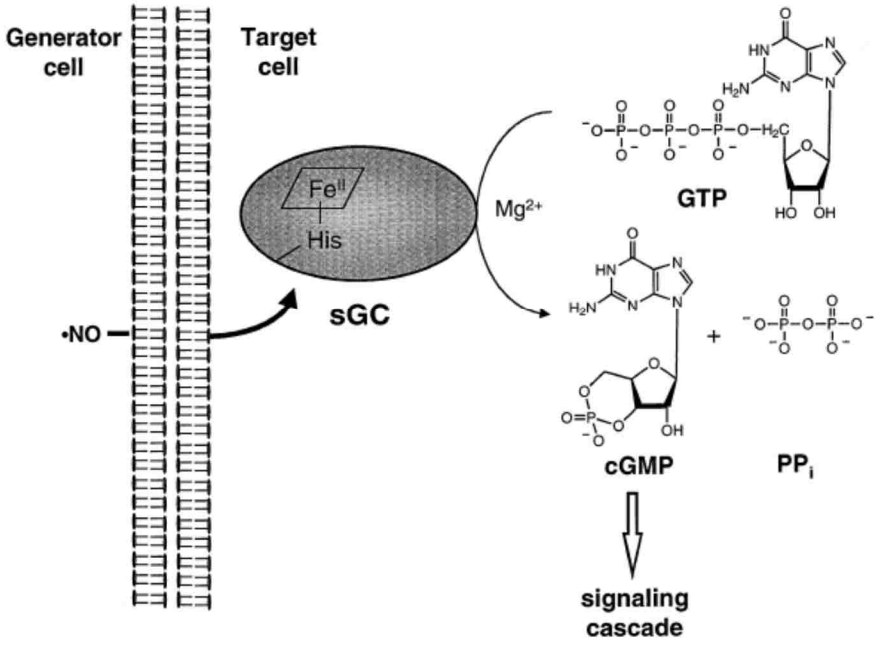

Figure 1.1.2.1 The guanylate cyclase reaction and NO signal transduction [14].

1.1.3. Cytochromes P450

The other type of enzymes being studied in this dissertation are the cytochromes P450 (also designated CYPs). Specifically, the one being targeted is designated CYP2B4 and will be thoroughly discussed in Chapter 3. The cytochromes P450 (CYP 450) are typical heme-containing monooxygenases, meaning that their function is to utilize molecular oxygen to oxygenate susceptible substrates, incorporating only one atom of the dioxygen molecule into the substrate. [15-17] Like the globins and sGC proteins mentioned above, and many other heme proteins, the prosthetic group of CYPs is a protoheme. However, an important difference is that the proximal ligand in CYPs is a thiolate provided by a strictly conserved cysteine residue [18, 19]. This axial thiolate ligation changes the chemical properties of the protoheme group relative to myoglobin and other histidine ligated heme proteins making it better suited for the difficult chemical transformation conducted by these enzymes. There are also changes in the spectral properties compared to histidine ligated proteins. For example, the reduced protein exhibits a maximum electronic absorption band (the Soret band) at 450nm upon formation of the ferrous CO adduct, whereas ferrous CO adducts of histidine-ligated heme proteins usually appear near 420 nm. [19-23] It was the observation of such spectra in solutions of cell extracts containing P450s when they were discovered that gave this group of proteins its name. [24]

The cytochromes P450 serve many functions in living systems. Mammalian P450s include two big categories: membrane bound and incorporated P450s. In mammals they are involved in mammalian steroid biosynthesis pathways and in drug metabolism [25]. The size of active site in steroidogenic P450s is much smaller than that in drug

metabolism P450s. And the structure of drug metabolism P450s is more “flexible” than steroidogenic P450s. This is necessary, because each drug metabolizing P450 must work on many substrates (drugs or pollutants). In general, drug metabolizing P450s can effect multiple and relatively non-specific hydroxylations on a bound substrate. Drug metabolism P450s metabolism are most of the drugs in the market [26, 27]. For example the size of active site in CYP3A4 is 1386 Å, and CYP3A4 can metabolizes around 50% of the drug [28].

However, steroidogenic P450s have a higher specificity so that they only bind one substrate molecule at one time and can effect highly regio- and stereo-specific hydroxylations or other oxidative transformations on the single natural substrate. In fact, steroidogenic P450s typically can process a given substrate undergoing multiple cycles causing larger structural changes, such as C-C bind cleavage; e.g., CYP17. As shown in Figure 1.1.3.1, CPY 17 can catalyze the cytochrome – *P*-450 hydroxylation reaction at position 17α – of the pregnene nucleus, with the second reaction causing loss of acetic acid [29].

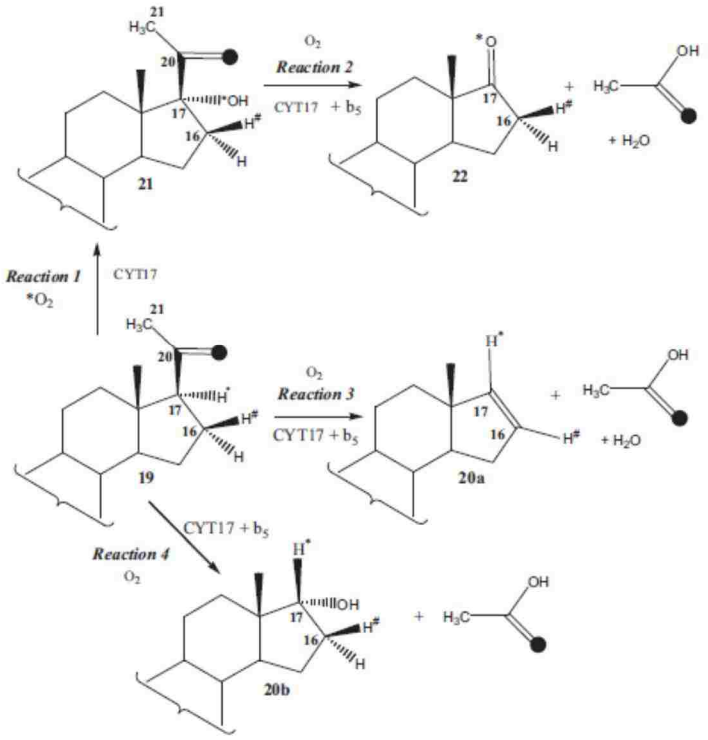

Figure 1.1.3.1 Reaction catalyze by CPY17 [29]

The accepted catalytic cycle of P450 is shown Figure 1.1.3.2. In this figure, the porphyrin macrocycle is symbolized by the two bold lines flanking the iron. The resting state of the enzyme is ferric complex and its axial ligand is water, from a cluster of water molecules present in the substrate-free form. This complex is low-spin (LS). The entrance of substrate into the protein pocket disrupts the water cluster, removing the bound axial water ligand, giving a 5-coordinate HS ferric heme (5cHS). This configuration is easier to reduce than the LS form, facilitating electron transfer from a bound partner reductase. [30]

This relatively electron rich five-coordinate ferrous heme group readily binds dioxygen [31]. The spectral data show this Fe(II)-O_2 complex is most reasonably named as a ferric-superoxide species, Fe(III)-O-O^- [32,33]. The ferric-superoxide protein gets the second electron via electron transfer from a reductase. The product of this step is a

negatively charged ferric peroxo group formulated Fe(III)-O-O^{2-}. A very quick protonation happens on ferric peroxo species by local transferred proton from water or surrounding amino acid side chain. Then it becomes ferric hydroperoxo Fe(III)-(O-OH^-). A second protonation happens on the distal oxygen atom of ferric hydroperoxo species, promoting O-O bond cleavage. This step produces a high-valent iron-oxo complex, Compound I, which is a strong oxidant. This Fe(IV) oxo species has the second oxidizing equivalent centered on a heme based π-cation radical localized over the porphyrin macrocycle [32]. The long untrapped cytochrome P450 Compound I has recently been made and characterized by M. T. Green [34].

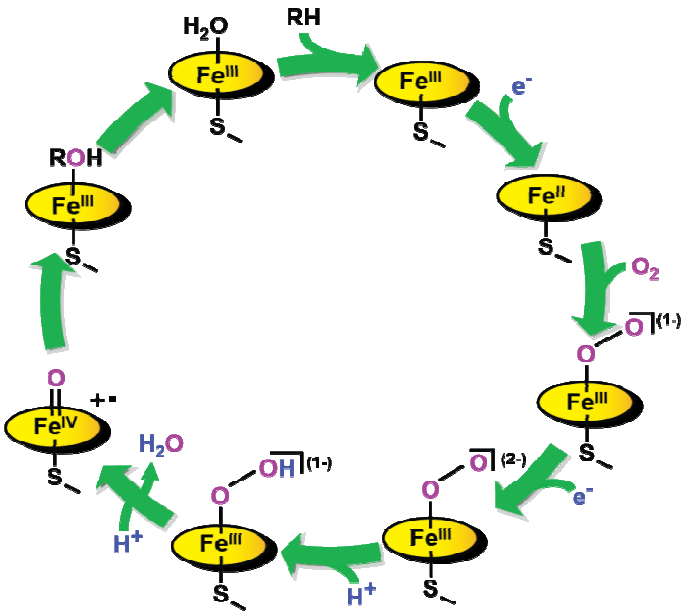

Figure 1.1.3.2. The catalytic mechanism of P450

1.2 Cryoradiolysis studies

1.2.1 Introduction to cryoradiolysis

Cryoradiolysis is a method for studying intermediates in chemical and biochemical reactions that are generated by electron transfer, but quickly disappear owing to uncontrolled subsequent protonation reactions. Irradiation with γ-rays, often from a ^{60}Co source, generates free electrons in frozen solutions containing certain organic solvents, such as glycerol and ethylene glycol.

As we know, ionizing radiation can initiate the chemical reaction. For example, the electron of the solvent radiolysis can make the reaction in the matrix start. Most popular radiation ray is gamma-ray in different source like ^{60}Co source. For many chemical reactions, the rate of reaction drop dramatically when the temperature becomes very low. If only the electrons are allowed to transfer but restrict the proton transfer, the intermediates in cytochrome P450 catalytic cycle can be trapped. Thus, cryoradiolysis combined with other measurement can be employed to study the active intermediates like peroxo-, hydroperoxo-, or maybe even compound I [35].

The concept of cryoradiolysis is shown as in Figure 1.2.1.1. The first step is to get stable oxy-complex so the slow spectroscopic and structural methods can be applied on the sample. The heme protein is prepared in a buffer (H_2O or D_2O) containing glycerol, which gets ionized to free electrons and organic radicals, and can supply electron during the irradiation. The heme protein can be reduced by using fresh dithionite to form the ferrous form. Then oxygen gas is bubbled through the solution and quickly frozen in liquid N_2 to make sure the sample does not auto-oxidize. The ferric-superoxide heme

protein is prepared by submersing the sample tube in cold bath which is very important to stabilize the oxy-complex.

After that, the oxy-protein can get one electron from irradiated glycerol by irradiating the sample under ^{60}Co gamma ray source at 77K. The source is available at Notre Dame Radiation Laboratory. At this step, ferric peroxo-heme protein is formed via migration of electrons at 77K, while other species, including protons, are not so mobile. The resonance Raman spectrum of this trapped peroxo- species can be collected at this point.

When the peroxo-protein is annealed at higher different temperature the ferric hydroperoxo complex can be generated at this point since proton is allowed to migrate. Using a combination of cryoradiolysis with rR or EPR, the change from peroxo- to hydroperoxo species can be monitored. Ideally, the next step is to trap Compound I. However, Compound I will be formed, but this species is too reactive to be seen yet [36].

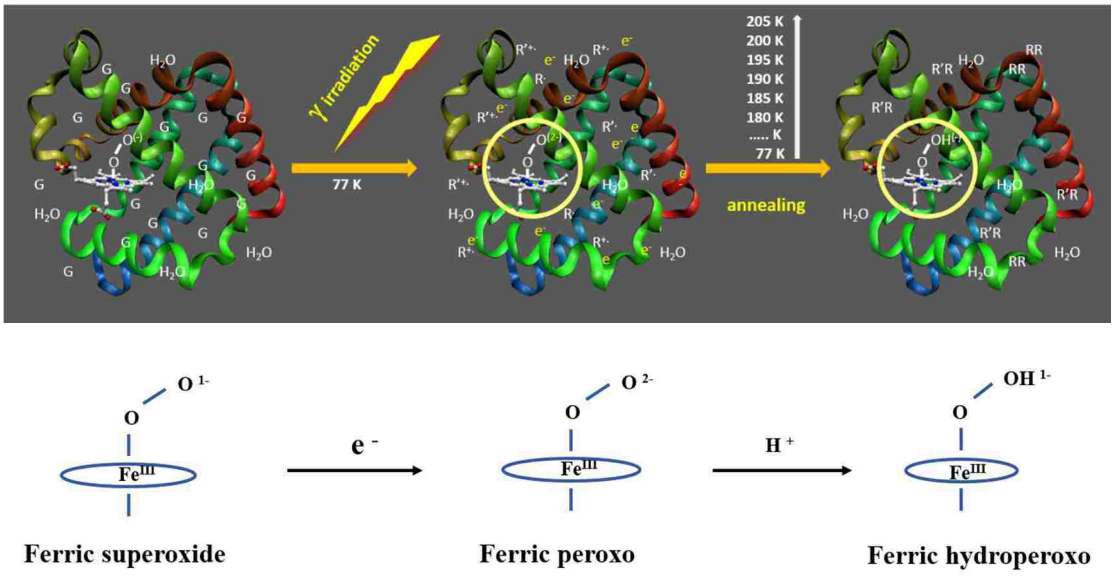

Figure 1.2.1.1 Process of cryoradiolysis and annealing to generate intermediates at different stage

1.2.2 Cryoradiolysis studies of heme proteins

The cryoradiolysis method was first applied for the study of oxy-heme protein by Martyn Symons in 1980s [37]. The key point of cryoradiolysis method is coupling with powerful spectroscopic probes to obtain the new structural dynamic processes in the catalytic pathways of oxidative heme enzymes. Hoffman and coworkers use cryoradiolysis method to study many oxygenated heme proteins, employing EPR and ENDOR spectroscopies. They studied the enzymatic cycles of heme monooxygenase, including peroxidases, catalases, cytochrome P450, nitric oxide synthases (NOS), with combination of cryoreduction/annealing and magnetic spectroscopy approaches, like EPR/ENDOR to help identify the oxidizing species involved in conversion of bound substrate to product [38-43]. However, one of the limitations of these magnetic spectroscopic methods is that only paramagnetic intermediates can be effectively monitored, whereas as will be seen in this document, rR spectroscopy can probe virtually all of the intermediates encountered in most heme enzyme reaction cycles [44, 45].

1.3 Raman Spectroscopy

1.3.1 Basic concepts of Raman spectroscopy

1.3.1.1 Normal Raman Effect

Indian physicist C.V. Raman was awarded the 1930 Nobel Prize for the discovering the Raman effect. When an incident beam passes through a transparent medium, a small fraction of the radiation will be scattered in all directions. As shown in Figure 1.3.1.1,

most of the photons scattered from interacting molecules have the same energy as the incident photons without losing or gaining energy from the molecule, giving rise to an intense Rayleigh scattered band with the same frequency as the incident band. Rayleigh scattering is more probable than other scattering. The rest of the scattered photons, which have different energies than the incident photons, are called Raman scattering. They include two kinds: the lower energy ("Stokes" Raman bands) and the higher energy ("anti-Stokes" Raman bands). The frequencies of the Raman peaks are determined by the energies of the vibrational modes of the molecule and are sensitive to molecular structure. Thus, the Raman spectrum, like IR spectra, can be used to characterize the structure of molecules. Thus, the type of information that can be obtained from the Raman Effect is the same as that obtained by direct *absorption* of energy in the infrared (IR) region. There the molecules absorb an IR photon whose energy matches that of an allowed vibrational transition, promoting the molecule to an excited vibrational level. This is the physical principle of IR spectroscopy. Therefore, in the IR and Raman spectra, the peaks of a given compound are at the same frequency, although the intensities may be different [46].

The Raman Effect occurs by scattering of photons. The energy for promotion of the molecule to an excited vibrational state is not absorbed, but transferred from the high energy photon to the molecule, with the scattered photon having an amount of energy corresponding to the difference in energy of the incident photon and the energy of the vibrational transition; i.e., ν_0-ν_i. If the incident photon encounters a molecule already in a vibrationally excited state, the photon can gain energy of that vibrational excited state to give a higher energy photon; i.e., ν_0+ν_i. The probability for the transfer of energy depends on the deformability of the electron cloud of the molecule, referred to as the polarizability,

α. The symmetric bond stretching vibrations are usually strong in the Raman spectra, because as the molecule expands during the stretching motion, the electronic cloud becomes more diffuse; i.e., the deformability (α) of the cloud changes. Antisymmetric stretching vibrations and deformation modes usually dominate the IR spectra. Since the physical mechanisms involved in Raman and IR spectroscopy are different, the intensities and selection rules of IR and Raman peaks are different [47].

Another important point is that Raman spectroscopy has one advantage over IR for studying materials dissolved in water, because water strongly absorbs IR radiation over a fairly wide spread of wavelengths; i.e., it covers up regions of the spectrum, eliminating regions of the spectrum where structure sensitive bands of the samples appear. Water is a very weak Raman scatterer, so the whole range of structure sensitive bands of the sample can be seen; this is a great advantage for studying biological samples, as is being done here.

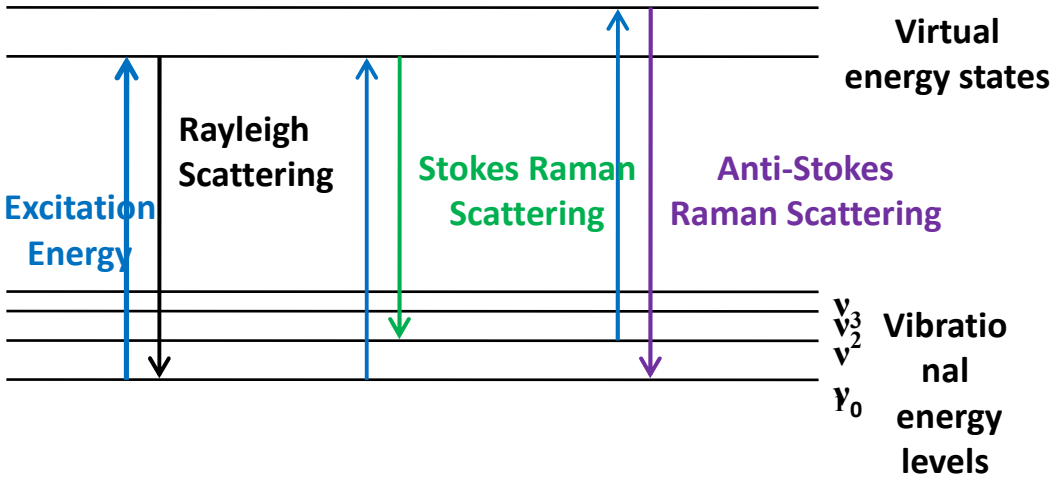

Figure 1.3.1.1 Schematic representation of the Raman Effect

1.3.1.2 Resonance Raman spectroscopy

Though Raman offers advantages over IR for work in aqueous solutions, a big disadvantage of "normal" Raman spectroscopy is that it is a very weak effect; the probability for Raman scattering is very low. For example, to acquire a high quality Raman spectrum of glucose in water, a concentration near 1M would probably be needed. However, if the molecules possess reasonably strong electronic absorption bands, there can be a very large increase in the probability of the scattering process, giving much stronger Raman scattered bands and enhancing sensitivity a lot. When the laser excitation line is in resonance with the allowed electronic transition of molecule, the Raman bands that are enhanced the most are those associated with vibrations that mirror the excited-state molecular distortion. The resonance enhancement allows the researchers to lower the concentration in samples from molar range to millimolar or micromolar range. Also, the laser beam can be focused to the spot and reduced the effective scattering volume to microliters.

A good example of great enhancement of RR for chromophoric group is shown in Figure 1.4 [47]. The target complex is tris-phenanthroline Fe(II) shown in 1.3.1.2 (A). As shown in 1.3.1.2 (B), the absorption spectrum exhibits a strong MLCT transition appearing around 515 nm. When the excitation line is far from the MLCT maximum, no matter the wavelength is bigger or smaller than the max MLCT transition, the signals from tris-phenanthroline Fe(II) complex are much weaker than those when the excitation line is close to max absorption band. For example, when the excitation is 647.1 nm, which is far from the MLCT maximum, the Raman spectrum is dominated by sulfate ion, SO_4^{2-}, with ν(S-O) at 981cm^{-1}. When the excitation line is closer to the MLCT maximum,

the characteristic modes of the coordinated ligand are increasing enhanced, dominating the spectrum even though the concentration of the complex is 1000 times less than that of the sulfate.

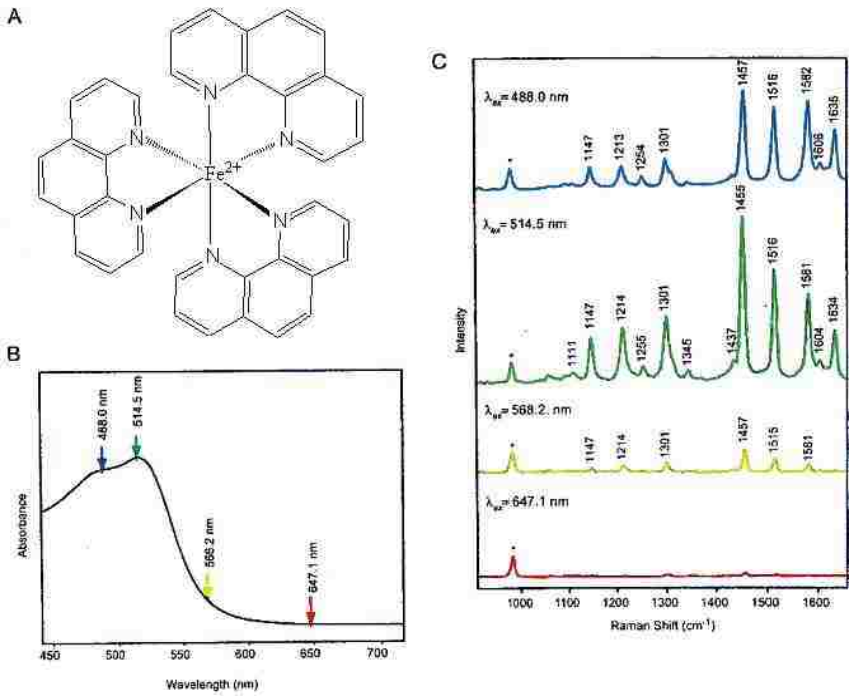

Figure 1.3.1.2 (A) structure of tris-phenanthroline Fe(II); (B) Absorption spectroscopy of tris-phenanthroline Fe(II); (C) Resonance Raman spectroscopy with different excitation laser lines [47]

1.3.2 Instrumentation

The instrumentation of Raman spectroscopy consists of a laser source, a sample illumination system, polychromator, and radiation transducer and computer data system, as shown in Figure 1.3.2.1. The most common and reliable sources are continuous wave (CW) gas lasers, like Argon and Krypton ion lasers. The helium-neon and helium-cadmium lasers are also very useful and popular at lower power levels [48, 49].

In order to avoid over-heating one spot by high power laser source and make sure the collected signals are from the whole sample, the sample tube is spinning in the Raman system. That equipment will allow to measure samples at different temperature all the time. The control of the sample temperature can be done by adding different liquid in the glass dewar. For example, the liquid nitrogen dewar is introduced into the system when the unstable species are measured like protein CYP2B4.

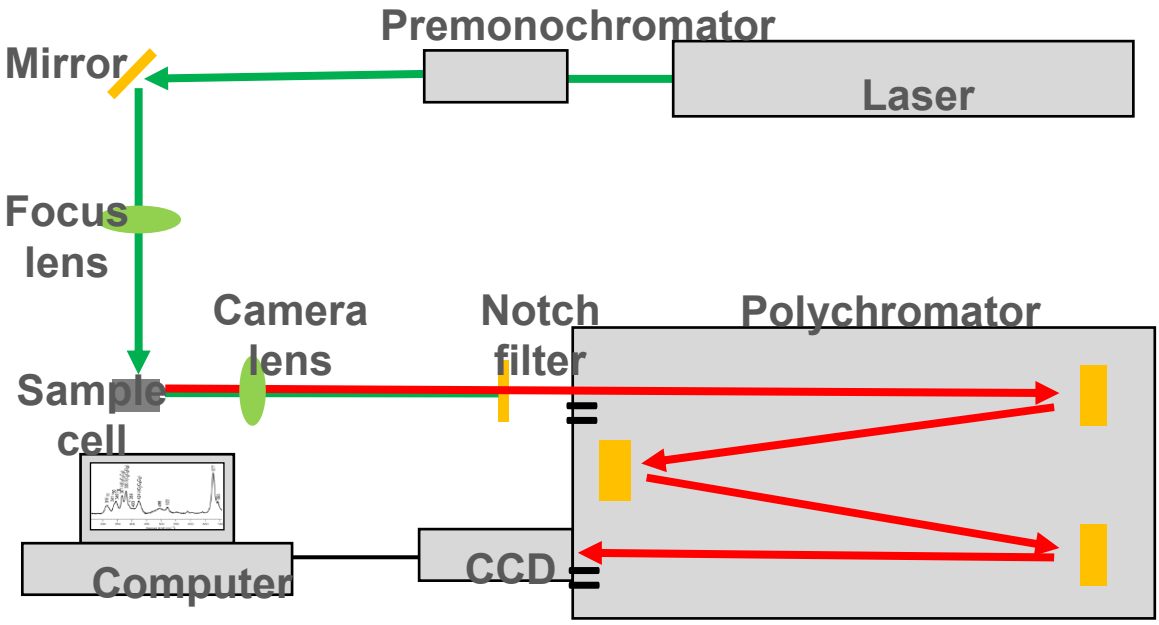

Figure 1.3.2.1. Diagram of a resonance Raman spectrometer

1.3.3 Resonance Raman spectroscopy and heme proteins

The heme groups in heme proteins are examples of molecules called metalloporphyrins. Metalloporphyrins are one of the most studied classes of molecules in the area of Raman spectroscopy. The first reason is about the aromatic macrocyclic structure of the heme group. The extended aromatic system of the porphyrin ring gives rise to two low-lying π-π^* electronic transitions. It is convenient to excite

metalloporphyrins with a visible laser. For instance, the vibrational frequencies changes in the Raman spectra are responsive to porphyrin geometry and electronic structure change; these effects can be examined selectively by changing the excitation wavelength. Moreover, the vibrational modes of the active site heme chromophore of heme proteins and their associated ligands can be selectively enhanced by exciting within the absorption spectral region of the heme chromophore. The vibrational modes of the non-absorbing polypeptide retain the much weaker scattering of the non-resonant event and are not detected above the spectral background. However, if one uses deep UV laser it is possible to selectively enhance aromatic amino acid groups, such as tyrosine, tryptophan and phenylalanine [50]. For example, in human hemoglobin, when the excitation line is in the UV laser near 220-280 nm, as shown in Figure 1.3.3.1, the Raman spectrum shows the information about the amino acid and protein structure. If the excitation line is just at Soret band which is the most intensive π-π^* transition, or close to Q band, the signals from the heme group are stronger than when other excitation line is applied [51]. So resonance Raman spectroscopy (RR) is characterized by enhanced detection and selection capabilities.

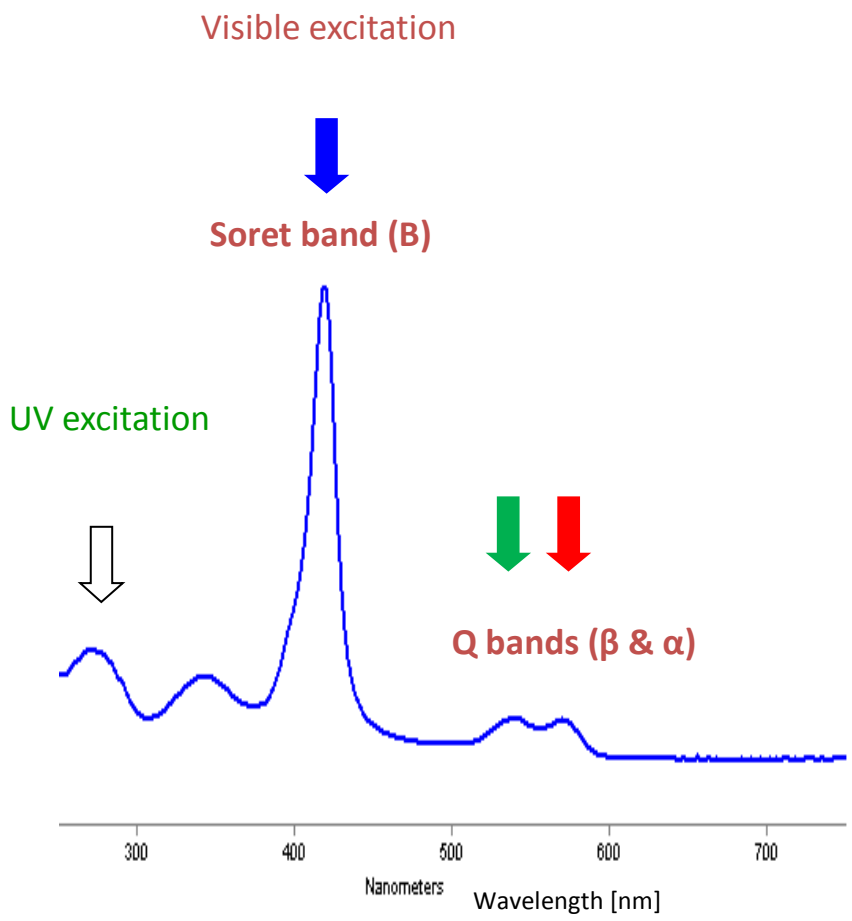

Figure 1.3.3.1 Electronic absorption spectroscopy of human being hemoglobin

1.3.3.1 Studies of ferric and ferrous CO forms of Cytochromes P450

Recalling the enzymatic cycle for cytochromes P450, the first step is binding of the substrate, which usually causes a spin-state change. Figure 1.3.3.2 shows a clear signaling of this change of the ν_3 mode. In addition, another interesting feature is shown in Figure 1.3.3.3, which shows that upon substrate binding modes associated with propionate bending are also affected; i.e., for substrate-free form only a single isolated band is seen near 380 cm^{-1}, but upon substrate binding a second propionate bending mode

appears near 368 cm^{-1}. These data show how well that rR can report on active site interactions associated with heme group distortions [52].

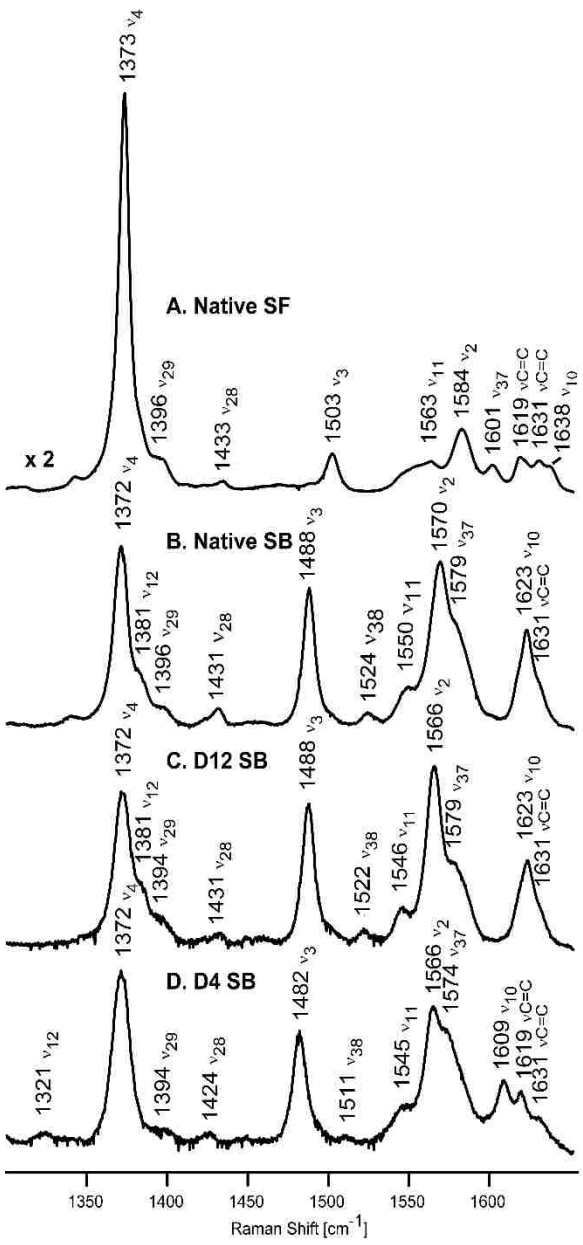

Figure 1.3.3.2 High frequency resonance Raman spectra of native P450cam substrate-free (A) and substrate-bound (B); and substrate-bound deuterated analogues of P450can, d12-P450cam (C) and d4-P450cam (D) [52].

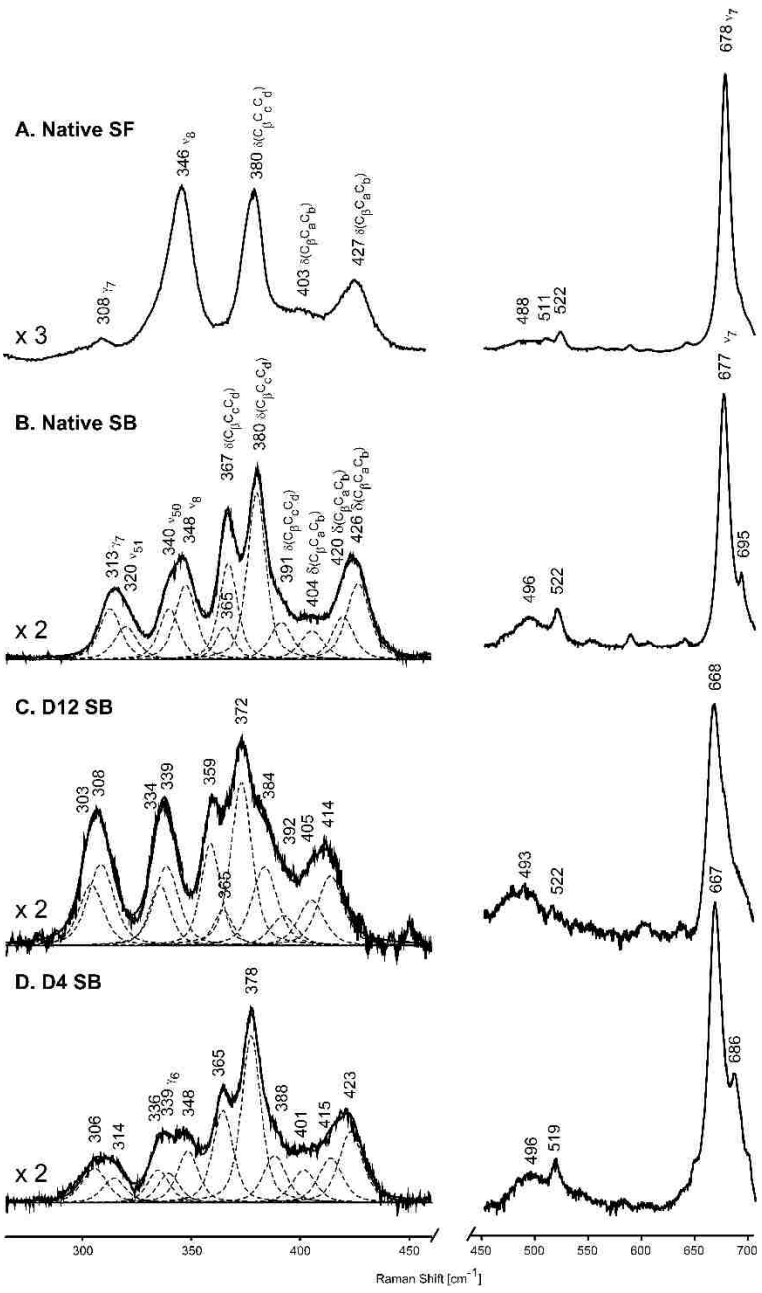

Figure 1.3.3.3 Low frequency resonance Raman spectra of native P450cam substrate-free (A) and substrate-bound (B); and substrate-bound deuterated analogues of P450can, d12-P450cam (C) and d4-P450cam (D) [52].

In addition to these effects on heme structure, rR spectroscopy provides a very good tool for monitoring the strength of the axial ligands to the heme iron in the resting state. As will be shown in Chapter 2 on myoglobin, this is true for histidine ligated proteins, but it is also true for cytochromes P450, where the ν(Fe-S) stretching mode can be detected using a near UV excitation line [53]. A very nice example of this is a recent work from our lab on CYP2B4. This will be discussed further in Chapter 3, but Figure 1.3.3.4 shows that this mode is seen at 353 cm^{-1}. It is very interesting that the introduction of a H-bond donor group in F429H mutant (also studied in Chapter 3) causes a 6 cm^{-1} downshift of the ν(Fe-S) stretching mode comparing to the ν(Fe-S) mode in BHT-bound Wild-type CYP 2B4 [54]. The presence of additional H-bond due to mutagenesis makes the Fe-S bond become weaker, owing to the lower effective negative charge on the thiolate.

The additional H-bond also affects the Fe-C-O linkage in the ferrous CO adduct of F429H mutant, as shown in Figure 1.3.3.5 (upper figure). The ν(Fe-C) mode and ν(C-O) mode both shifted up by 3 and 5-7cm^{-1}, respectively. They show the σ-donation of the proximal thiolate ligand becomes less due to the H-bond introduced by new histidine residue. This result is also supported by computational data [55-57].

As shown in Figure 1.3.3.5 (bottom figure), the inverse correlation of the ν(Fe-C) modes and ν(C-O) modes indicts different polarity of the distal heme pocket which also relates to different strength of the proximal ligand. The points obtained for the F429H mutant are between the points of NOS and Wild-type CYP 2B4. Thus, the strength of Fe-S in F429H mutant is also between NOS and Wild-type CYP 2B4. It means the Fe-S bond become weaker due to new additional H-bond. This effect is consistent with the result of a 6 cm^{-1} downshift of the ν(Fe-S) stretching mode [58-61].

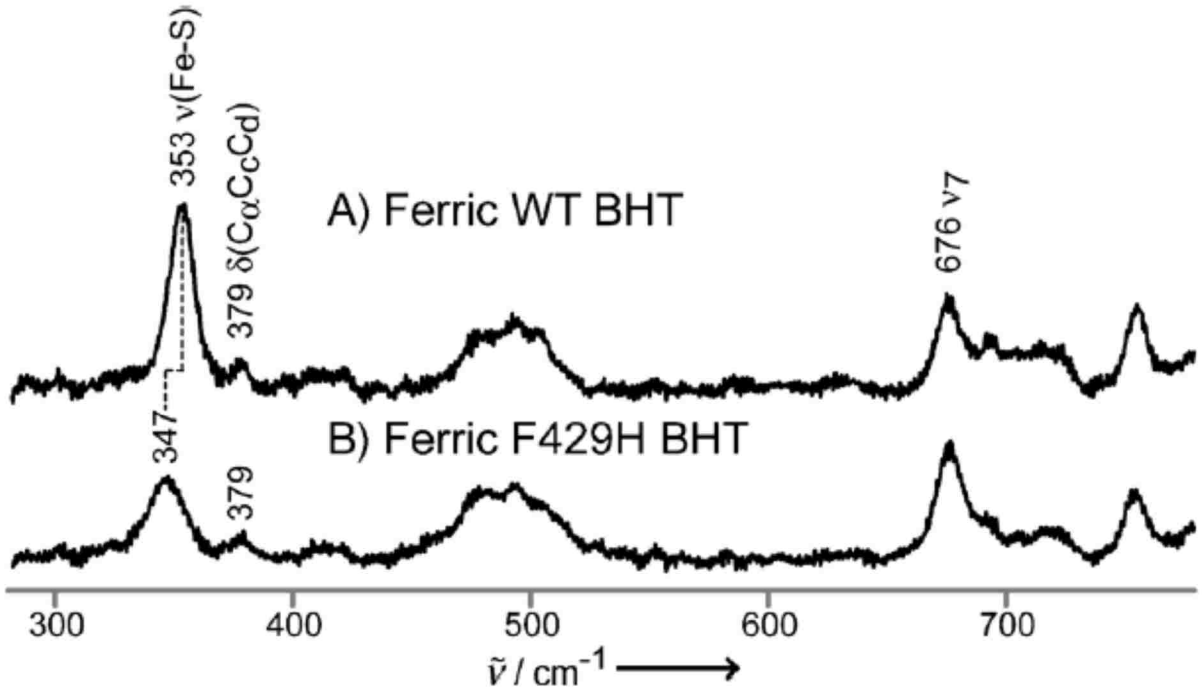

Figure 1.3.3.4 Low-frequency rR spectra of ferric CYP 2B4: A) wild-type BHT-bound; B) F429H mutant BHT-bound. Spectra measured with 356 nm excitation line and normalized to the mode ν_7 at 676 cm^{-1} [54].

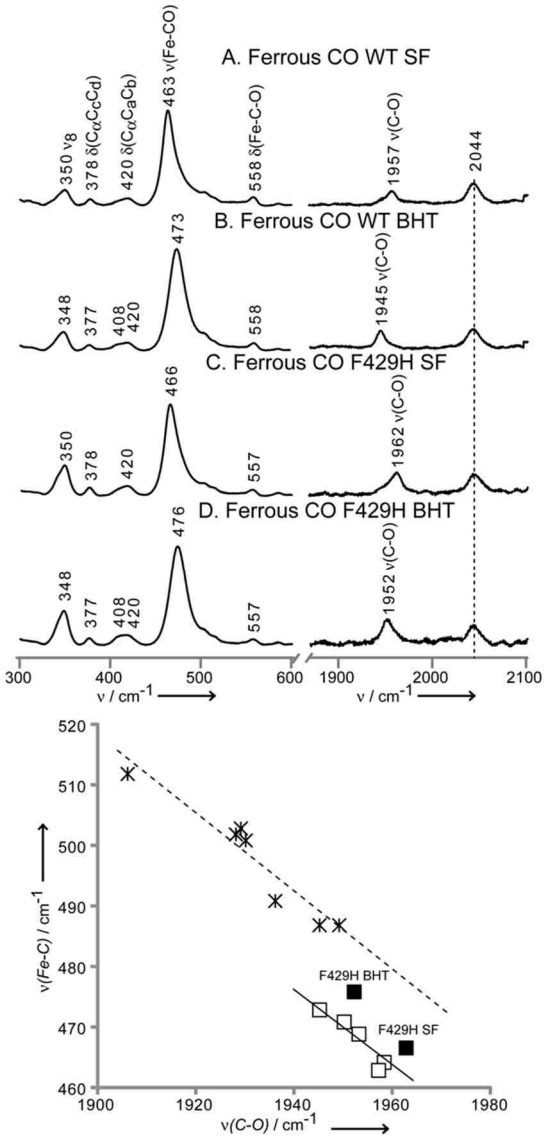

Figure 1.3.3.5 Low- (left) and high (right)-frequency rR spectra of ferrous CO adduct of CYP 2B4: A) wild-type substrate-free; B) F429H mutant substrate-free; C) F429H mutant BHT-bound D) F429H mutant BHT-bound. Spectra measured with 442 nm excitation line and normalized to the mode ν_7 and ν_4. The bottom graph shows linear correlation between ν (Fe-C) and ν (C-O) frequencies, the open squares represent wild-type truncated CYP 2B4, the solid square indicate points for F429H mutants, and the stars show mammalian NOSs [58-61].

1.3.3.2 Dioxygen adducts of Cytochromes P450

Resonance Raman spectroscopy is especially powerful to study the detailed structure of the Fe-O-O fragments of dioxygen adducts of cytochromes P450, because both the ν(Fe-O) and ν(O-O) modes are well enhanced. The best example of this ability to provide key details is seen in a recent paper from our group about CYP17A1 [62]. As shown in Figure 1.3.3.6 A and 1.3.3.7 A, when progesterone (PROG) and pregnenolone (PREG) are bound, the rR spectra show the ν(Fe-O) and ν(O-O) modes are the same (see the $^{16}O_2$ and $^{18}O_2$ difference trace). This is not surprising because these molecules fit into the pocket similarly and there is no H-bond between substrate with Fe-O-O fragment. But when we compare the Figure 1.3.3.6 B and 1.3.3.7 B, the situation changes. The ν(O-O) modes downshift in OH-PREG and OH-PROG bound CYP17A; however, the ν(Fe-O) mode downshifts in OH-PREG but upshifts in OH-PROG bound CYP17A. This is quite informative, because DFT calculations are consistent with the rR result and give more detail to explain rR data. The DFT result shows that H-bond donation to the *proximal* O atom will weaken both the ν(Fe-O) and ν(O-O) modes due to pull the electrons into the non-bonding sp^2 orbital on proximal O atom. On the other hand, an H-bond donation to the terminal O atom will weaken the ν(O-O) mode but *increase* the ν(Fe-O) mode because of the increase of back-bonding [63]. So, these results are consistent with the H-bond interactions shown in Figure 1.3.3.8.

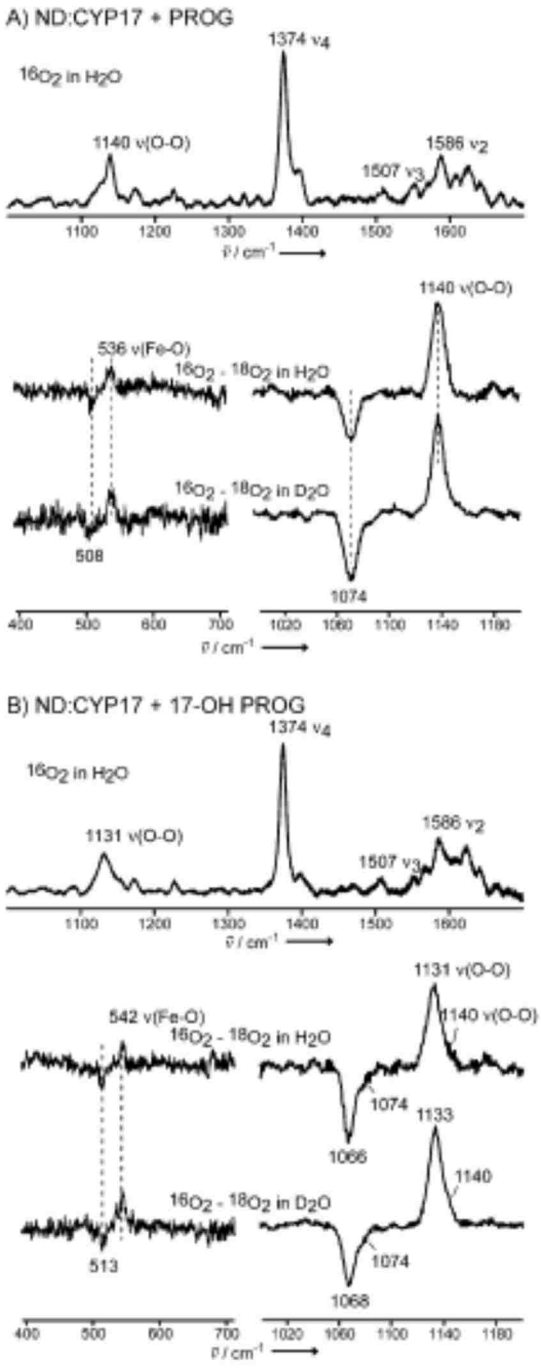

Figure 1.3.3.6 The rR spectra of PROG- and 17-OH-PROG-bound $^{16}O_2$ adducts of ND:CYP17 in H_2O buffer (panel A and B, respectively). The lower section of each panel shows $^{16}O_2$-$^{18}O_2$ difference plots in H_2O (upper) and D_2O (lower) buffers [63].

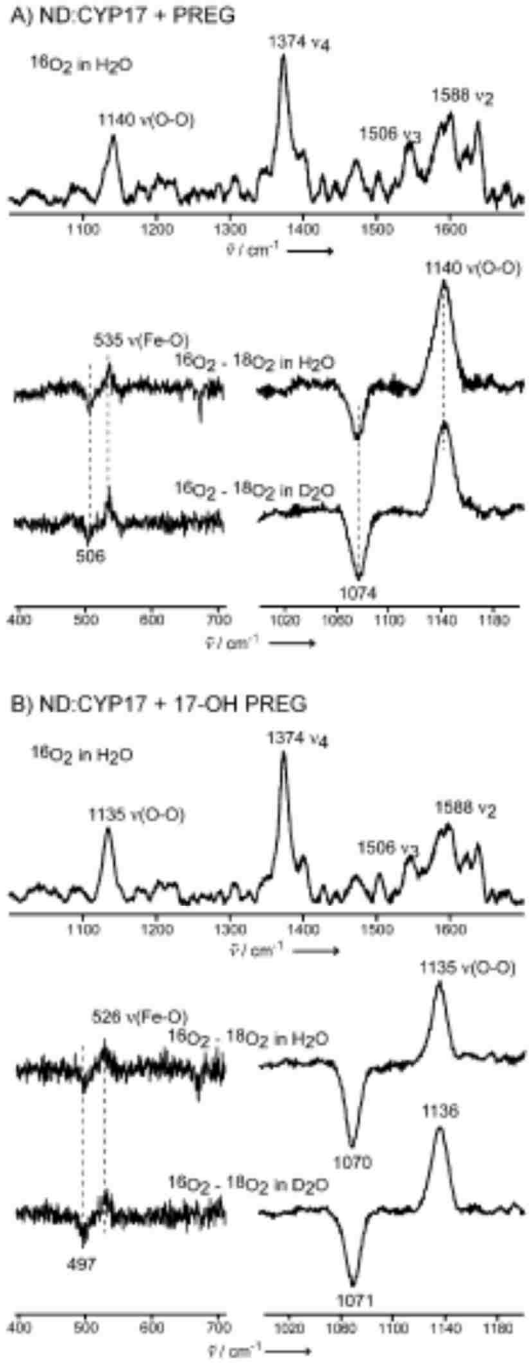

Figure 1.3.3.7 The rR spectra of PREG- and 17-OH-PREG-bound $^{16}O_2$ adducts of ND:CYP17 in H_2O buffer (panel A and B, respectively). The lower section of each panel shows $^{16}O_2$-$^{18}O_2$ difference plots in H_2O (upper) and D_2O (lower) buffers [63].

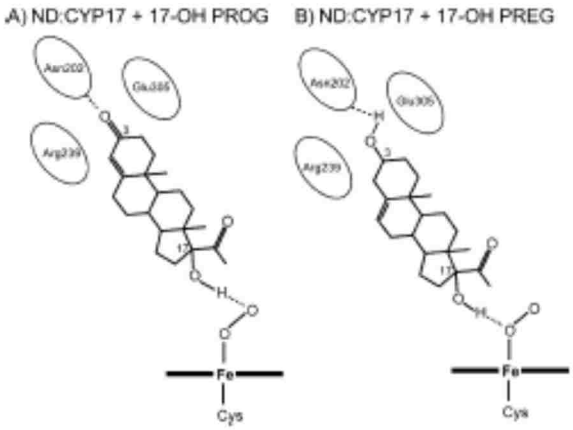

Figure 1.3.3.8 The human CYP17A1 protein–substrate interaction derived from these newly acquired rR data; the substrates are 17-OH progesterone and 17-OH pregnenolone [63].

1.3.3.3 Cryoreduced forms of CYP101

The first reported rR studies of the cryoreduced forms of an oxy-P450 was published by our group in 2007. The oxy-CYP101 was prepared and cryoreduced forms of CYP101 were generated. They used rR data to figure out the ν(O-O) modes appears near 1140 cm^{-1} for the dioxygen adduct precursor and at 1073 $cm^{-1}$for $^{18}O_2$, as shown in Figure 1.3.3.8 (on the left, top two traces). The spectra in the right panel are for the cryoreduced sample. They are very cluttered with heme modes, but by doing difference traces with $^{16}O_2$ -$^{18}O_2$, a new band is seen at 799cm^{-1}, with its $^{18}O_2$ corresponding band at 759 cm^{-1}. Actually, this band might be a ν(O-O) mode of a peroxo-like species, but could also be a ν(Fe=O) mode, which also occurs near here, with similar isotopic shifts.[64] To determine what is correct, so-called "scrambled oxygen" can be used; the $^{16}O_2$:^{16}O-^{18}O:$^{18}O_2$ population is 1:2:1. Looking at the left panel, where we know there is a O-O bond, the (scrambled-$^{16}O_2$) and (scrambled-$^{18}O_2$), give patterns showing there is an

intact O-O bond. If one compares these patterns with the paters seen in the right panel, then it is known that there also is an intact O-O bond; i.e., the right panel patterns indicate a “Fe-peroxo-like” fragment. Actually, since ν(^{16}O-^{16}O)and ν(^{18}O-^{18}O) modes have H-D shift in deuterated buffers as shown in Figure 1.3.3.9 (on the right), the species is assigned as the hydroperoxo- intermediate, because when Fe-O-O-H changes to Fe-O-O-D one sees a shift. The expanded low frequency rR spectra shown in Figure 1.3.3.9 show that the ν(Fe-O) mode of this hydroperoxo-form occurs at 559 cm^{-1} [64].

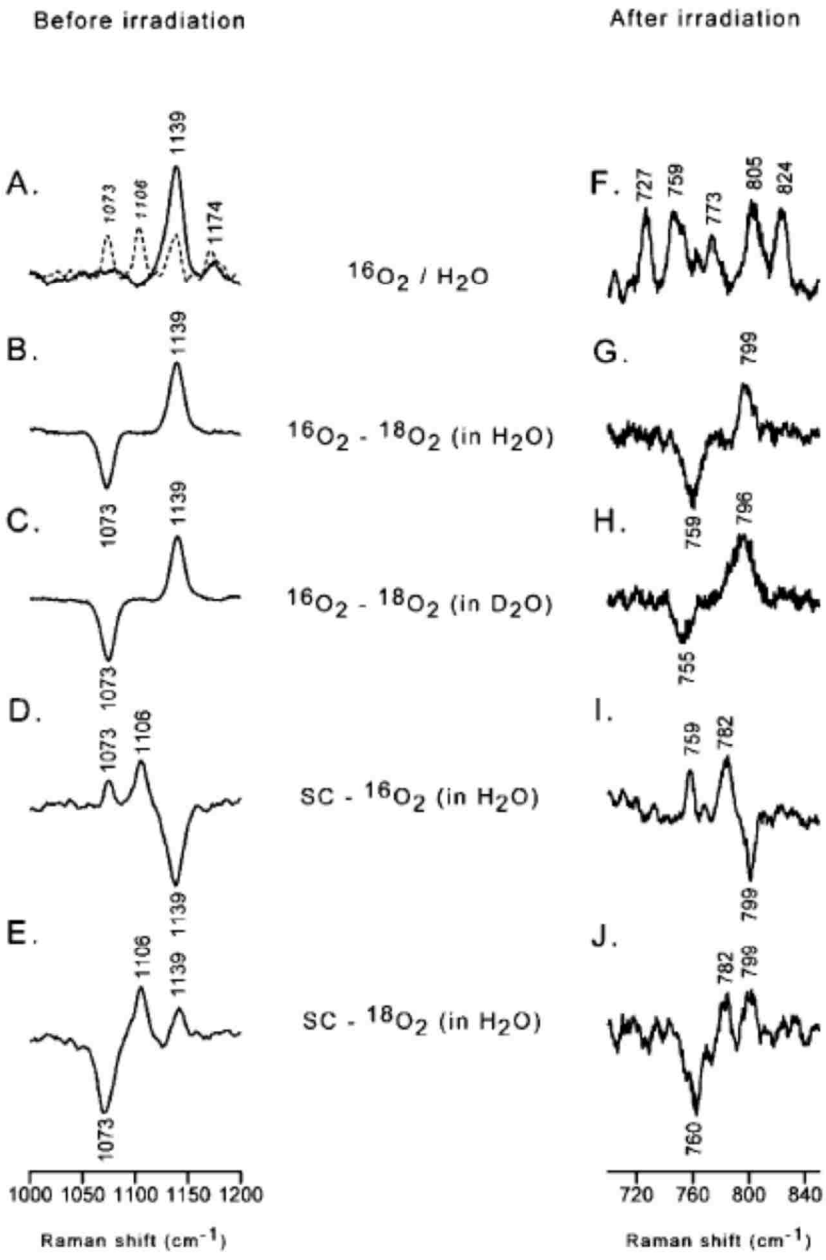

Figure 1.3.3.9 Left panel: RR spectrum of $^{16}O_2$ CYP101 in 30% glycerol/ buffer before irradiation (A); $^{16}O_2$-$^{18}O_2$ in glycerol/buffer (B); $^{16}O_2$-$^{18}O_2$ in deuterated glycerol/buffer (C); scrambled $^{16}O_2$ in glycerol/buffer (D); scrambled $^{18}O_2$ in deuterated glycerol/buffer (E). Right panel: RR spectrum of $^{16}O_2$ CYP101 in 30% glycerol/buffer after irradiation (F); $^{16}O_2$-$^{18}O_2$ in glycerol/buffer (G); $^{16}O_2$-$^{18}O_2$ in deuterated glycerol/buffer (H); scrambled$^{16}O_2$ in glycerol/buffer (I); scrambled $^{18}O_2$ in deuterated glycerol/buffer (J). The dashed line in trace A is for the sample with scrambled oxygen [64].

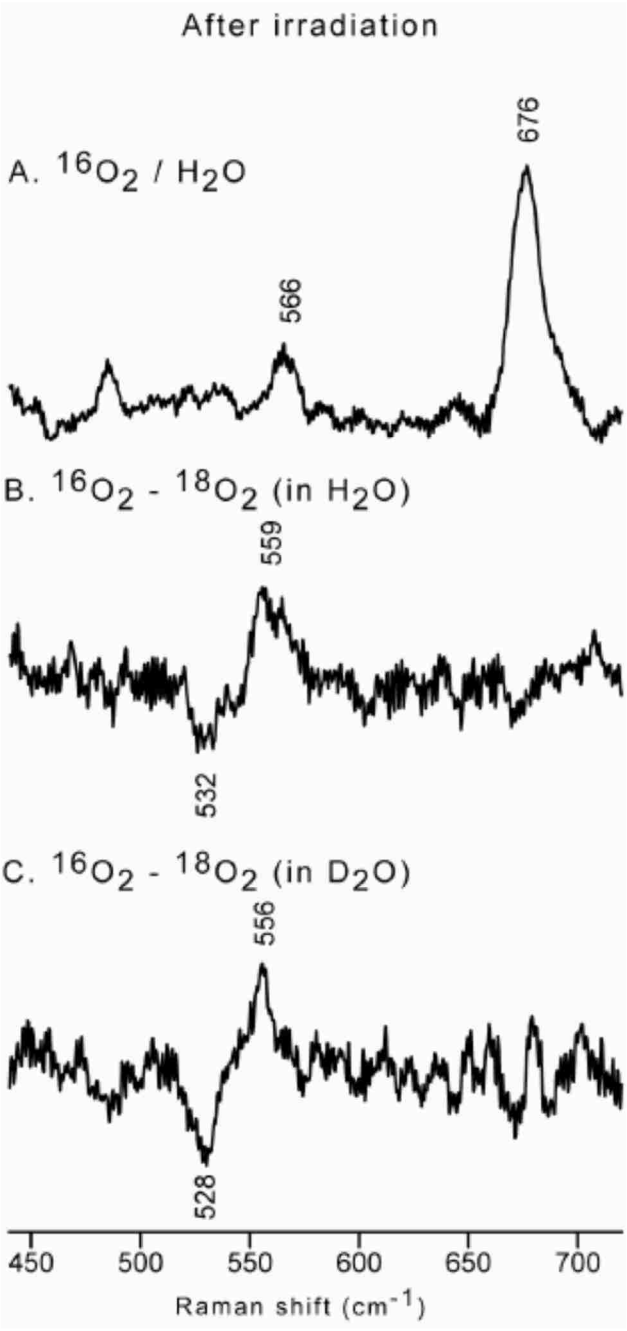

Figure 1.3.3.10 Low Frequency RR spectrum of $^{16}O_2$ CYP101 in 30% glycerol/buffer after irradiation (A); $^{16}O_2$-$^{18}O_2$ in glycerol /buffer (B); $^{16}O_2$-$^{18}O_2$ in deuterated glycerol/buffer (C) [64].

It is interesting to note that in the previous study the hydroperoxo- intermediate was immediately obtained, with no evidence for the peroxo- form that surely was there before it. The reason is that the enzyme is so well designed that proton transfer seems to occur even at 77K. Fortunately, there is a mutant CYP101, D251N CYP101, for which proton transfer is restricted. As seen below, this allowed the trapping and rR spectral characterization of the peroxo- intermediate, with the hydroperoxo- intermediate being later generated by annealing to higher temperature.

As shown in Figure 1.3.3.11, in the rR spectra of oxy D251N CYP101 complex in high-frequency region, there are two $\nu(^{16}O\text{-}^{16}O)$ modes at 1136cm^{-1} and 1125cm^{-1}, respectively. This means there are two structural conformers of the Fe-O-O fragment The $\nu(^{16}O\text{-}^{16}O)$ mode at 1136cm^{-1} mode downshifts for $^{18}O_2$ to1070cm^{-1}; the 66 cm-1 shift upon $^{18}O_2$ substitution, in agreement with that predicted by Hooke's law The other $\nu(^{16}O\text{-}^{16}O)$ mode occurs at 1125cm^{-1} and shifts up by 2 cm^{-1} in deuterated solvents, consistent with H-bonding with an active site donor.

After irradiation the oxy-D251N CYP101 becomes peroxo- and then, following annealing, becomes the hydroperoxo-complex, as shown in Figure 1.3.3.12 and 1.3.3.13. The ν(Fe-O) mode change from 537cm^{-1} to 553 cm^{-1} when the complex change from oxy- to peroxo complex, and ν(O-O) modes change from 1136cm-1 to 792cm-1. When the complex become hydroperoxo-complex, the ν(Fe-O) and ν(O-O) modes become to 564cm^{-1} and 774 cm^{-1}, respectively. The ν(O-O) modes downshift a lot and the ν(Fe-O) mode upshift since the O-O bond become weaker and Fe-O bond become stronger. Those data are consistent with the enzyme cycle of CYP101 [30].

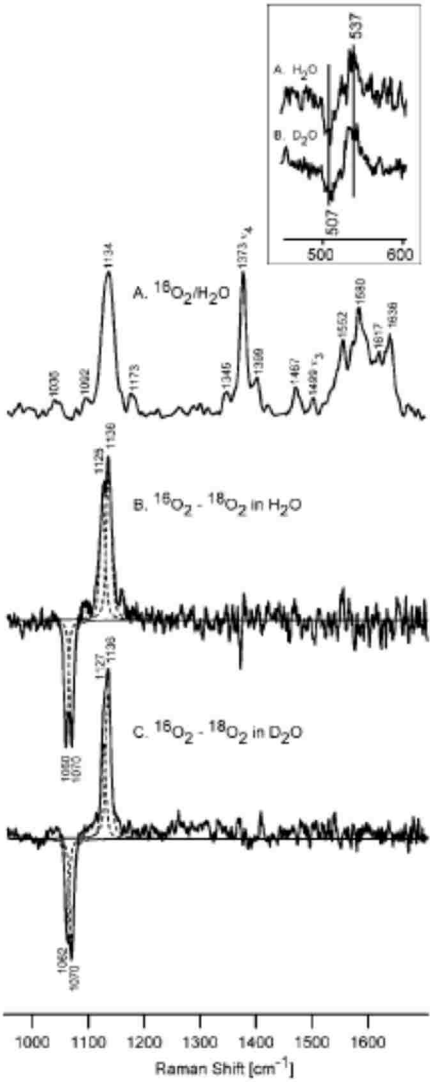

Figure 1.3.3.11 High-frequency RR spectra of oxy D251N CYP101 measured at 77 K and difference spectra before irradiation (excitation at 413 nm). Inset shows low-frequency difference spectra of $^{16}O_2$-$^{18}O_2$ in H_2O (A) and in D_2O (B) buffer [30].

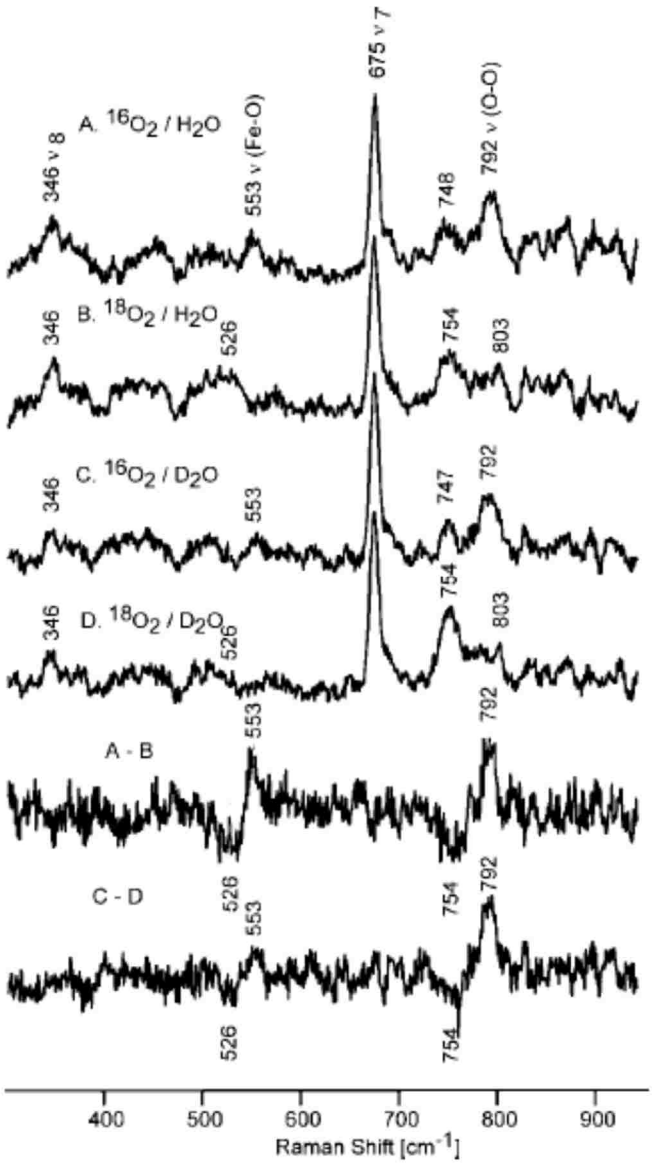

Figure 1.3.3.12 RR spectra of irradiated P450 D251N samples in H2O buffer, spectra A ($^{16}O_2$) and B ($^{18}O_2$), and in the D_2O buffer, spectra C ($^{16}O_2$) and D ($^{18}O_2$). The two bottom traces shows the difference spectra of $^{16}O_2$-$^{18}O_2$ in H_2O and $^{16}O_2$-$^{18}O_2$ in D_2O buffer (excitation line 442 nm, temperature 77 K) [30].

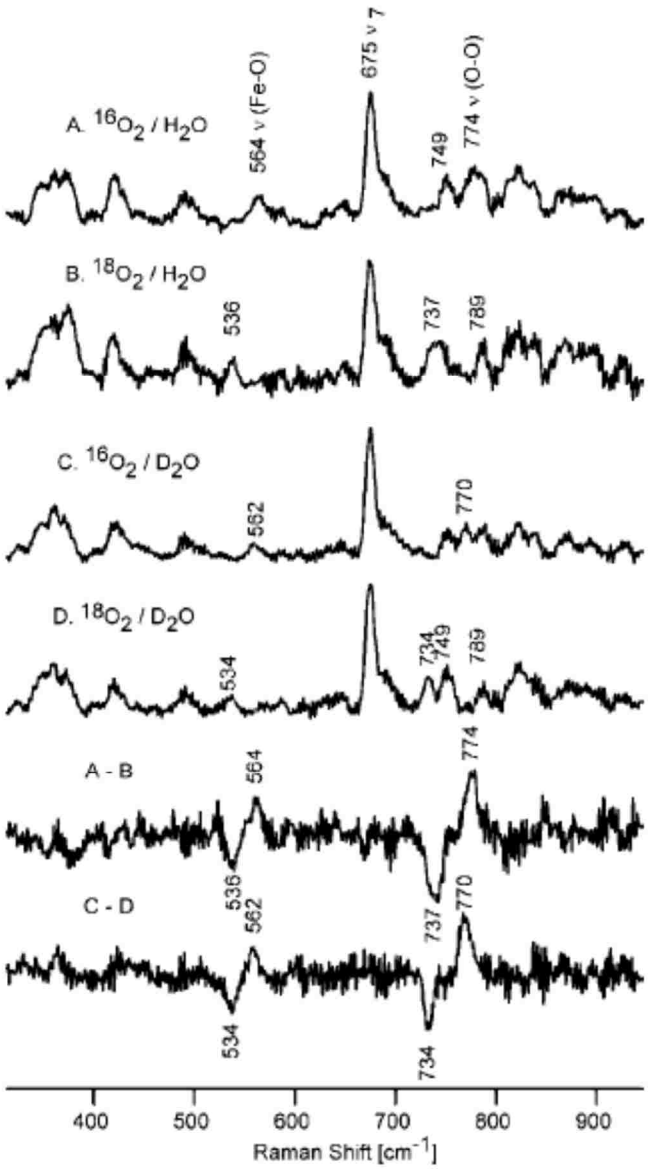

Figure 1.3.3.13 rR spectra of irradiated and annealed at 185 K samples of P450 D251N in H_2O buffer, spectra A ($^{16}O_2$) and B ($^{18}O_2$), and in the D_2O buffer, spectra C ($^{16}O_2$) and D ($^{18}O_2$). The two bottom traces shows the difference spectra of $^{16}O_2$-$^{18}O_2$ in H_2O and $^{16}O_2$-$^{18}O_2$ in D_2O buffer (excitation at 442 nm, temperature 77 K) [30].

It is important to point out here that the single active site mutation in this enzyme not only allowed trapping of the peroxo-intermediate, but also induced a rather large

change in the strength of the O-O bond in the hydroperoxo-intermediate; i.e., the ν(O-O) frequency shifted by 25 cm^{-1} from the 799 cm^{-1} value seen for the WT protein. The magnitude of this effect of a single active site mutation provided some basis for the planned effort to explore effects of such mutations on cryoreduced samples of myoglobin and its mutants (Chapter 2), though such efforts proved to be rather disappointing.

1.4 Mutagenesis Strategies

Myoglobin (Mb) is a heme protein found mainly in heart and skeletal muscle. As oxygen storage and transport protein, Mb is one of the best characterized of all biomolecules. Ligand binding to Mb has long been used as a model system for the study of structure-function relationships in proteins [65].

In order to employ Mb as a model system to investigate the effects of active site structural elements on the Fe-O-O and Fe=O fragments of these reactive species, it will be important to systematically change the active site structure by introducing mutations via established methods of molecular biology.

1.4.1 The method for making mutants: Polymerase Chain Reaction (PCR)

1.4.1.1 Introduction to the Polymerase Chain Reaction (PCR)

Deoxyribonucleic acid (DNA) is a genetic material which stores the genetic information encodes the sequence of proteins and RNA in most of the living organisms and many viruses. It is a linear polymer contained four types of monomers. These four monomers called deoxyribonucleoside triphosphates (dNTPs)

have four different nucleobases: adenine (A), cytosine (C), guanine (G) and thymine (T). They form DNA molecules which has doule-helix structure as shown in Figure 1.4.1 A [66]. Each strand of DNA has a sugar-phosphate backbone and each sugar connects to two phosphate groups. One of nucleobase attaches to the sugar and form specific base pairs (bp) held the two strands together by H-bonding. The base adenine pairs with thymine (A-T) and cytosine pairs with guanine(C-G). The example of DNA single strand is shown in Figure 1.4.1 B. [67]

Polymerase Chain Reaction (PCR) was first introduced by Kary Mullis in in 1984. PCR is a method for amplifying specific DNA sequences exponentially [68]. The dNTPs can enzymatically form the targeted DNA molecules by adding heat-stable polymerase on thermally cycling. The solution where the PCR will happen includes all four dNTPs, target DNA molecule (template), primer, enzyme and buffer solution. The enzyme PCR used is a heat-stable DNA polymerase which comes from *Thermus aquaticus*, a thermophilic bacterium in hot spring. PCR can generate a 10^6-10^7 fold increase in the concentration of DNA or RNA.

PCR is a powerful tool for medical diagnostics, forensics and studies of molecular evolution.

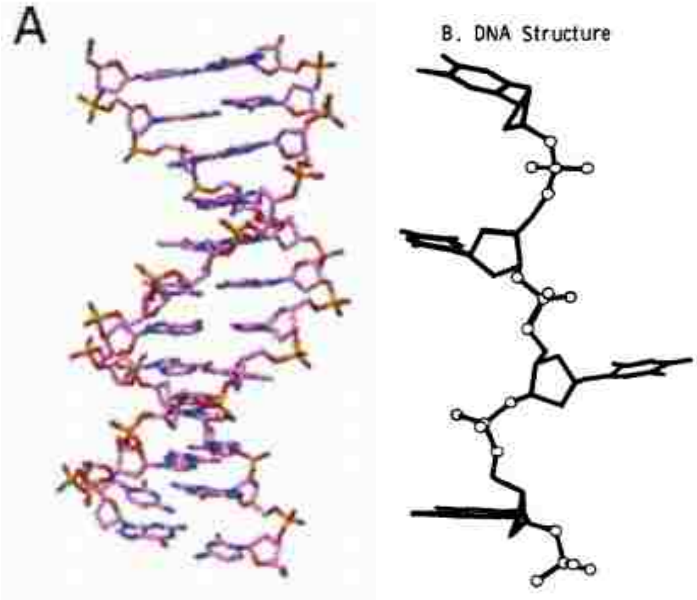

Figure 1.4.1 The structure of B-DNA (X-ray, PDB 1BNA) (A) and structure for a single strand of the DNA in Pfl (B) [66, 67]

1.4.1.2 Primer design

The primers in the PCR are a pair of oligopeptide which can be a starting point for DNA synthesis. The length of primers is usually 25-45 nucleotides. Since the primers need to anneal to the opposite strand of plasmid, the sequences of primers match the beginning and the end of the DNA fragment to be amplified. The sequence does not have to 100% the same as the original sequence. The desired mutation should be in the middle of primer and has minimum change. The melt point of primer should be higher than 78°C and %GC should be higher than 40%. The terminals need to include at least one C or G.

There are some website tools that can help primer design, like primer design tool in ncbi: http://www.ncbi.nlm.nih.gov/tools/primer-blast/.

Here is an example of primer design. The template is horse heart Mb. The mutate is H64L. The highlight part is the amino acid code where the mutation happen.

E.g. The original sequence:

CGTCTGAAGATCTGAAAAAACATGGTACCGTTGTGTTAACT

The primer:

CGTCTGAAGATCTGAAAAAACTTGGTACCGTTGTGTTAACT

1.4.1.3 The steps of PCR cycle

The PCR happens in the thermal cycler where the temperature can be programmed to make rapid and accurate temperature changes during the reaction. The thermal cyclers need to have heated lids to prevent condensation otherwise a layer of oil needs to be placed on the top of the reaction mixture. The PCR cycle consist of three steps: strand separation, hybridization of primers and a heat-stable DNA polymerase, as shown in Figure 1.4.2.

a. Strand separation

The two strands of DNA denature and separate at 95°C for several seconds. The other ingredients are stable at this temperature in the solution.

b. Hybridization of primers

In the second step, the solution cooled to 55°C to allow the primer anneal to the DNA template. The primers adds to the solution are pairs of oligonucleotide will which can hybridize to the 3' end of the target DNA. The DNA duplexes are not formed since the large excess primer forbid the template DNA to come close enough.

c. DNA synthesis

Since the optimum temperature for *Taq* DNA polymerase's activity is around 75°C, the DNA synthesis happen at ~70°C. The primer is the starting point of DNA synthesis. The reaction is in the 5'-to-3' direction and extends beyond the target sequence. The DNA synthesis happens on both two types of strands.

After these three steps, the temperature increases to 95°C ago and the second cycle begin. In each cycle, the reaction will produce 2n DNA. For example, if there is one DNA template, after first cycle, there are 2 DNA in the solution. After second cycle, there are 4 DNA in the solution. The DNA produced from the last cycle is the new template for the next cycle. Ideally, the number of DNA is amplified 2^n fold after n cycles. Usually, the cycle number will be less than 20 [69].

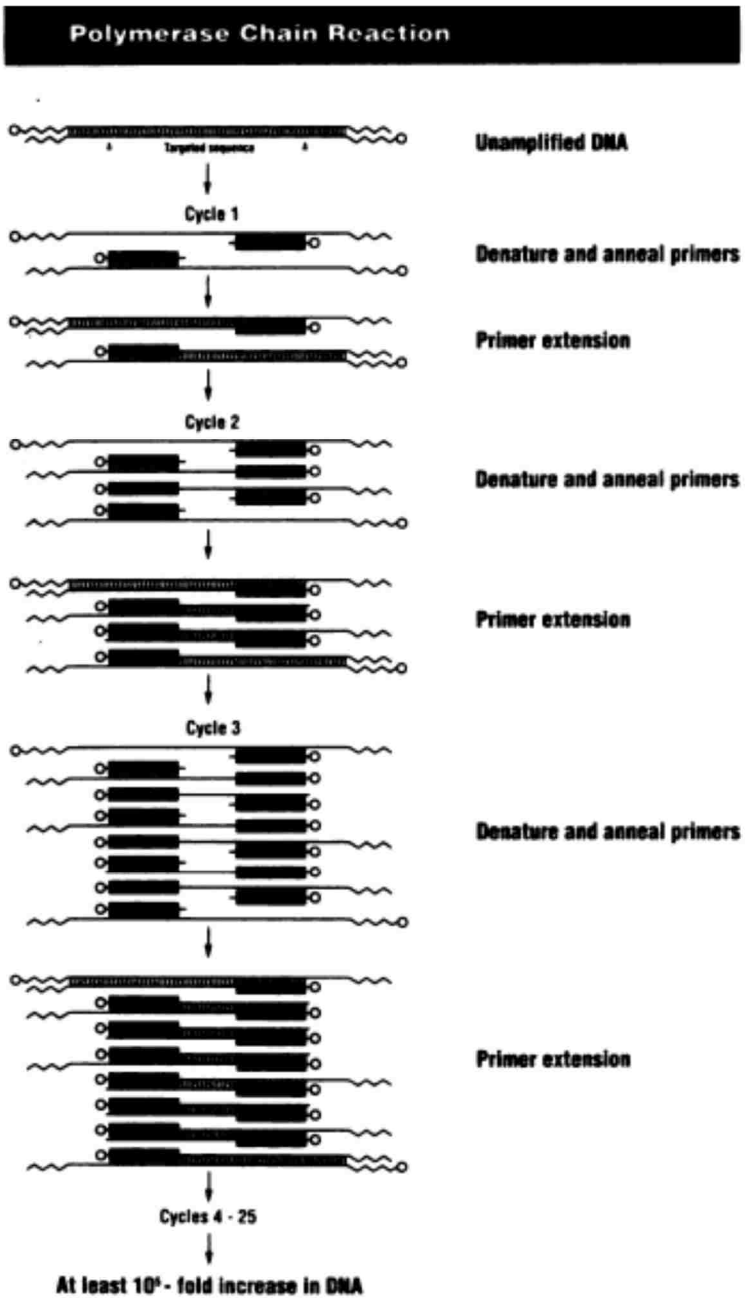

Figure 1.4.2 The procedures of PCR [69]

1.4.2 The applications for PCR

As a method to amplify the DNA, PCR can be used to produce more DNA. The primers do not need to be perfect the same as the flanking sequences to amplify the DNA. Thus, PCR can produce the mutants. The mutation site should be in the middle of the primers.

PCR is also a valuable method to provide diagnostic information in medicine. The DNA in bacteria and viruses in body and tissue can be amplified in PCR by adding specific primers. For example, PCR can be used to detect HIV genotyping by using PCR. Also, early cancer can be readily and rapidly detected by using PCR [70, 71].

The genetic sequence of individual DNA is highly distinctive thus PCR also can be used for forensics and legal medicine. The analysis result of blood and semen samples can reveal guilt or not in numerous case.

1.5 Specific Aims of the Dissertation

1.5.1. Applications of rR spectroscopy to cryoradiolytically generated reactive oxygenated derivatives of myoglobin and its mutants

Realizing that it is possible to generate and trap the intermediates in the enzymatic cycles of heme enzymes like peroxidases and cytochromes P450, this group began a plan to study model system to try to get a better understanding of the applications of cryoradiolysis and resonance Raman (rR) spectroscopy. The basic idea was to try to improve the techniques to trap the sometimes very unstable precursors, the dioxygen complexes. It was decided to use myoglobin as a model. This protein is studied a lot as a

model for many methods. The plan was to prepare a number of mutants, with replacements on both the distal pocket and on the proximal side of the heme, where the heme axial ligand, histidine sits.

In the end, only about 6 mutants proteins were obtained by me. We were able to obtain good dioxy samples of all of the seven proteins. Of the mutants, only for H64L had the oxy-complex been studied before. Finally, we were able to make samples suitable for cryoradiolysis studies and also were able to acquire rR spectra for all of them; none of the cryoreduced mutant samples had ever been made before. The final situation was that only two mutants gave interesting results. Both of them are distal pocket mutants; H64L and V68S.

1.5.2. Resonance Raman Characterization of dioxygen adducts of CYP2B4 and its distal and proximal side mutants

Soon after my Research Meeting I was assigned to begin working with CYP2B4, a drug metabolizing cytochrome P450, to begin to do studies on cryoradiolysis of the dioxygen adducts of this enzyme. The first thing I needed to do was to make the dioxygen complex of this protein, working together with Dr, Piotr Mak and Dr. Sangchoul Im from Dr. Waskell's lab. The biggest problem for this project was to try to get good samples of the dioxygen complex. The dioxygen complexes of *bacterial* cytochrome P450 are relatively stable. One that is studied a lot in our lab is cytochrome P450camphor, because it is a bacterial protein and easy to get. Actually, it has a very stable oxy complex, because it remains stable in cold solution for several minutes. The dioxygen complexes of steroidogenic P450s are also relatively easy to prepare and freeze. However, the dioxygen complexes of drug metabolism P450s are very *unstable*. In the

beginning, before I worked on this project, the samples of 2B4 from Dr Waskell's lab were able to be generated most of the time. However, it seems the methods used changed, because the CYP2B4 samples we have been getting are much more difficult to get stable oxygen adducts.

I worked many hours with Drs Mak and Im (who would bring samples) for over a year, trying to reproducibly make samples of the dioxygen adduct of CYP2B4. Eventually, we succeeded and were able to prepare samples, with various isotopes; $^{18}O_2$ and D_2O buffers. Once that was done, the next step was to make similar samples with two mutants of CYP2B4; one distal side mutant (E301Q) and one proximal side (F429H). The E301Q is supposed to stabilize the peroxo- intermediate and the F429H, which donates an H-bond to the heme thiolate ligand, is reported to have a more stable dioxygen complex; the problem with F429H is that it is supposed to convert to an inactive "P420 form" before it can oxygenate. These efforts have been going on for over a year, with almost no success. Sometimes we would get some oxy complex of E301Q, but not always. The work with F429H was not successful at all. As will be seen in Chapter 3, very recently we had a breakthrough and can anticipate that the O_2 samples of all 3 proteins will be finished and rR spectra obtained.

Chapter 2. Resonance Raman studies of myoglobins and mutants in the oxygenated and cryoreduced forms

2.1 General introduction to myoglobin and its mutants

Myoglobin (Mb) is a heme protein found mainly in heart and skeletal muscle. Hemoglobin (Hb) and myoglobin work together to transport and storage oxygen in most aerobic organisms. They can bind oxygen corporately and reversibly. Hemoglobin is nearly saturated with oxygen in the lung, where there is a high concentration of oxygen. The oxy-Hemoglobin is transported to area of low oxygen concentration by blood stream. In the respiring tissues the oxygen is released from Hb and delivered to Mb. Mb is a globular protein which contains 8 α-helices and one protoheme prosthetic group. Mb is one of the best characterized of all biomolecules, since it is the first protein whose high resolution structure was determined by X-ray crystallography [72, 73]. The central iron of the protoheme prosthetic group is in the ferrous state and can bind molecular oxygen reversibly. In the heme proteins, iron reactivity is electronically and sterically controlled through the iron axial ligand. Mb has long been used as a model system for the study of structure-function relationships in proteins [74]. Combination of site-directed mutagenesis with spectroscopy studies can give useful information about the theories such as steric hindrance, hydrogen bonding, and polarity change in heme proteins [75]. Therefore it is reasonable to use this protein to conduct systematic studies of the responses of the Fe-O-O and Fe=O fragments of "oxy-derivatives" to changes in the active site brought about by mutating some active site residues. That is the essential goal of our work, where the "oxy derivatives" that will be studied include the dioxygen complex, the peroxo- and hydroperoxo- species. It may also be possible to generate and

study O-O bond cleavage products such as Compound I and Compound II-like forms, all of these species being relevant to work currently being done on cytochrome P450s and other heme enzymes [76-78]. Some relevant earlier work has been completed for several types of heme enzymes [79-84], but a study of the dioxy-, cryoreduced and O-O bond cleavage products of any particular protein whose active site has been systematically altered has not been completed; this is the main goal of this work.

2.1.1 Introduction of Mb mutants

Amino acid residues obviously play important roles in protein functions. In the case of HH Mb, the amino acid residues, His64, Leu29, Val68 and Ile107 are on the distal side, where they can interact with bound exogenous ligands affecting their affinity. [85] Therefore, it can be expected that a mutation of any of these residues in the distal side of the heme pocket could cause large changes in the ligand-binding properties [86-90] On the other hand, residues His93, His97, Ser92 and Leu89 play an important role in the H-bonding network on the proximal side as displayed in Figure 2.1, interactions which can affect the strength of the key Fe-N_{his} bond, which in turn can manipulate ligand affinity. [91]

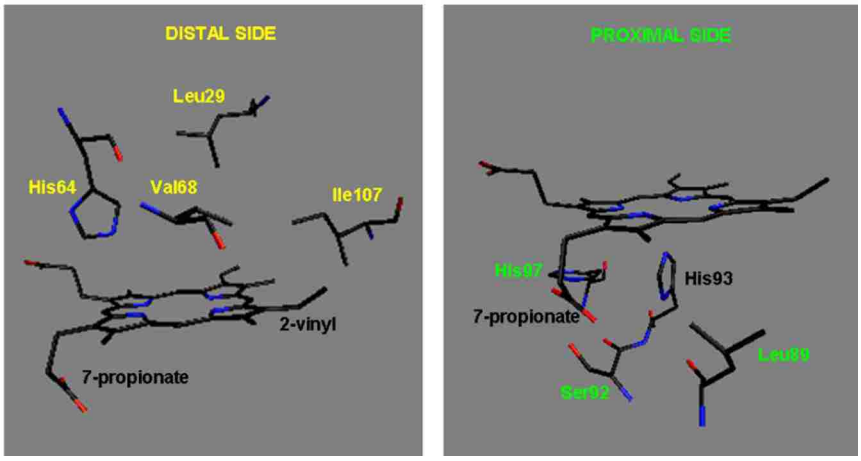

Figure 2.1 The amino acid residues in the distal and proximal pocket of Mb

2.1.2 Previous functional and RR studies of Mb mutants

Site-direct mutagenesis experiments supply a good method to define the importance of polarity, hydrogen bonding, and steric hindrance in the distal and proximal pockets in ligand binding to heme protein. For Mb mutations, there are two categories: distal mutations and proximal mutations. Seven mutation sites are chosen in our studies, as shown above in Figure 2.1. Four sites are on the distal side: Leu29, His64, Val68 and Ile107. Three sites are on the proximal side: Leu89, Ser92 and His97.

2.1.2.1 Distal Side Mutants

The studies of diatomic ligands CO, NO and O_2 bound with Mb mutants can indicate the different interactions between the exogenous ligands with protein residues, and the various distal residue geometries [92, 93]. The NO, O_2 and CO diatomic molecules are common exogenous ligands for heme proteins to study structures and interactions. The

CO molecule binds to heme; it bind to heme plane by linear mode and the Fe-C-O configuration is perpendicular to the heme plate. In contrast, NO binds to ferrous heme proteins in a bent conformation similar to the Fe-O-O fragment, so ferrous nitric oxide proteins are thought to be reasonable models for oxy-heme protein, since O_2 is also binds heme group in a bent orientation [94]. As another important exogenous ligands CN^-, the rR spectra of ferric CN^- complex are much more complicated than the other two ligands, owing to the presence of multiple conformers. So less work on the ferric CN^- complex has been done compared to the other two complexes, even though it is a good hydrogen receiver [88].

The CO, NO and O_2 empty π^* orbitals share Fe d_π electrons with porphyrin π^* orbitals to form the d_π-π^* back-bonding. Thus when the back-bonding from the porphyrin macrocycle is enhanced, the back-donation from Fe d_π to XO π^* orbital will decrease. The Table 2.1 shows some trends in the data of ν(Fe-X) and ν(XO) in some distal mutants. Higher polarity of distal pocket increases back-bonding and decreases the ν(CO), like in V68S and L29W. On the other hand, the behavior of the NO adducts of these two mutants seems inconsistent; i.e. the ferrous NO adducts of these two mutants exhibit unaltered ν(N-O) modes compared to WT, with only V68S exhibiting a significantly different (substantial) down shift. In the mutant H64L, the polarity decreased, so the ν(NO) increased, though the ν(CO) wasn't changed. Though studies on Fe(II)-NO and Fe(II)-CO can be of some help in providing information of relevance to understanding oxy-Mb [76, 94], direct interrogation of the dioxygen adducts themselves would be of much more relevance; as will be shown in this work, this becomes quite practical using cryogenic techniques and well-designed mixing methods.

Table 2.1Vibrational Frequencies for NO and CO Adducts of Mb mutants

Protein name	ν(NO)	ν(Fe-NO)	ν(CO)	ν(Fe-CO)	ν(O-O)	ν(Fe-O_2)
Wild-type Mb	1613[a]	558[a]	1965[a]	490[a]	x	571[b]
H64L	1635[a]	563[a]	1965[a]	490[a]	x	570[b]
V68S	1614[a]	547[a]	1949[a]	x	x	x
L29W	1615[a]	559[a]	1949[a]	x	x	574[b]

[a] NO data taken from ref *80*; [b] dioxygen data taken from ref *76*.

a. H64L

The scheme 1 shows a hydrogen bond between the oxygen of oxy-Mb and His64 which helps to stabilize the oxy-complex. The mutation on the His64 tend to hinder sterically the binding of CO but no steric constraint on the Fe-O-O complex, since the affinity of CO reduced and no change on O_2 affinity[95, 96]. The binding energy is related to the strength of bond. The bonding energy of wild-type Mb to O_2 is 0.26eV, and for H64L is 0.12eV [97]. The decrease of bonding energy is significant upon mutation. The replacement from His to Leu decreased the stabilization of the bound O_2 since the H-bonding between O_2 and His 64 was removed. These data were taken to suggest the bond of Fe-O_2 of H64L Mb mutant is weaker than wild-type; interestingly, the authors note that the corresponding vibrational data imply the lack of a correlation between binding energy and Fe-O bond strength, as measured by ν(Fe-O) frequency.

Scheme 1. Oxygenation of Deoxy Mb[a]

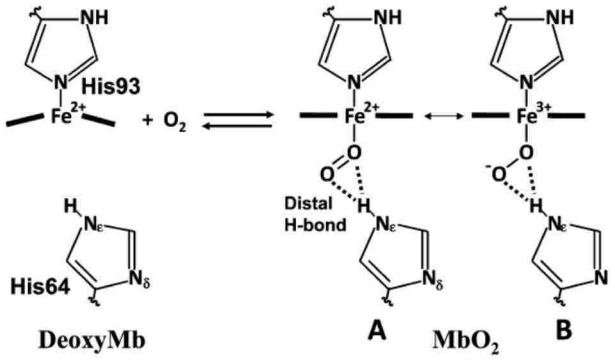

The structure B is only the proposed one [90].

The room temperature rR spectra of oxy-H64L are shown in Figure 2.2, along with those of oxy-L29F and L29W, to be discussed later. At room temperature, the ν(Fe-O_2) modes of WT-Mb and H64L are 571 and 570cm^{-1}. The frequency of ν(Fe-O_2) directly reflects the strength of the Fe-O_2 bond. Thus, the strengths of the Fe-O_2 bond of H64L and WT-Mb are practically the same. As would be anticipated, this distal mutation had no significant effect on proximal side structure, as indicated by the fact that the ν(Fe-His) of H64L (221 cm^{-1}) and native (220 cm^{-1}) deoxyMbs are not substantially different. [76]. There is a correlation between ν(Fe-O_2) and the Fe-O-O angle observed in the crystal structures of MbO_2 [98]. The rR result for this mutant shows the Fe-O-O angle of wild-type and H64L oxy-Mb is almost the same.

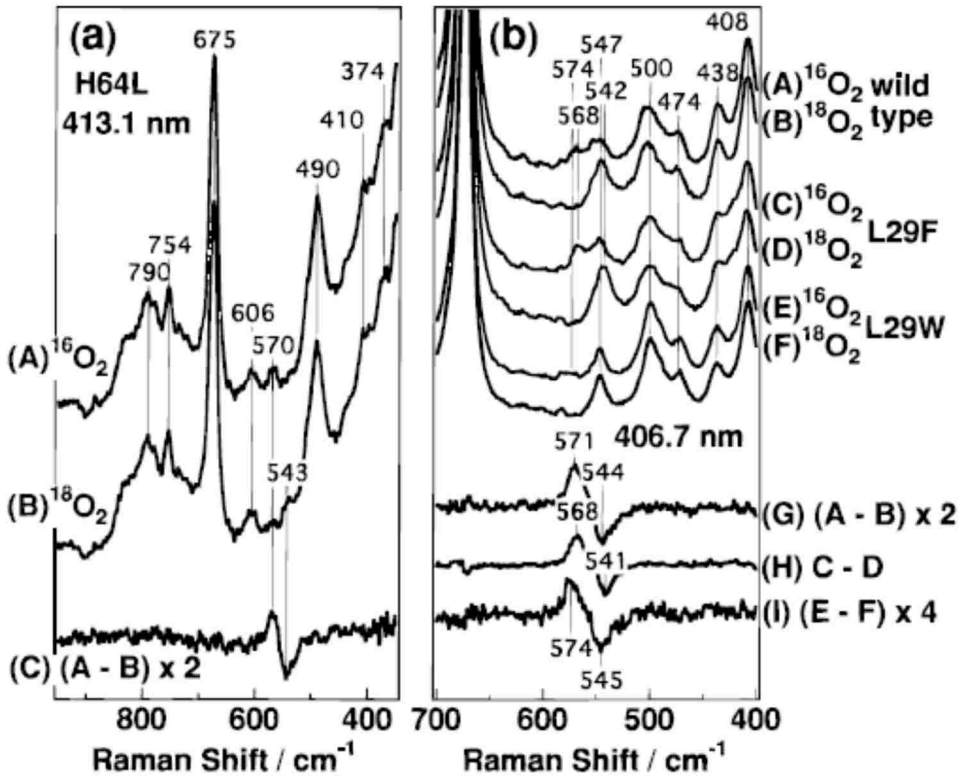

Figure 2.2 rR spectra in the 950-350 cm^{-1} region for the $^{16}O_2$ (A) and $^{18}O_2$ (B) adducts of Leu29 and His64 Mb mutants and their difference spectrum [76].

b. V68S

Valine is a small hydrophobic amino acid. Replacement of Val68 with Ser may create a new hydrogen bond and have some effect induced by new H-bonding interactions. In the past, mutations have been introduced which were intended to test the effects of steric bulk of newly introduced larger hydrophobic residues. For example, the replacement of Val68 to Ile can cause 10-fold decrease in CO transfer coefficient Kco [99], because of steric effects directly over the iron. Also, there is a decrease of Kco upon substitution of Phe for Val68. Since the hydrophobic amino acid residues Phe has larger volume than

Val, the decrease of Kco attributed to steric hindrance in the distal packet. The mutation Val68 to Ser also can cause the Kco decrease, because Ser increase the polarity in distal packet and enhance the back-bonding of CO with Fe [100].

Despite the observed functional changes, substitution of hydrophobic amino acid for Val 68 has little effect on vibrational spectrum of bound C-O. The wild-type ν_{CO} is 1941cm^{-1}, and the values of V68A, V68I, V68S and V68F are 1943, 1938, 1949 and 1940cm^{-1}, respectively. Inasmuch as the hydroxyl group can rotate away from the CO ligand, it is perhaps not surprising that there is very small change compared to wild-type Mb [100, 101]. However, replacement of V68 with hydrophilic amino acid can change the IR spectrum. A 19cm^{-1} downshift of ν_{CO} (to 1922 cm^{-1}) inV68N mutant's IR spectrum since the amide N_δ atom is in the hydrogen bond distance of the bound ligand [97]. The CO complex of mutant V68N has higher binding energy than wild-type it may come from the structure change of ligand [90, 97]. The ν (Fe-CO) of pig V68T mutant has 3cm^{-1} upshift [103],this being in agreement with fact that the hydroxyl group of the T68 is within the distance for hydrogen bonding to CO molecule [76, 91]. Based on all this, it is reasonable to expect that in the V68S mutant of oxy-Mb, there is possibility of creation a new hydrogen bond between Ser68 and the O_2 ligand, an interaction that will be probed in the frozen samples being prepared in this work. Furthermore, it is also possible that H-bonds would impact the Fe-O-O fragments of peroxo- and hydroperoxo forms.

c. I107A

Some mutants had little effect of Fe-O-O fragment but they may reorient the peripheral substituents; i.e., mutation of Ile107 [104]. The position of Ile107 is

between the 2-vinyl and 3-methyl groups of heme. Replacement from Ile to Ala, the polarity and steric hindrance decrease.

In this approach, mutations in Mb will be made to reorient the peripheral substituents; i.e., replacement of Ile107 with other amino acid residues of differing volumes (e.g., Phe or Ala), which is in close proximity (3.65-4.59 Å) to the 2- and 3- heme peripheral groups [105]. This strategy might well serve to manipulate vinyl group disposition with respect to the heme plane, noting that the issue of interest here is the extent to which such alterations, which are readily detected in the rR spectrum, are able to perturb the Fe-OH, Fe=O and Fe-O-O fragments.

2.1.2.2 Proximal Side Mutants

a. S92A, S92L and S92V

In the proximal side of Mb, the H-NMR and X-ray data confirmed the Ser92 forms a weak H-bonding with the proximal histidine (His93) in the WT Mb [106]. The replacements of Ser92 with Ala, Leu and Val caused the imidazole plane of His93 to be rotated around the Fe-N_{His}. Also, the affinity of the protein for O_2 and CO increased as Ala<Val<Leu [106]. In addition, the elimination of the H-bonding between His-97 and the 7-propionate caused the significant change in the propionate sensitive groups [107].

In the proximal side of Mb, an extensive hydrogen-bonding network is implicated in stabilizing the Mb proximal geometry (Figure 2.3) [107]. The Ser92 forms a weak H-bonding with the proximal histidine (His93) in the WT Mb. This conclusion has been suggested by the 1HNMR spectra of the S92A/H93G mutant [108, 109].

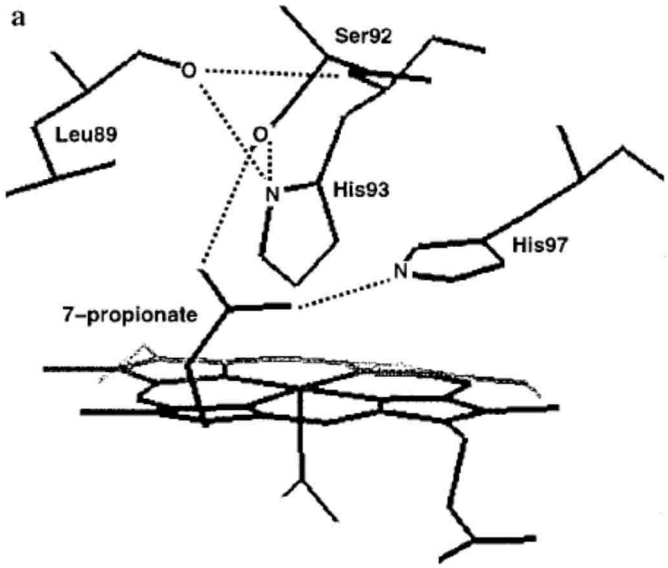

Figure 2.3 Proximal heme pocket showing the hydrogen bonds between the $N_{\delta}H$ of the His93 imidazole ring and the hydroxyl side chain of Ser92 and the carbonyl of Leu89. Also shown are the hydrogen bonds from the 7-propionate carboxylate group to the hydroxyl of Ser92 and the imidazole of His97 [107].

Three proximal Mb mutants, S92A, S92V and S92L, the hydrogen bonds were eliminated from position 92 to both His93 and the 7-propionate. The $\nu_{Fe\text{-}His}$ band in the S92A upshifts to higher frequency (219.7cm^{-1} to 222.8cm^{-1}) due to the small change in the His93 imidazole azimuthal angle [107].

b. H97F

H97F eliminates H-bonding to the heme 7-propionate group, but maintains the presence of an aromatic ring close to the porphyrin macrocycle. The $\nu_{Fe\text{-}His}$ band in the H97F downshifts to lower frequency (219.7cm^{-1} to 217.9cm^{-1}) and the bond of Fe-His97 gets weaker [107].

2.2. Method and materials

The plasmid encoding the wild-type Mb gene was kindly provided by the Mauk group (Professor Grant Mauk, University of British Columbia). The site-directed mutagenesis kit NEB 5-α competent *E.coli* and *E.coli* strain BL21 were purchased from Biolabs. Tryptone, yeast extract and Lauria-Bertani (LB) agar, used in the expression procedure described below, were purchased from Mo Bio Laboratories Inc. Sodium dithionite, ampicillin and glycerol were obtained from Sigma Aldrich.

2.2.1 Site-Directed Mutagenesis, Protein expression and Purification

2.2.1.1 Site-Directed Mutagenesis

The original plasmid called pGYM （4.5kbp）, bearing the coding sequence of the horse heart wild-type Mb plasmid, was a gift from the Mauk group of University of British Columbia [83]. The primers were ordered from Integrated DNA Technologies (IDT). The mutations at positions 29, 64, 68, 89, 92, 97 and 107 were generated by using site-directed mutagenesis method [110]. The QuikChange II Site-Directed Mutagenesis

Kit (Agilent Technologies Co.) which is good for short (4kb-8kb) plasmids was chosen to produce the mutants. This kit includes two parts: mutagenesis and transformation part. The overview of the mutagenesis method is shown in Figure 2.4.

After the mutagenesis, in order to avoid uncontrolled mutagenesis, the DNA template was extracted and sent to Beckman Coulter Genomics for DNA sequencing.

The PCR protocol was shown as Table 2.2 indicated.

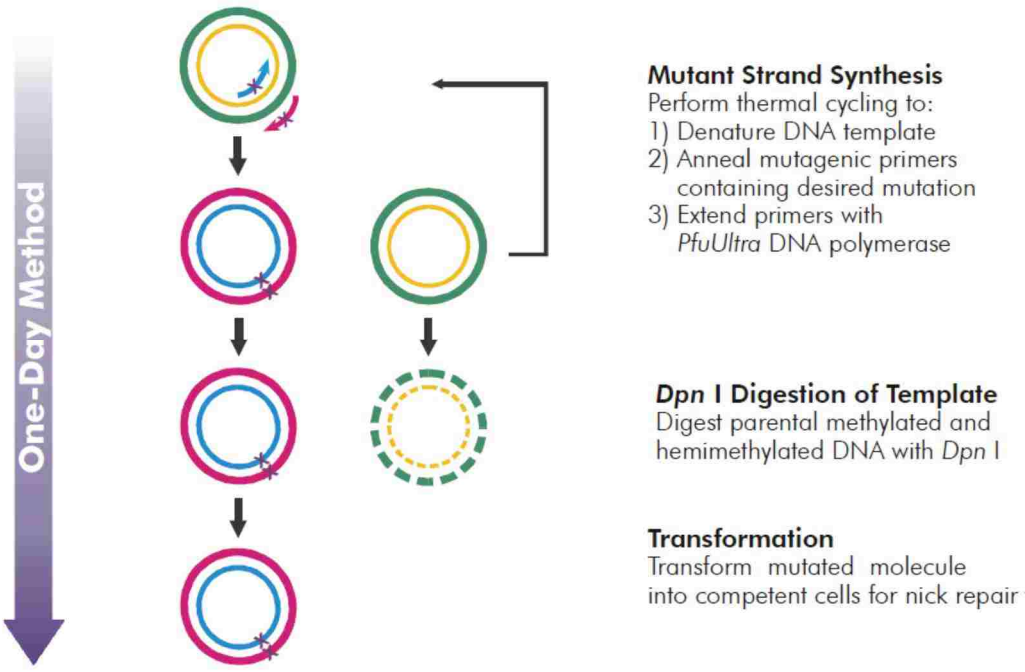

Figure 2.4 Overview of the QuikChange II site-directed mutagenesis method [110].

Table 2.2 Cycling Parameters for the PCR Method [110]

Segment	Cycles	Temperature	Time
1	1	95°C	30 seconds
2	16	95°C	30 seconds
		55°C	1 minute
		68°C	5 minute

2.2.1.2 Protein expression and Purification

The original and mutated plasmids were transformed into *E.coli* strain BL21 [83]. The expression and purification of Mbs were carried out as reported by Mauk et. al [111, 112] and Kitagawa et. al [88]. Wild-type and mutant myoglobin plasmids were transformed into *E.coli* strain BL21 for expression by following the protocol [110]. BL21 cells containing the pGYM plasmid were grown in a superbroth medium (10g/L tryptone, 8g/L yeast extract, 5g/L NaCl) containing 100µg/mL ampicillin for 24 hours. Typical yields of cells from 1L media were ~6g. After harvesting, the cells were resuspended in 4 volumes cold Tris/HCl (20Mm, pH 8.0) and lysozyme (1mg/mL) was added. The suspension was shaken at 4ºC for 3 hours until the cells turned viscous then froze at -80 ºC.

In the frozen cells, 16 U/mL deoxyribonuclease I, 4 U/mL ribonuclease A was added and stirred on ice for 3-4 hours followed by sonication 30s. Then viscous liquid was centrifugated at 7000 rpm for 30 minutes to remove cell debris. Following the 45%-90% ammonium sulfate salt cut, the pellet was resuspended in a minimum amount of 50mM

potassium phosphate buffer, pH 7.0. A Sephadex G-25 column was used to remove all the ammonium sulfate and adjust the pH of the protein solution to 6.0. The running buffer of G25 column was 10mM potassium phosphate, pH 6.0. The protein was then loaded onto a CM52 column that was equilibrated with 10mM potassium phosphate, pH 6.0. The protein was eluted from the column with 50mM potassium phosphate, pH 7.4.

The 2 or 3 fractions from the column which has highest Rz value were pooled and concentrated. The H_2O/D_2O buffer exchange was carried out by concentration at the centrifuge. The solution was concentrated to 0.5mL. Then it was diluted to 2mL with 50mM potassium phosphate buffer, pH 7.4 in D_2O and concentrated to 0.5mL again. This process was repeated for 3 times per day and diluted to 2mL. The solution was put at 4 ºC overnight. The same experiment was done for 3 days to make sure the H/D buffer exchange complete. The final protein solution is 250μM Mb protein with 20% (v/v) glycerol in 50mM potassium phosphate buffer, pH 7.4.

2.2.2 Preparation of oxy-Mb

The oxy-Mb complexes samples were produced by using the vacuum line schematic shown in Figure 2.5.

The Mb samples in the NMR tubes (WG-5M-ECONOMY-7, Wilmad Glass Co., Beuna, NJ) were connected to a vacuum line system and degassed twice. The ferrous Mb was obtained by adding sodium dithionite solution via syringe under an argon atmosphere. The O_2 gas was added to the ferrous Mb solution at -6 ºC and mixed completely. The formation of the ferrous Mb and oxy-Mb were confirmed by UV-vis and rR spectroscopy.

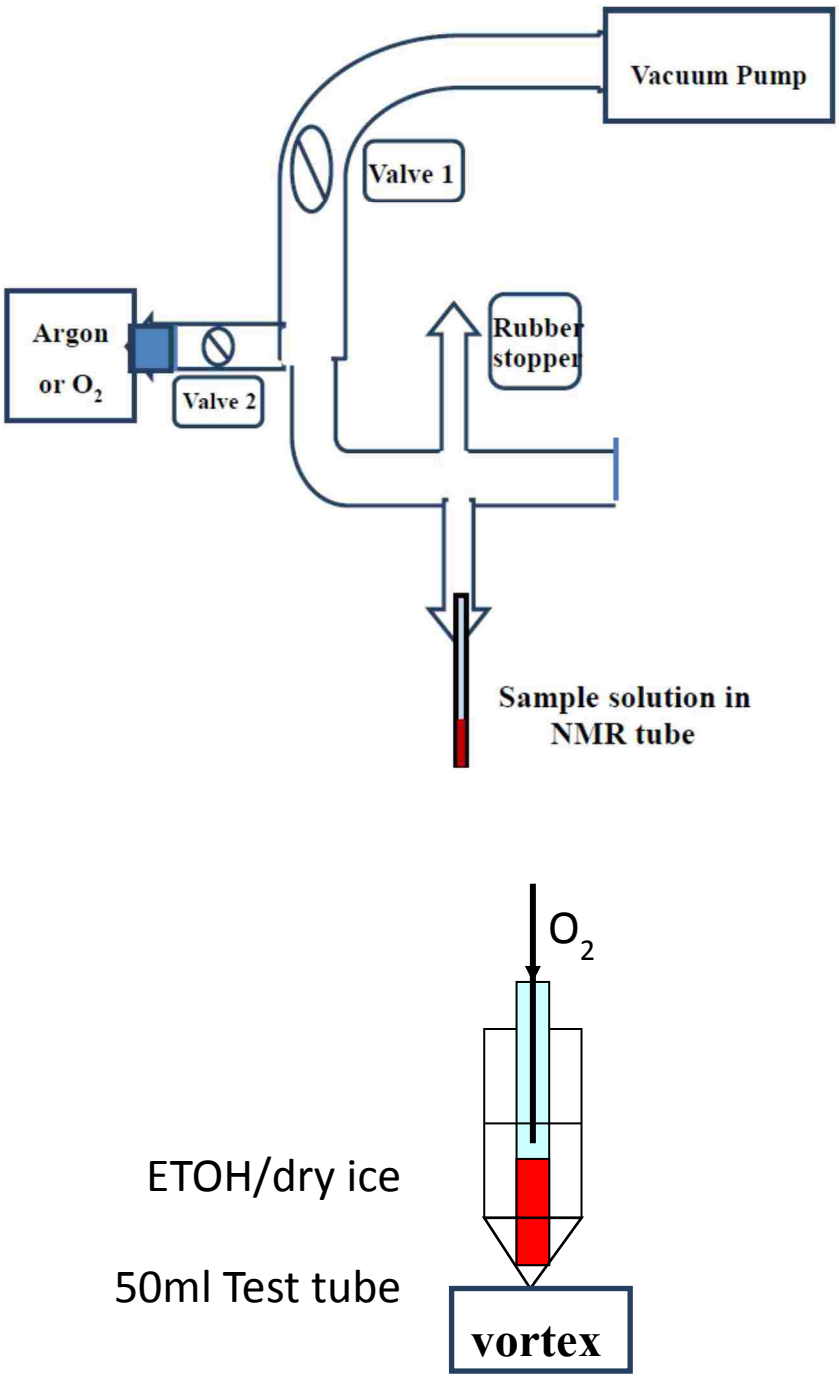

Figure 2.5 The vacuum line system for oxy-protein produce

2.2.3 Resonance Raman study

Resonance Raman spectra were obtained using a Spex 1269 spectrometer equipped with a CCD detector (Spec 10 from Princeton Instruments), at liquid N_2 temperatures (77 K). The wavelength of excitation lines employed for the oxyferrous samples before and after irradiation was 413.1 or 415 nm (Coherent Sabre Kr ion laser) and for ferrous Mb the excitation line was 441.6 nm (Kimmon Model IK4153RC He:Cd laser). Fenchone was used to calibrate all spectra, which were processed with Grams 32/AI (Galactic Industries, Salem, NH). Rayleigh scattering was removed by use of an appropriate Notch filter from Kaiser Optical. The power at the sample was approximately 1.5 mW. The NMR tube containing the sample was spun and the rR spectra were collected at liquid N_2 temperature using 180° (back scattering) geometry in combination with a cylindrical lens. The geometry allows the laser beam focuses on the sample as a line image to avoid local heating (Figure 2.6).

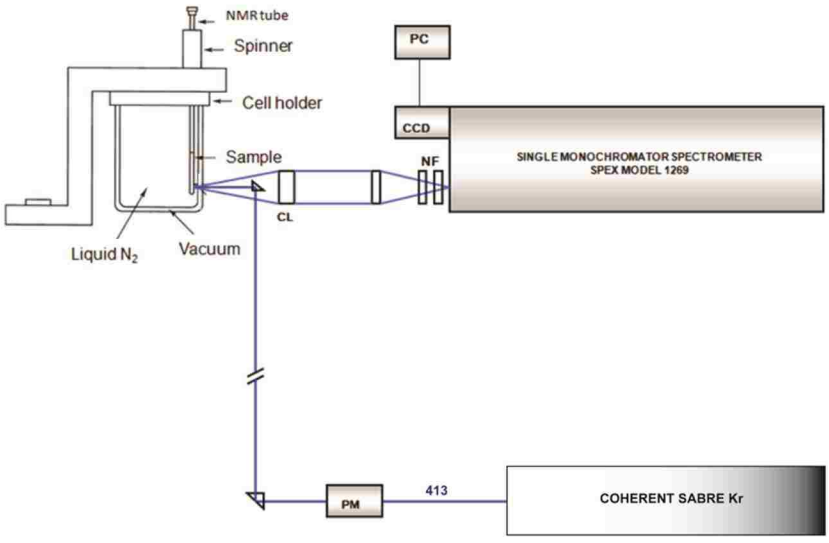

Figure 2.6 Schematic of rR instrumentation

2.3 Results and Discussion

2.3.1 The primer design and sequence check

Horse heart wild-type Mb is contained in plasmid pGYM which was supplied by Dr. Mauk. The plasmids for recombinant myoglobins were also given to us [112].

The gene sequence of Mb is:

ATGGGTCTGTCTGATGGTGAATGGCAGCAGGTTCTGAACGTTTGGGGCAAAGT
TGAAGCTGACATCGCTGGTCACGGTCAAGAAGTCTTGATTCGACTGTTCACCG
GCCACCCGGAAACTCTGGAAAAATTCGATAAATTCAAACACCTGAAAACTGA
AGCTGAAATGAAGGCGTCTGAAGATCTGAAAAAACATGGTACCGTTGTGTTAA
CTGCCCTAGGTGGCATCCTTAAGAAAAAAGGGCACCACGAAGCTGAGCTCAA
ACCGCTTGCGCAATCGCATGCTACTAAACACAAGATCCCGATCAAATACCTGG
AATTCATCTCTGATGCGATCATCCACGTTCTGCATTCTAAACATCCAGGTGACT
TCGGTGCTGACGCTCAGGGTGCTATGACCAAAGCTCTCGAGCTGTTCCGTAAC
GATATCGCTGCTAAGTACAAAGAACTGGGTTTCCAGGGT

As explained in the Introduction, it was planned to make 10 Mb mutants: H64L, H97F, S92A, S92V, S92L, V68S, L29S, L89D, L89V and I107A.

The primers for ten mutants were designed. The rules for primer design are shown as below:

1. Both of the mutagenic primers must contain the desired mutation and anneal to the same sequence on opposite strands of the plasmid;

2. Primers length should be between 25 and 45 bases, with a melting temperature (Tm) of ≥78°C;

3. The desired mutation (deletion or insertion) should be in the middle of the primer with ~10–15 bases of correct sequence on both sides; 4. The primers optimally should have a minimum GC content of 40% and should terminate in one or more C or G bases.

The designs of primers are displayed in Table 2.3; the highlight code is the mutagenesis site.

Table 2.3 List of forward primer for mutagenesis

Name of mutant	Forward primer
H64L	CGTCTGAAGATCTGAAAAAACTTGGTACCGTTGTGTTAACTG
H97F	GCGCAATCGCATGCTACTAAATTCAAGATCCCGATCAAATACC
S92A	GCTCAAACCGCTTGCGCAAGCGCATGCTACTAAAC
S92V	GAGCTCAAACCGCTTGCGCAAGTGCATGCTACTAAACACAA
S92L	CTCAAACCGCTTGCGCAATTGCATGCTACTAAACAC
L89V	GCTGAGCTCAAACCGGTTGCGCAATCGCATGC
L89D	GCTGAGCTCAAACCGGATGCGCAATCGCATGC
V68S	GAAAAAACATGGTACCGTTTCGTTAACTGCCCTAGGTGGC
L29S	TCACGGTCAAGAAGTCTCGATTCGACTGTTCACCGG
I107A	CGATCAAATACCTGGAATTCGCCTCTGATGCGATCATCCACG

The DNA of WT-Mb and mutants was extracted and sent to the Beckman Coulter Genomics for the DNA sequencing. The result is 100% match the map of WT Mb (pGym) and the designs of 10 mutants.

2.3.2 The expression and purification of Mb and mutants

2.3.2.1 The expression and yield of Mbs

Although there were plasmids of WT-Mb and 10 mutants, only WT and 7 mutants could be expressed efficiently. The L89D, L89V and L29S had very low expression so these three mutants were dropped. Much later in my work it was discovered that an early paper had reported that isolation as the cyanide adducts improves yield for L29S mutant of ***human*** Mb, but it was decided not to pursue this further. [104]. In the mutant S92L, the mutagenesis position was the same as mutants S92A and S92V, and the amino acid leucine was also non-polar like alanine and valine. The reason why S92V was similar with S92A.

Thus, only WT-Mb and 6 mutants were expressed. There were 3 distal and 3 proximal side mutants as shown in Table 2.4.

The levels of expression in different protein varied.

Yield of protein = the mass of pure Mb (mg) / the volume of medium (L)

The yield of WT-Mb is 4.9mg/L. As shown in Table 2.3, except for H97F, the expressions of mutants were considerably lower than the WT-Mb.

Table 2.4 List of Mb mutants obtained

	Name	Yield (mg/L)	Rz
Distal mutants	V68S	1.6	5.3
	I107A	2.6	4.8
	H64L	2.0	2.8[a]
Proximal	H97F	4.8	5.6

mutants	S92A	2.3	4.6
	S92L	3.0	4.8

a. the Soret band of mutant H64L at room temperature is at 394nm.

2.3.2.2 The UV-vis spectra of WT-Mb and mutants

As shown in Figure 2.7, all the Soret bands of the Mbs are at 408nm except mutant H64L (vide infra). The Soret band at 408nm and Q-band at 506 and 635nm indicated a typical 6-coordinated ferric high-spin heme [87].The sixth ligand in Mb is water which is stabilized by H-bonding with the His-64 residue. Because the mutant H64L at room temperature is 5-coordinate, the Soret band shifts to 393nm and the extinction coefficient was 103 $mM^{-1}cm^{-1}$ [76, 77], as shown in Figure 2.8 [112]. And at relatively low temperatures (T<-20°C), the Soret band of mutant H64L is at ~410nm which indicated 6-coordinated [77]. In order to make the Soret bands of all the mutants are near the same wavelength to compare the Rz values, the UV spectrum of H64L at low temperature was put in Figure 2.7. The UV-vis spectra of mutant H64L at different temperature is shown in Figure 2.9.

The Rz (A_{408}/A_{280}) value of Mb can show the purity. In Dr. Mauk's paper, they pooled the fractions of WT-Mb that the Rz (A_{408}/A_{280}) was larger than 4.9 [113]. And the Rz (A_{408}/A_{280}) of mutants was 5~5.6 [87, 114]. The Rz (A_{393}/A_{280}) value of mutants H64L is ~3.1 in Dr. Watanabe's paper [115]. The Rz of my samples were 4.6~5.6 except mutant H64L, which was 2.8. The purity of the proteins was considered to be good enough to make deoxy and oxy-samples for rR measurement. The Rz values of each mutants are shown in Table 2.4.

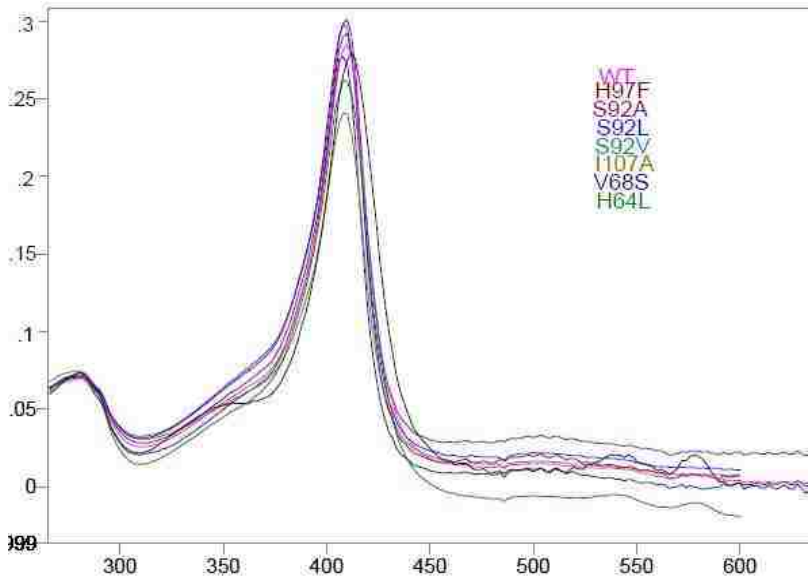

Figure 2.7. Electronic spectra of 200uM ferric wild-type and mutant HH Mbs in 50mM PB buffer at pH 7.4.

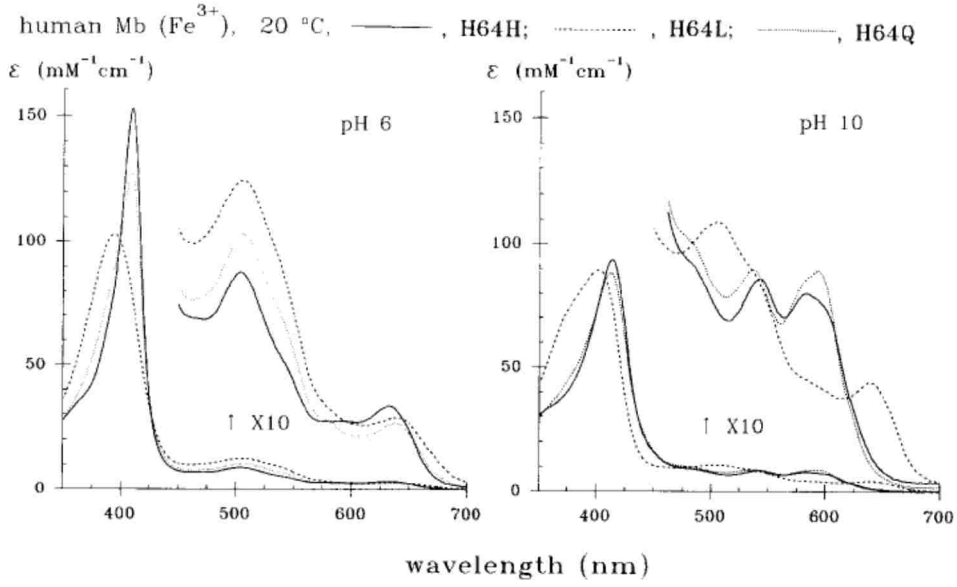

Figure 2.8 Light absorption spectra of ferric recombinant Mb in 0.1 M phosphate buffer, pH 6 (left), and 0.1 M glycine-NaOH buffer, pH 10 (right) [113].

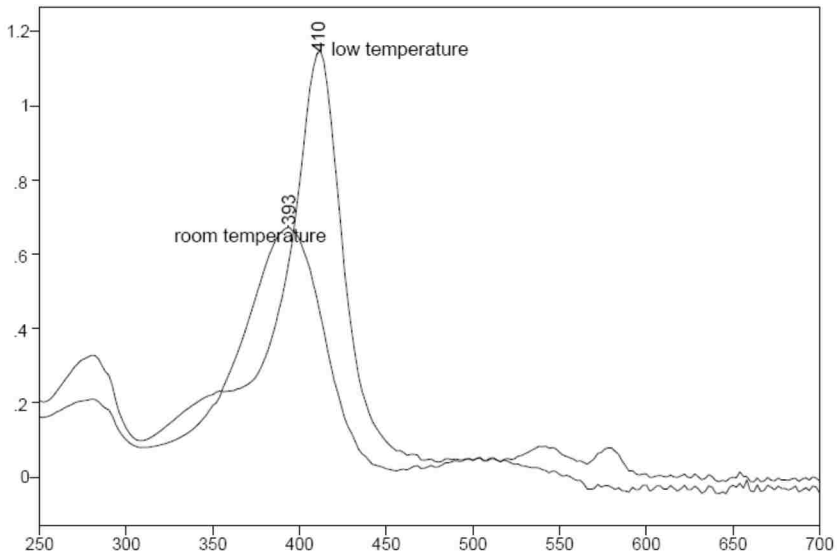

Figure 2.9 Electronic spectra of 500uM ferric mutant H64L in 50mM PB buffer at room temperature and low temperature (T<-20°C) .

2.3.3 Resonance Raman Spectra of deoxy Mb

The rR spectra from 170 to 1030 $cm^{-1}$of the deoxy Mbs are shown in Figure 2.12. The low-frequency spectra were normalized using the ν(Fe-His) band at ~220cm^{-1} which was the stretching mode of the proximal bond between the heme iron and the N_ε (His93) [82, 116]. The assignments of heme modes in this region are based on a large number of reference papers [82, 101, 116] are summarized in Table 2.5**.** The shoulder at ~240 cm^{-1} has been assigned as ν_9, one of the principal totally symmetric modes of the planar heme macrocycle. The weak peak at ~295cm^{-1} was assigned to an out-of-plane mode γ_{16}. The peak at ~300 cm^{-1} was assigned to γ_7, an out-of-plane methine wag mode involving C_a and C_m. The peak at ~335 cm^{-1} is γ_6, assigned to an out-of-plane pyrrole tilting mode. The peak at ~342 cm^{-1} is ν_8, a symmetric macrocycle deformation mode. The peak at 364-371 cm^{-1} is assigned to $\delta(C_\beta C_c C_d)$, a

mode involving bending of the propionate methylene groups. A pair of weak features appeared near 405 and 435 cm^{-1} were referred to as 4- and 2- “vinyl bending” modes, respectively.

The Figure 2.11 showed the rR spectra’s high frequency region of WT and 6 mutants. In this region, the ν_4, ν_2 and ν_3 bands showed the oxidation state and spin state. The ν_4 band at 1355 cm^{-1} showed that the proteins were in the ferrous form and the ν_2 band at 1563 cm^{-1} was a marker of a high-spin state. Actually, in the high frequency region, the wavenumbers of all the bands were not significantly different, reflecting the heme oxidation and spin states are not perturbed by the mutations.

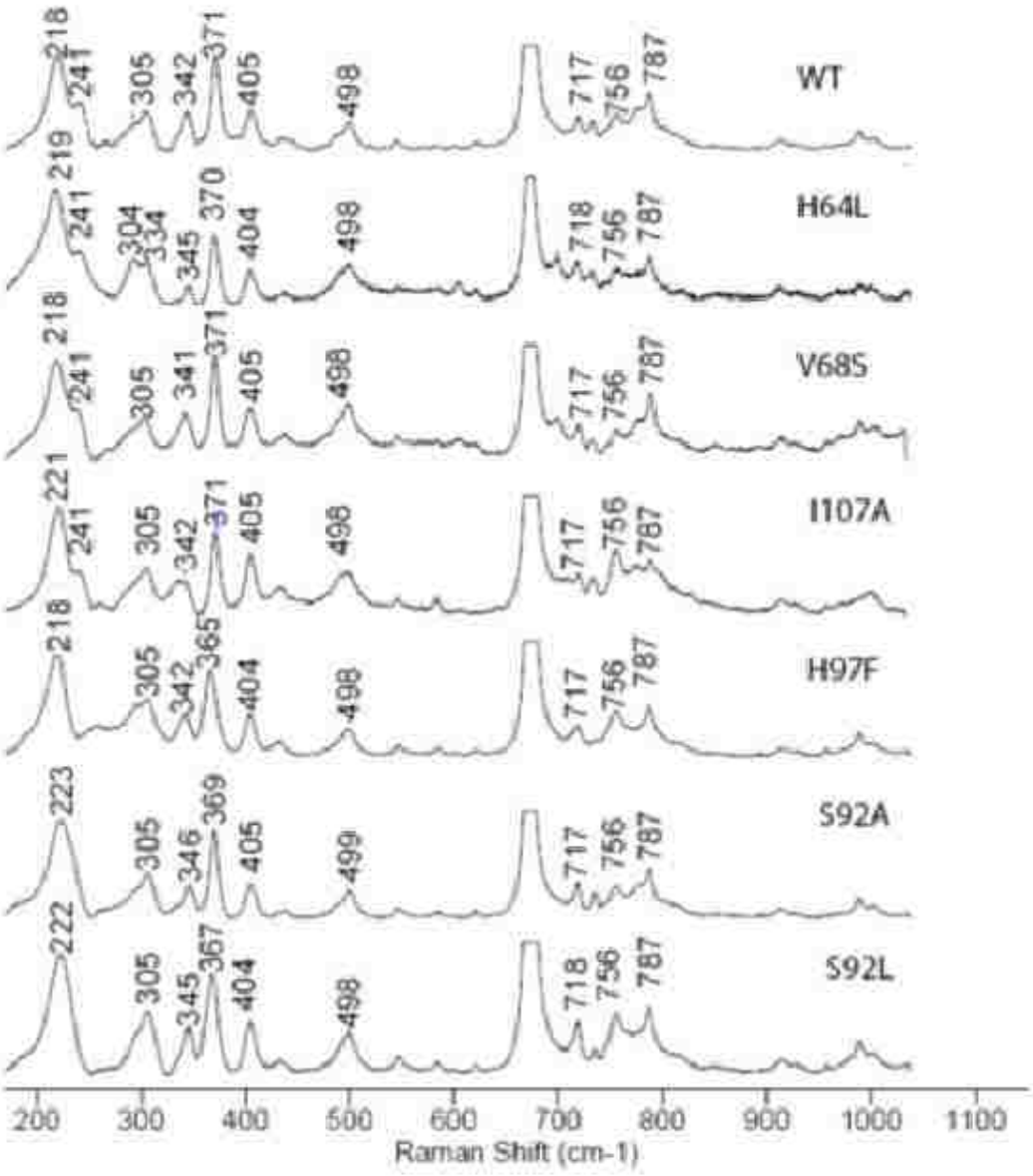

Figure 2.10 The rR spectra of low-frequency region of the 200μM wild-type deoxy-Mb and its mutants. Laser wavelength is 442nm and power is ~3mW. All samples were in 50mM phosphate buffer, pH 7.4 with 20% glycerol. The measurements are finished at room temperature.

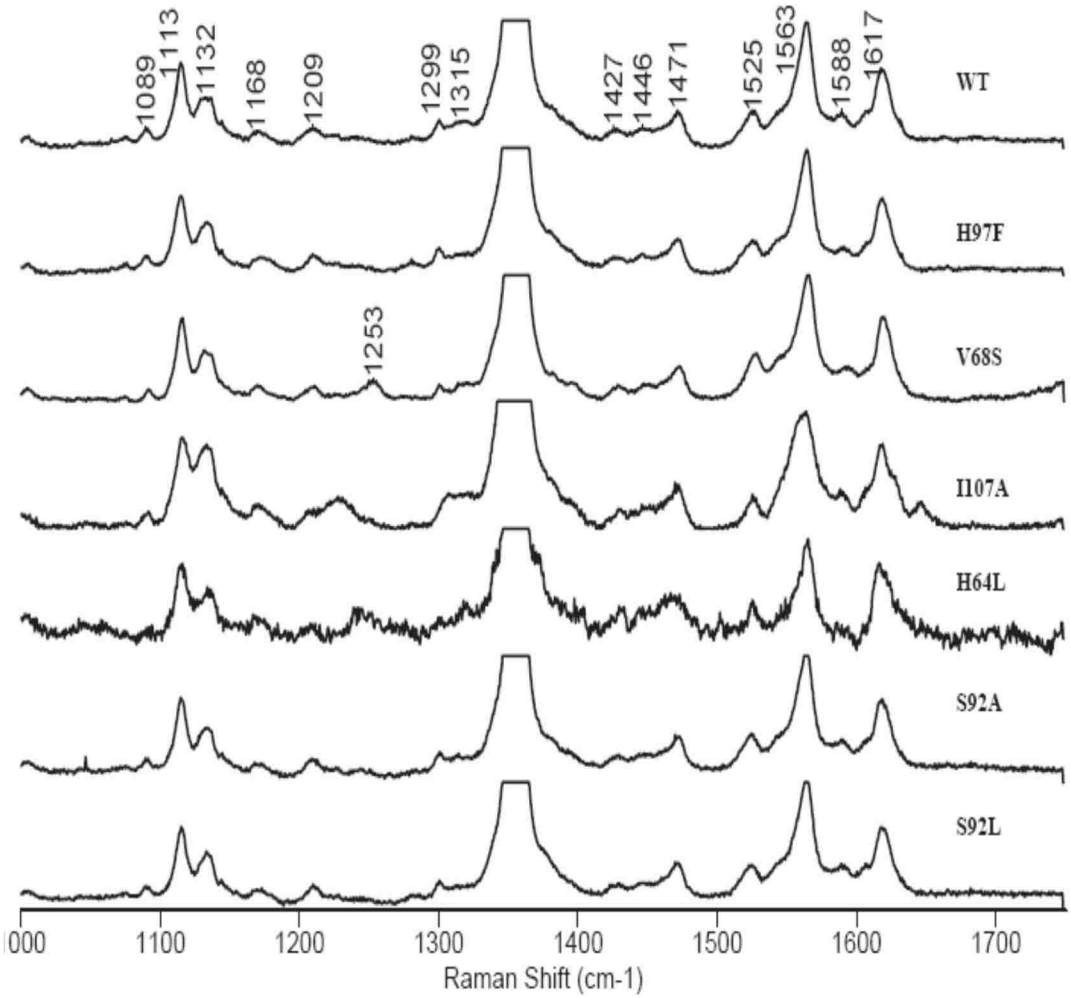

Figure 2.11 The high-frequency region of the 200μM wild-type deoxy-Mb and its mutants. Laser wavelength is 442nm and power is ~3mW. All samples were in 50mM phosphate buffer, pH 7.4 with 20% glycerol. The measurements are finished at room temperature.

2.3.3.1 *ν*(Fe-His) Mode

The H-bonding between the N_ε (His93) and other amino acid residues can affect the structure especially at the heme proximal side. In order to gain insight into it, especially Fe - N_ε (His93) bond character, the resonance Raman spectra of WT-Mb

and its mutants in the deoxy form have been measured. Figure 2.12 shows the low-frequency region of the Raman spectra measured by using 442nm laser.

The values of *v*(Fe-His) in WT-Mb and its mutants are tabulated in Table 2.5. The *v*(Fe-His) band profiles of the WT-Mb and distal side mutants H64L, I107A and V68S peaks were nearly identical, ~220cm^{-1}. As expected, it indicated the mutagenesis on the distal pocket has little effect on the structure around proximal His93. [86].

There were 3 proximal side mutants studied here, H97F, S92A and S92L. The *v*(Fe-His) modes were 218, 224 and 222cm^{-1}, respectively. mutations can be expected to possibly alter the key H-bonds between the $N_{\delta}H$ of the His93 imidazole ring and the hydroxyl side chain of Ser92 and the 7-propionate carboxylate group of the heme, as well as the H-bond interaction between the $N_{\delta}H$ of the His97 imidazole ring and the heme carboxylate, all of which are illustrated in Figure 2.3, above [84]. The rR results obtained here show the actual consequences of the mutations, as follows. In the mutant of H97F, there was no direct interaction change between His93 and the mutation position. Interestingly, the *v*(Fe-His) mode showed an identical value compared to WT-Mb. However, NMR studies of the ferric cyanide complex of this mutant showed that the proximal histidine is rotated ~3° relative to the normally eclipsed orientation in WT, a movement that would have been expected to increase the strength of the Fe-Nhis bond, owing to lowering steric interactions with the pyrrole nitrogens [117].

The deoxy complexes of mutants S92A and S92L had a higher frequency of *v*(Fe-His) than WT-Mb. The higher *v*(Fe-His) frequency reflects a shorter and stronger Fe-His bond. The X-ray structures of the Ser92 mutant (S92D) showed no significant

change in the His93 imidazole tilt angle. [108] In the S92A mutant, NMR data revealed imidazole plane clockwise rotated ~5° compared to the WT-Mb. [103] This was suggested to significantly relieve the steric forces between the pyrrole 2 and 4 nitrogens and the C_δ and C_ε carbons of the imidazole ring [83, 106]. This was argued to be the primary reason why the strength of the Fe-N_{his} bond increased.

While the authors of the above work argued that differences in steric factors between Ala and Leu lead to higher frequency of ν(Fe-H_{his}) for S92A than for S92L, the difference is of borderline significance (1 cm^{-1} in our data), with the main effect seeming to be best attributed to elimination of the H-bonding associated owing to the presence of S92 [83].

Table 2.5. *ν*(Fe-His) of Ferrous Mbs at Room Temperature [101, 102]

	***ν*(Fe-His)**		
Protein	Horse heart[a]	human	SW
WT	218	221[b]	218[c]
H64L	218		
V68S	219		
I107A	220		
H97F	218		218[c]
S92A	224	224[b]	222[c]
S92L	222		

[a]*ν*(Fe-His) data taken from this experiment, [b]*ν*(Fe-His) data taken ref *102*; [c]*ν*(Fe-His) data taken from ref *101*.

2.3.3.2 Heme Modes

a. Propionate-Sensitive Modes: γ_6, ν_8, ν_9, and $\delta(C_\beta C_c C_d)$

The propionate-sensitive modes γ_6, ν_8, ν_9, and $\delta(C_\beta C_c C_d)$ are out-of-plane modes of heme and bending mode of the peripheral groups. They were mainly affected by

proximal side mutations. The data from my experiment are tabulated in Table 2.6. In the WT-Mb, the γ_6, ν_8, ν_9, and $\delta(C_\beta C_c C_d)$ modes were at ~334, 344, 242 and 372cm^{-1}. In the WT-Mb and distal side mutants, all the propionate-sensitive modes there were identical since there was little interaction change between propionate group and these mutation positions.

The ν_9 mode is one of the principal totally symmetric modes of the heme macrocycle; i.e., the ν_9 mode was downshift from 240cm^{-1} to 233cm^{-1} in deuterated deoxy Mb compounds (Mb-D12-deoxy) [116]. From the data of deoxy Mb mutants, the $\delta(C_\beta C_c C_d)$ and ν_9 had an interesting correlation. If the $\delta(C_\beta C_c C_d)$ was higher than 370cm^{-1}, the intensity of the ν_9 band was increased so that it could be observed, near 240cm^{-1} [84].

In the H97F mutants, the $\delta(C_\beta C_c C_d)$ mode was 366cm^{-1} and the ν_9 was downshifted and overlapped with the ν(Fe-His) mode. The broken of His97-heme-7-propionate H-bonding caused a relatively large influence on the orientation of heme plane. The heme plane was rotated away from carbonyl by ~3°according to NMR data [117]. Similarity, in S92A and S92L mutants, the ν_9 bands were downshift and seemed to disappear. The mutations on Ser92 caused partial disruption of His97-heme-7-propionate H-bonding and pushed the His97 imidazole out of pocket. Thus, the $\delta(C_\beta C_c C_d)$ also downshifted like the H97F mutant.

In Mb, the propionates participate in H-bonding with other amino acid residues in the pocket. The $\delta(C_\beta C_c C_d)$ mode will decrease if the H-bonding of the 7-propionate is broken. In addition, ν_9 mode will downshift. Thus, in the H97F, S92A and S92L mutants, the $\delta(C_\beta C_c C_d)$ mode was downshifted by 2-6 cm^{-1} relative to WT and ν_9

mode was shifted to ~232cm^{-1} or lower, probably being buried in the ν(Fe-N_{his}) envelope [30, 46, 48]. In the distal mutants, the $\delta(C_\beta C_c C_d)$ and ν_9 modes had the same profile as in WT-Mb.

b. Vinyl-bending Mode

Two small bands near ~405 and 432cm^{-1} were assigned to vinyl bending modes associated with the 4- and 2-vinyl substituents [116, 120]. Generally, the higher frequency vinyl bending modes are associated with more out-of-plane orientations, with respect to the heme plane, while the lower frequency bending modes are associated with more in-plane orientations. In the case of myoglobin, the lower frequency bending mode was assigned as 4-vinyl bending mode. In the V68S mutant, both vinyl modes were upshifted, while in the I107A mutant, the 2-vinyl bending mode decreased by 4 cm^{-1}, consistent with I107 being closer to the 2- rather than 4-vinyl group.

Table 2.6. rR spectroscopic Features of Ferrous Mb at Room Temperature

Protein	γ_6	ν_8	ν_9	$\delta(C_\beta C_c C_d)$	δ(4-vinyl)	δ(2-vinyl)	γ_7	γ_{16}
WT	334	344	242	372	405	435	303	295
H64L	335	345	241	370	405	437	304	293
V68S	X	342	242	373	410	439	303	292
I107A	334	342	242	371	406	433	305	289
H97F	X	342	X	366	404	432	305	296
S92A	335	347	229	370	405	437	305	295
S92L	336	345	X	368	405	437	305	294

2.3.4 Oxy-, peroxo- and hydroperoxo-Mb

2.3.4.1 Oxy-Mb

a. High-frequency region

The Figure 2.12 shows the rR spectra (high frequency region) of oxygenated forms of WT and 6 mutants. The v_4 band at 1379 cm^{-1} showed the proteins were oxy-complexes, with no residual deoxy present and v_2 band at 1588 cm^{-1} was assigned as low-spin state [82]. The enlarged view of this region is displayed in Figure 2.13. The weak band around 1476cm-1 comes from the glycerol. The v_2 and v_3 modes are near 1589 and 1509cm^{-1}, respectively, which corresponds to low-spin ferric heme, consistent with a ferric-superoxide formulation. Actually, in the high frequency region, the frequencies of all the bands

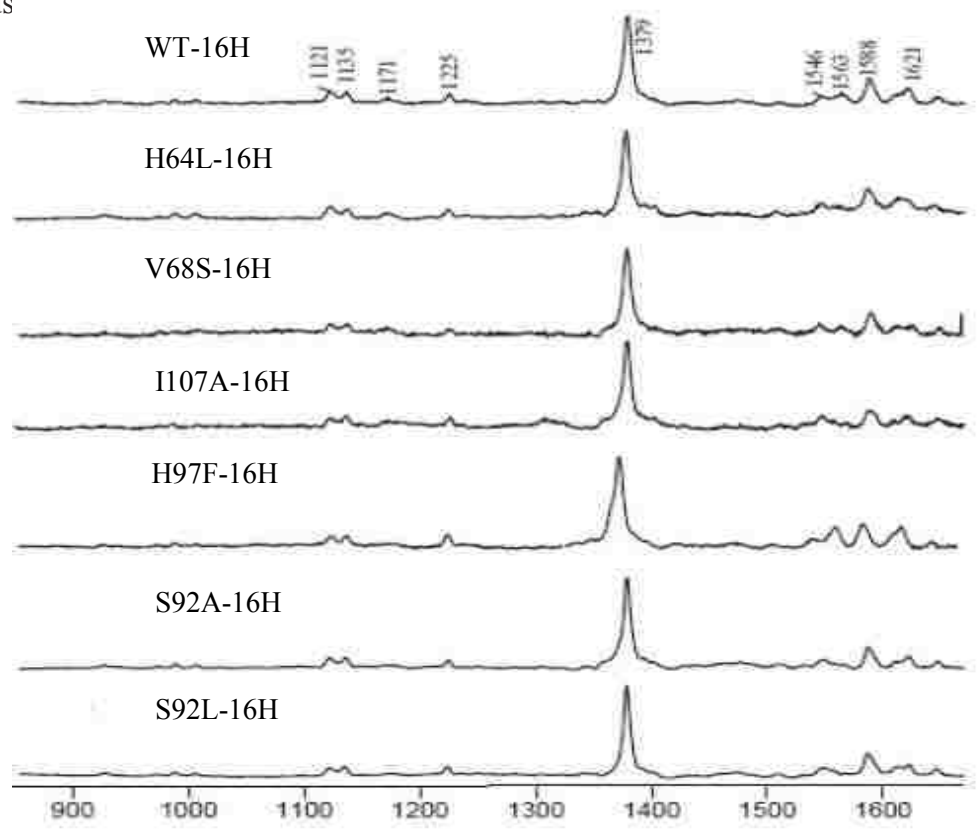

Figure 2.12 The high-frequency region of the 200μM wild-type oxy-Mb and its mutants. Laser wavelength is 415nm and power is ~1.3mW. All samples were in 50mM phosphate buffer, pH 7.4 with 20% glycerol. The measurements are done at 77K.

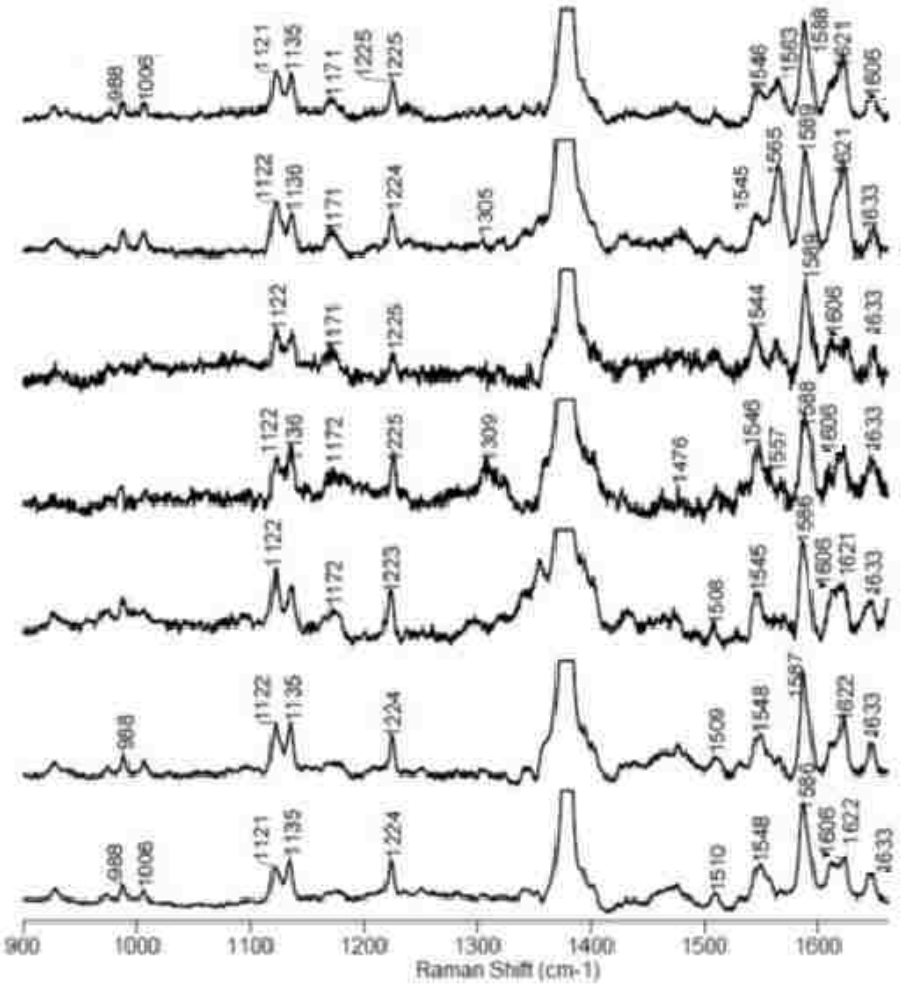

Figure 2.13 Enlarged view of high-frequency region of the 200μM wild-type oxy-Mb and its mutants. Laser wavelength is 415nm and power is ~1.3mW. All samples were in 50mM phosphate buffer, pH 7.4 with 20% glycerol. The measurements are finished at 77K.

b. Low-frequency region

(i) Heme modes

The Raman spectra from 170 to 1130cm^{-1}of the deoxy Mbs are shown in Figure 2.14 The low-frequency spectra were normalized using the ν_7 band at ~675cm^{-1}, which was the most intense band in the spectra, where the heme mode changes were very clear, all

of the values being collected in Table 2.6, the assignments being established in a previous work [116]. The shoulder at ~255 cm^{-1} (WT) was assigned as ν_9, one of the principal totally symmetric modes of pyrrole planar, downshifting by only 2-5 cm^{-1} for the mutations [76,82 and this work]. This, and the other in-plane and out-of-plane (γ_7 near 305 cm^{-1}) modes listed in Table 2.6, have been assigned based on previous studies employing isotopically labelled protohemes [116]. Generally, no significant or systematic changes could be detected for the heme modes.

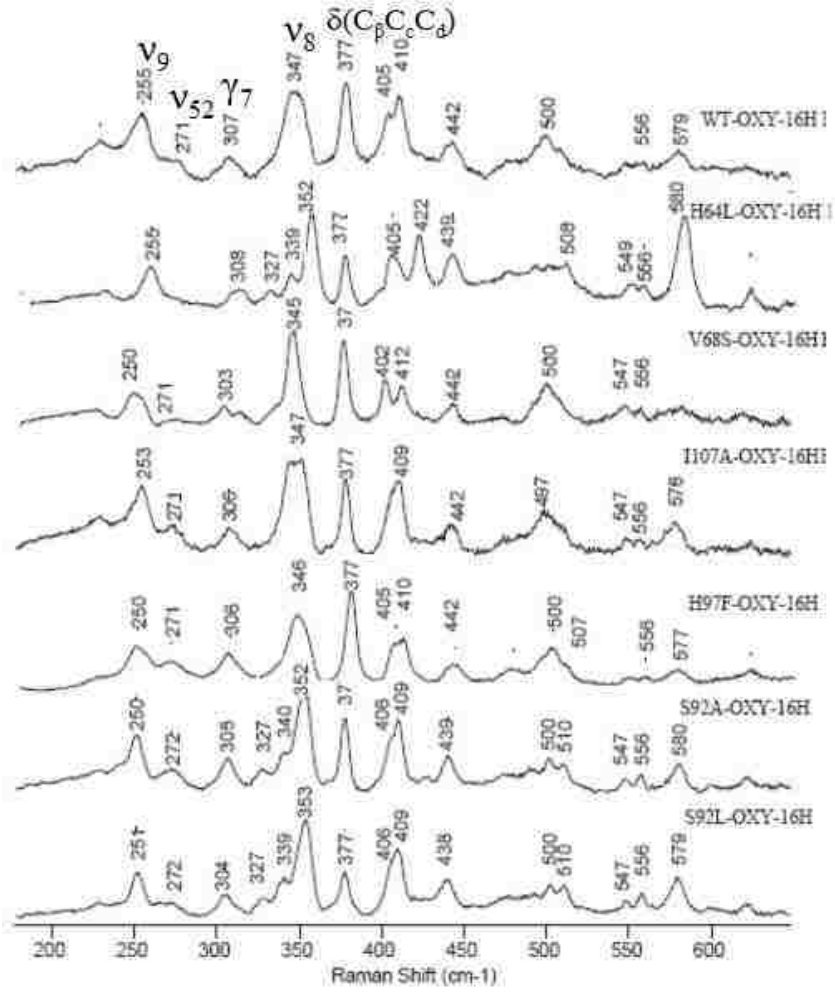

Figure 2.14 The rR spectra of low-frequency region of the 200μM wild-type oxy-Mb and its mutants. Laser wavelength is 415nm and power is ~1.3mW. All samples were in 50mM phosphate buffer, pH 7.4 with 20% glycerol. The measurements are finished at 77K.

(ii) Fe-O-O modes

The low frequency rR spectra of all of the oxygen adducts of the mutants are shown in Figure 2.14. In order to better characterize the rather weak ν(Fe-O) stretching modes, $^{16}O_2$-$^{18}O_2$ difference spectra were generated from the raw data and are shown in Figure 2.15, with the extracted frequencies being given in Table 2.7. The *ν*(Fe-O) stretching mode of the oxygenated form was observed as a relatively weak feature at 578-580cm^{-1}. As shown in the Table 2.9 and Figure 2.14, the *ν*(Fe-O) frequency of these 6 mutants oxy-Mb were insignificantly different from that of the WT oxy-Mb [76], an unexpected result, since the targeted residues are believed to be involved in key H-bonding interactions that can affect active site stricture and the status of the Fe-O-O fragment.

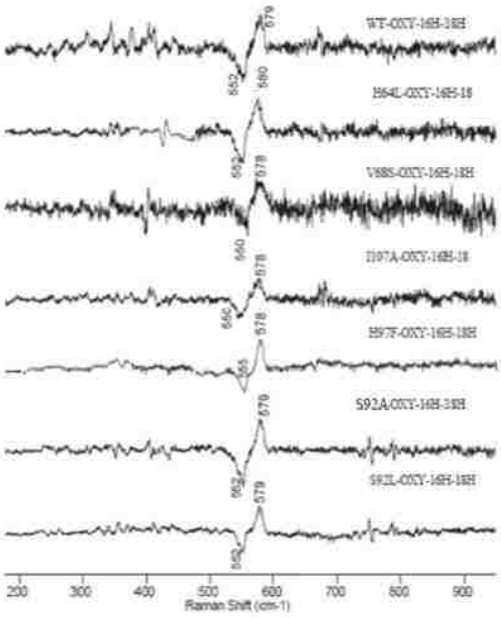

Figure 2.15 Difference spectra of the low-frequency region of the visible resonance-enhanced Raman spectra from 190 to 480 cm^{-1} of the oxy-Mbs.

However, two mutants showed slightly different behavior. The H64L mutant exhibited an especially intense ν(Fe-O) mode and an unusually intense δ(Fe-O-O) bending mode. On the other hand, the intensity of *ν*(Fe-O) stretching mode in another distal side mutant,V68S, is much less intense than other mutants. Consequently, experiments conducted for those two mutants were repeated. The new rR spectra in the low frequency regions of those two oxy-Mb mutants are shown in Figure 2.16.

The new spectra have higher signal to noise ratio and they confirm the *ν*(Fe-O) stretching mode of oxy-V68S and oxy-H64L mutant are both at 580 cm^{-1}. The bending mode of Fe-O-O in oxy-H64L mutant is at 422 cm^{-1} and the new data for the V68S still fail to show an enhanced δ(Fe-O-O) bending mode and confirm the very low intensity of the ν(Fe-O) mode. This is most reasonably attributed to a much more rapid auto-oxidation rate that occurs because of the more hydrophilic distal pocket resulting from introduction of another CH-O-H group.

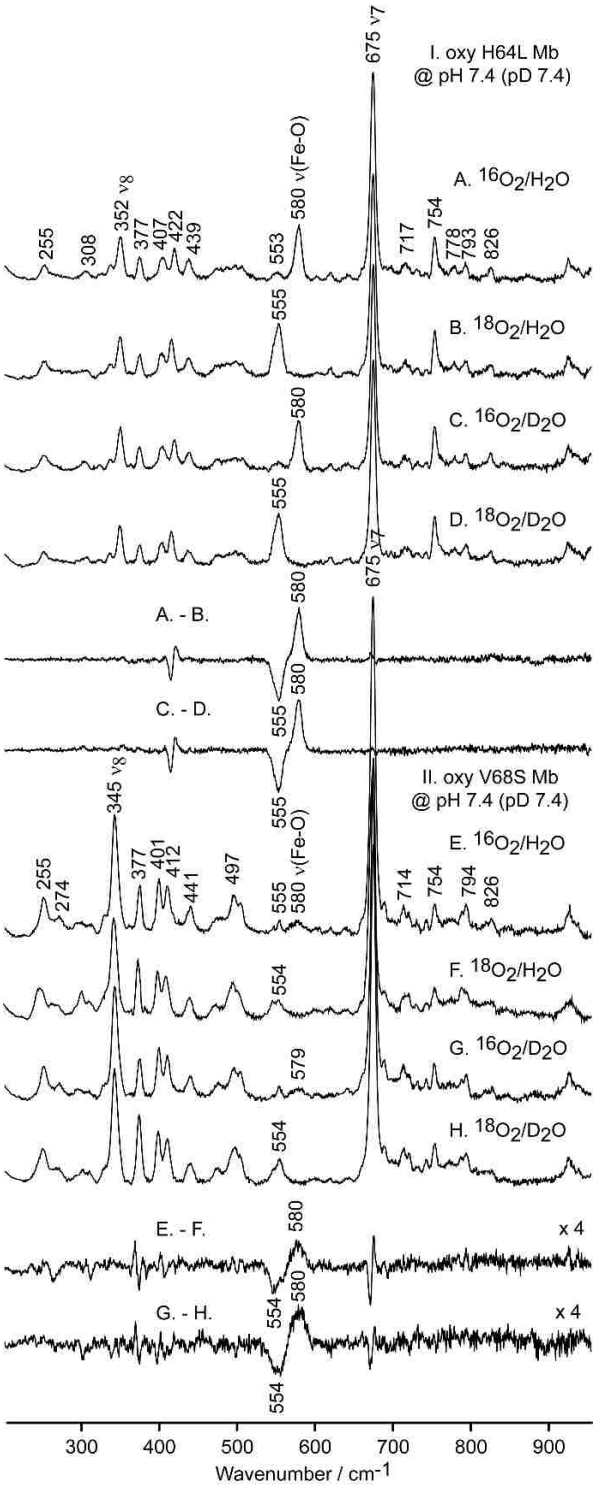

Figure 2.16. The low frequency rR spectra of oxy Mb mutants. Panel I – samples of oxy H64L Mb mutantat pH 7.4 (pD 7.4), A) $^{16}O_2/H_2O$, B) $^{18}O_2/H_2O$, C) $^{16}O_2/D_2O$, A) $^{18}O_2/D_2O$, and their difference traces. Panel II – samples of oxy V68S mb mutant at pH 7.4 (pD 7.4), E) $^{16}O_2/H_2O$, F) $^{18}O_2/H_2O$, G) $^{16}O_2/D_2O$, H) $^{18}O_2/D_2O$ and their difference traces. Samples were measured at 77 K, total collection time for each spectrum was 60 min, excitation line was 413.1 nm, laser power was 1.0 mW

Table 2.7. rR spectroscopic Features of oxy-Mbs at 77K

Protein	γ_7	ν_8	ν_9	$\delta(C_\beta C_c C_d)$	δ(4-vinyl)	δ(2-vinyl)
WT	307	347	255	377	410	442
H64L	308	352	255	377	405	439
V68S	303	345	250	377	412	442
I107A	306	347	253	377	409	442
H97F	306	346	250	377	410	442
S92A	305	352	250	377	409	439
S92L	304	352	251	377	409	438

Table 2.8. rR spectroscopic Features of *ν*(Fe-O) at 77K

	ν_{Fe-O}	
Protein	$^{16}O^{16}O$	$^{18}O^{18}O$
WT	579	552
H64L	580	555
V68S	580	554
I107A	578	550
H97F	578	552
S92A	579	552
S92L	579	552

2.3.4.2 Irradiated Oxy-Mb; the peroxo- or hydroperoxo- derivatives of Mb

a. High-frequency region

The Figure 2.17 shows the rR spectra (high frequency region) the irradiated forms of oxygenated WT and 6 mutants. These samples were annealed at 185K. It is noted that in the Figure, the ν_4 band at ~1379 cm^{-1} can contain contributions from dioxy-Mb, peroxo- and hydroperoxo-Mb. The ν_4 modes appearing between 1356 and 1362 cm^{-1} are ascribed to ferrous forms, with the 1362 cm^{-1} feature arising from cryoreductuion of the autoxidized Mb. This is supported by data shown in Figure 2.18.

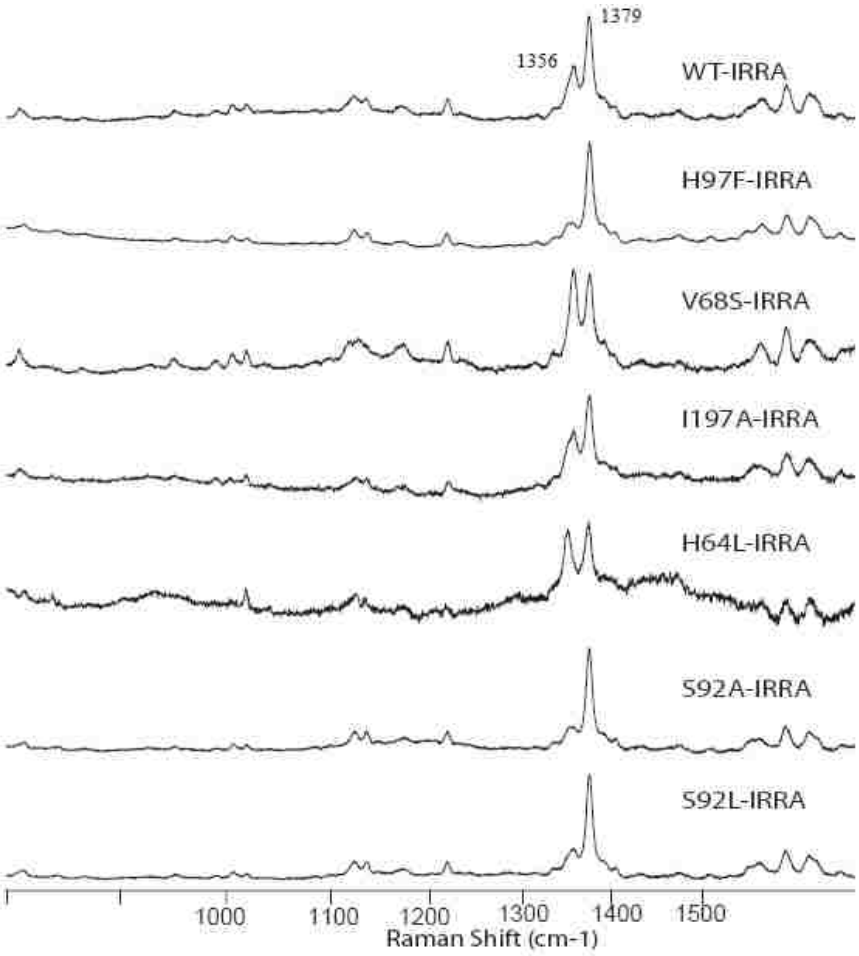

Figure 2.17 The high-frequency region of the 200μM irradiated wild-type oxy-Mb and its mutants. Laser wavelength is 415nm and power is ~1.3mW. All samples were in 50mM phosphate buffer, pH 7.4 with 20% glycerol. The samples were annealed at 180K, but the measurements are finished at 77K.

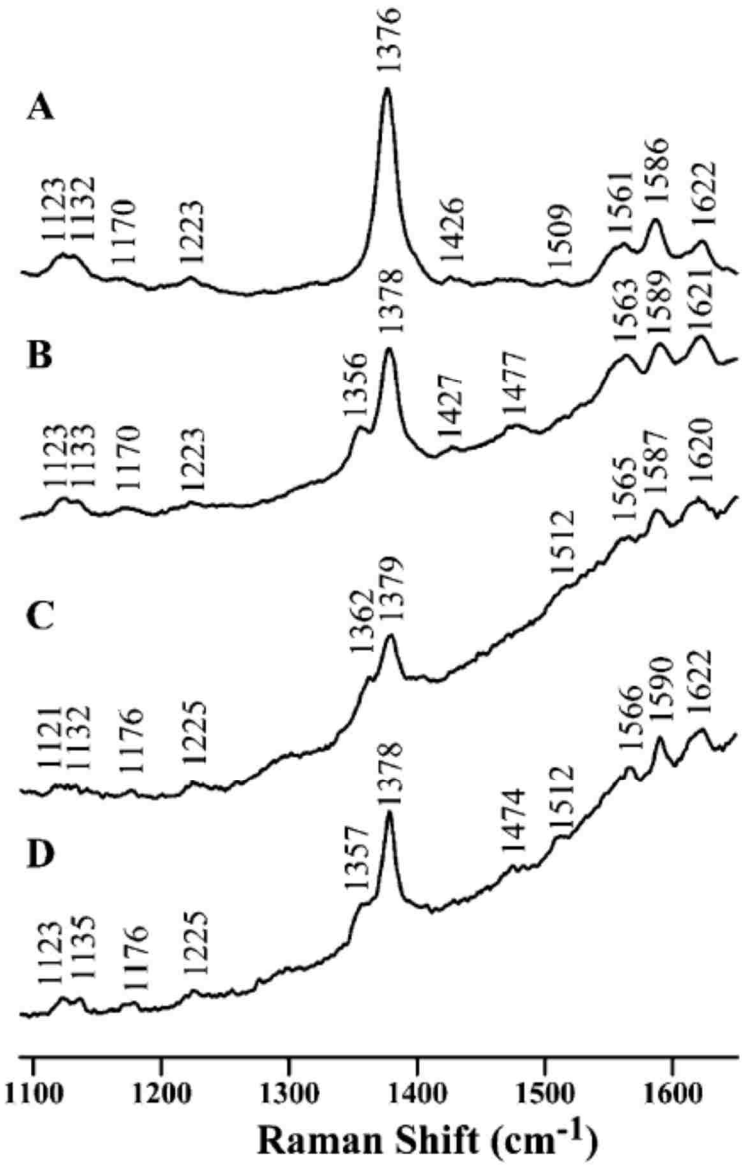

Figure 2.18 High-frequency rR spectra of oxy-Mb (50% glycerol) at 413 nm excitation. (a) At room temperature. (b) At 77 K, where some of the oxy-form has been photolyzed (c) Irradiated, at 77K, with the 1362 cm^{-1} being attributed to cryoreduction of an autoxidized ferric protein.. (d) Sample in C, annealed to 185 K, measured at 77 K; i.e., 1362 cm^{-1} feature converted to 1357 cm^{-1} [81].

b. Low-frequency region

In the low-frequency region, the most interesting feature was *ν*(Fe-O) which could possibly vary significantly for the different forms of the oxygenated intermediates of Mbs; i.e., peroxo- and hydroperoxo- forms. As shown in Figures 2.19 and 2.20, the *ν*(Fe-^{16}O) modes for WT, H97F, I107A, S92A and S92L mutants in H_2O- based buffer, are all near 616cm^{-1}, downshifted to ~613cm^{-1} for samples prepared in D_2O-based buffers, as expected for hydroperoxo complexes [81]. On the other hand, H64L shows only strong bands at 580 and 422 cm^{-1}, characteristic of the dioxygen adduct, while the V68S shows only a very weak band near 600 cm^{-1}, a value consistent with that expected for a cryotrapped peroxo-species; i.e., for peroxo- P450s the ν(Fe-O) typically appears ~10 cm^{-1} below that for the corresponding hydroperoxo form [86]. As mentioned earlier, based on unusual behavior of the H64L and V

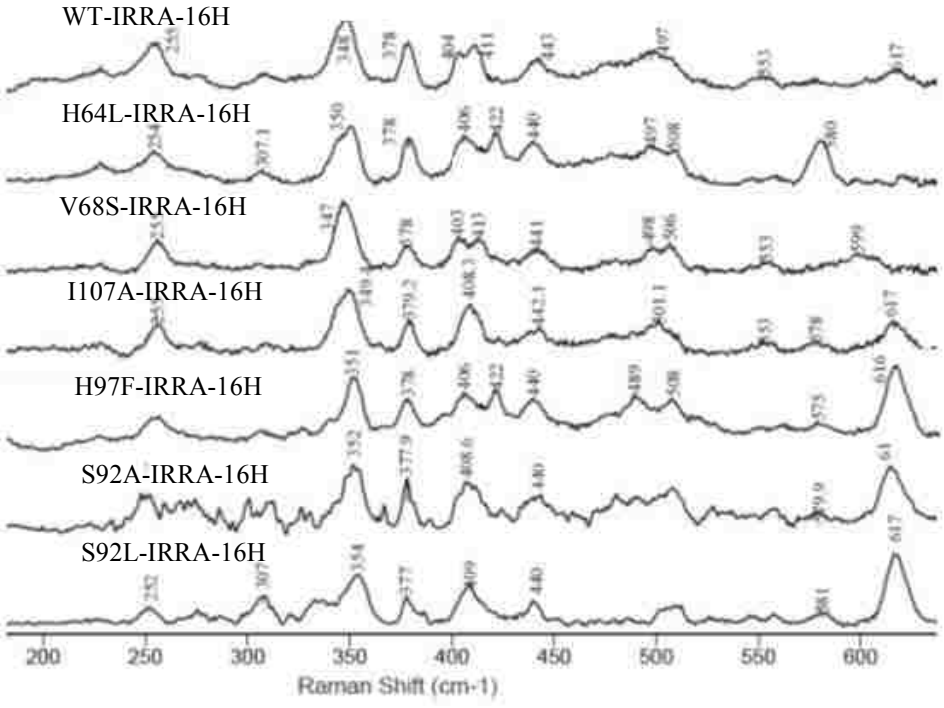

Figure 2.19 Enlarged view of the low-frequency region of the visible resonance-enhanced Raman spectra from 190 to 650 cm^{-1} of the irradiated oxy-Mbs.

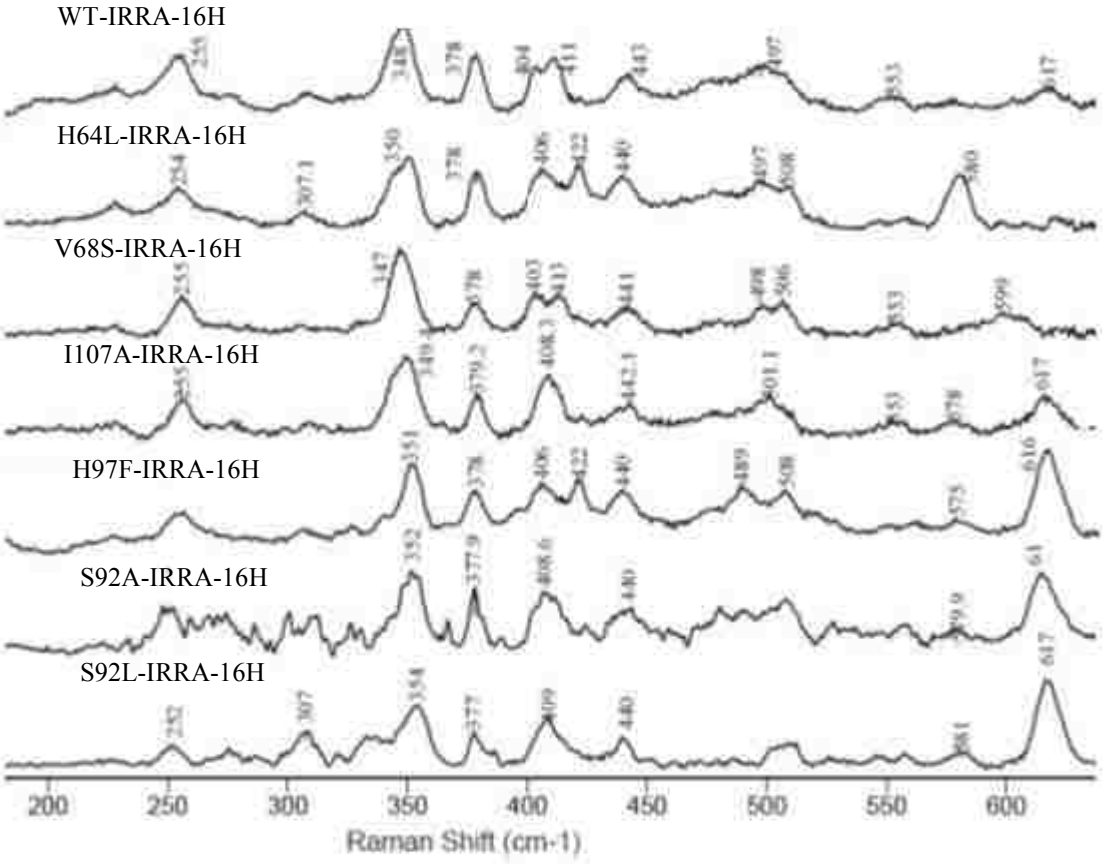

Figure 2.20 Difference spectra of the low-frequency region from 300 to 900 cm^{-1} of the irradiated oxy-Mbs

The new rR spectra of the cryoreduced samples of H64L andV68S mutants are shown in Figure 2.21, which reinforces the point that in the ecryoreduced dioxygen adduct of H64L, the only detectable species is apparently the dioxygen adduct. The lack of any new observable modes is most reasonably attributed to an apparently extreme instability of the peroxo-/hydroperoxo- form of this mutant, presumably owing to a very non-polar distal pocket. The essential point is that rR results confirm the absence of a stable cryoreduced form. The spectrum of the V68S mutant, on the other hand, shows only a very weak band appearing near 599 cm^{-1}, noting the significant finding that it

exhbits no shift in deuterated solvent. The most reasonable assignment for this feature is to a trapped peroxo- species. In support of this, it is pointed out that work done with cytochrome P450s showed that the ν(Fe-O) for a peroxo- intermediate, seen at ~553 cm^{-1} occurs ~11 cm^{-1} lower than that for the corresponding hydroperoxo form.[34] Here, the 599 cm^{-1} feature is 18 cm^{-1} lower than its corresponding hydroperoxo- form.

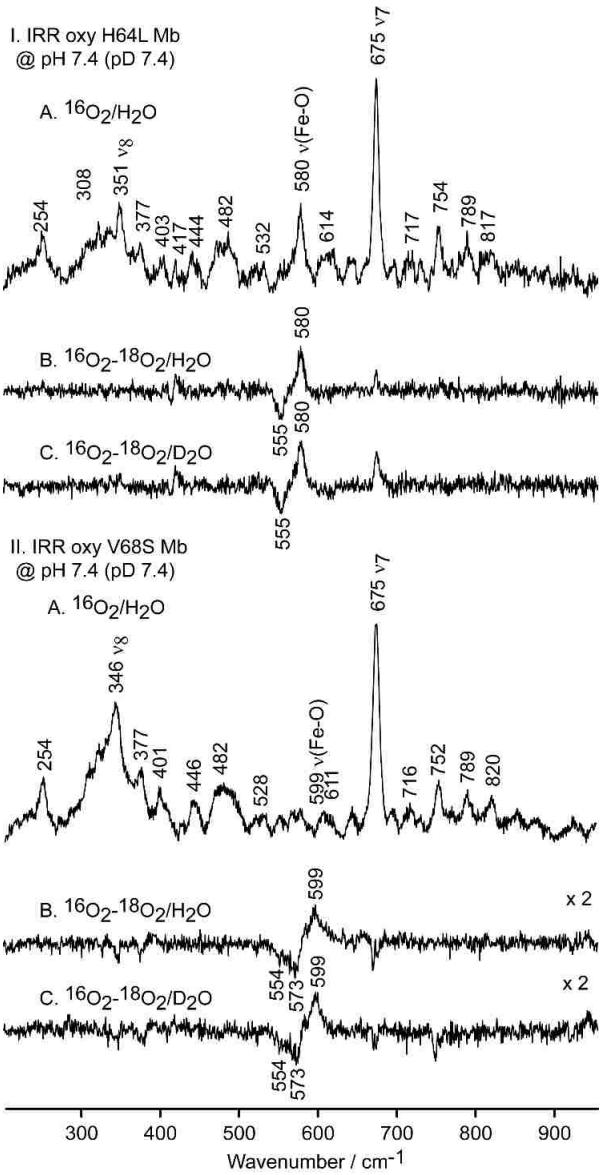

Figure 2.21. The low frequency rR spectra of irradiated oxy Mb mutants. Panel I - samples of H64L Mb at pH 7.4 (pD 7.4), A) $^{16}O_2/H_2O$, B) the $^{16}O_2$-$^{18}O_2$ difference trace in H_2O buffer, C) the $^{16}O_2$-$^{18}O_2$ difference trace in D_2O buffer. Panel II – samples of V68S Mb at pH 7.4 (pD 7.4), A) $^{16}O_2/H_2O$, B) the $^{16}O_2$-$^{18}O_2$ difference trace in H_2O buffer, C) the $^{16}O_2$-$^{18}O_2$ difference trace in D_2O

buffer. Samples were measured at 77 K, total collection time for each spectrum was 1-2 hrs, excitation line was 413.1 nm, laser power was 1.0 mW.

As in case of WT Mb, these mutants' samples were annealed to higher temperatures. Fig. 2.22 shows low frequency rR spectra of $^{16}O_2/H_2O$ samples of H64L (Panel I) and V68S (Panel II) annealed to 180 K and 200 K. Interestingly, the 580 cm^{-1} mode in the spectra of annealed H64L mutant seems to maintain its strong relative intensity as compared to the ν_7 mode; such persistence in higher temperatures would be expected for relatively stable oxy precursor. The $^{16}O_2$-$^{18}O_2$ difference patterns of 180 K and 200 K annealed samples of V68S mutant show no signs of hydroperoxo intermediate; in fact, there are no oxygen sensitive features observed in either of these traces. This behavior, occurring in a relatively polar distal pocket is most reasonably interpreted as being due to either proton assisted dissociation of hydrogen peroxide or perhaps very efficient O-O bond cleavage to generate an unstable ferryl species. In closing this section it is important to stress that although the peroxo-/hydroperoxo-/ferryl species were not observed simultaneously in the case of these myoglobin mutants, the combination of annealing procedures and the use of deuterated solvents permits one to readily distinguish among the different types of intermediates.

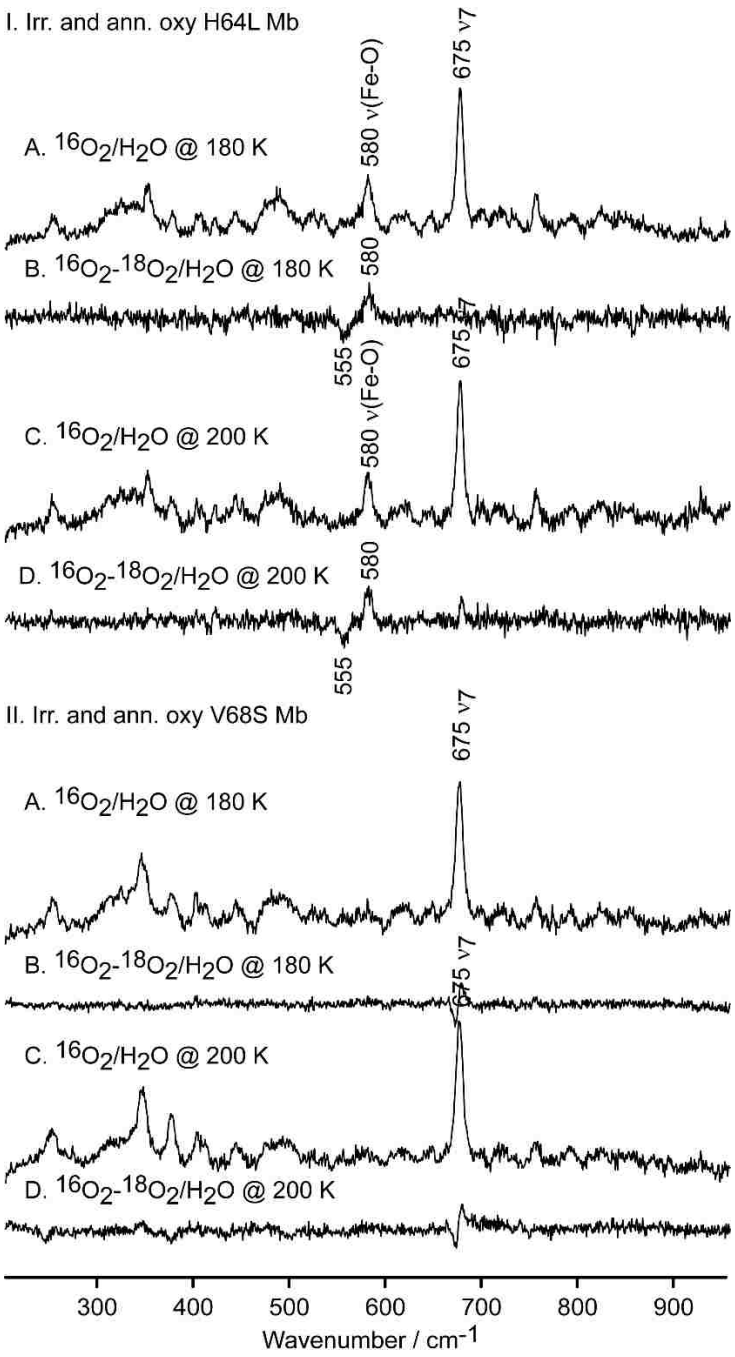

Figure 2.22. The low frequency rR spectra of irradiated and annelaed samples of oxy Mb mutants at pH 7.4. Panel I – H64L Mb mutant, A) $^{16}O_2/H_2O$ sample annealed to 180 K, B) the $^{16}O_2$-$^{18}O_2$ difference trace in H_2O buffer of samples annealed to 180 K, C) $^{16}O_2/H_2O$ sample annealed to 200 K, B) the $^{16}O_2$-$^{18}O_2$ difference trace in H_2O buffer of samples annealed to 200 K. Panel II – V68S Mb mutant, A) $^{16}O_2/H_2O$ sample annealed to 180 K, B) the $^{16}O_2$-$^{18}O_2$ difference trace in H_2O buffer of samples annealed to 180 K, C) $^{16}O_2/H_2O$ sample annealed to 200 K, B) the $^{16}O_2$-$^{18}O_2$ difference trace in H_2O buffer of samples annealed to 200 K. Samples were measured at 77 K,

total collection time for each spectrum was 2 hrs, excitation line was 413.1 nm, laser power was 1.0 mW.

Table 2.9. rR spectroscopic Features of ν(Fe-O) in irradiated samples at 77K

	ν_{Fe-O}	
Protein	$^{16}O^{16}O$	$^{18}O^{18}O$
WT	617	590
H64L	580	590
V68S	599	573
I107A	617	590
H97F	616	590
S92A	615	590
S92L	616	590

2.3.4.3 Effects of pH on cryoradiolysis of oxyMb

The first rR study of cryoreduced oxy myoglobin revealed a ν(Fe-O) mode observed at 617 cm^{-1} that exhibited a 25 cm^{-1} downshift upon $^{18}O_2$ substitution, as well as a 5 cm^{-1} downshift in D_2O buffer [81]. These telltale shifts identify this as a hydroperoxo-species, owing to the H/D sensitivity, implying that the fleeting peroxo- precursor was not trapped under these conditions (vide infra). The ν(Fe-O) mode of this newly generated intermediates is upshifted by 39 cm^{-1} to higher frequency from its oxy-precursor (the ν(Fe-O) of oxyMb is observed at 578 cm^{-1}). One possible complication is that the original studies were performed for samples dissolved in phosphate buffer (pH= 7.4), which can experience substantial drops in pH at very low temperatures [115, 116]. Thus, it was decided to conduct further studies here at higher pH. Boric acid based buffer is much less temperature sensitive, and as such was chosen in this study to probe the formation of peroxo-/hydroperoxo- intermediates under basic conditions so as to explore the possibility of stabilizing the peroxo- intermediate in an environment containing lower proton concentration.

Before considering the effects of increased pH on formation of the hydroperoxo- species, it is noted there is a small effect on the dioxy-Mb precursor. Thus, Fig. 2.23 shows the rR spectra of oxy samples of myoglobin generated in boric buffers at pH 8.5 and 9.5 (Panel I and II, respectively). As can be seen from absolute spectra as well as difference patterns, the increase of pH causes a slight downshift of the ν(Fe-O) modes; e.g., the ν(Fe-O) stretching mode moves from 578 cm^{-1} at pH 7.4 (not shown)[29] to 576 cm^{-1} at 8.5 and further to 574 cm^{-1} at pH 9.5. In both cases the ν(Fe-O) modes exhibit expected 27-28 cm^{-1} down shift upon $^{18}O_2$ substitution and no sensitivity to the D_2O exchange. These slight shifts of ν(Fe-O) modes to lower frequencies with increasing pH might reflect changes in the distal heme pocket environment. It is noted that there are no significant alterations in heme modes nor for the modes associated with heme peripheral groups caused by changes in pH.

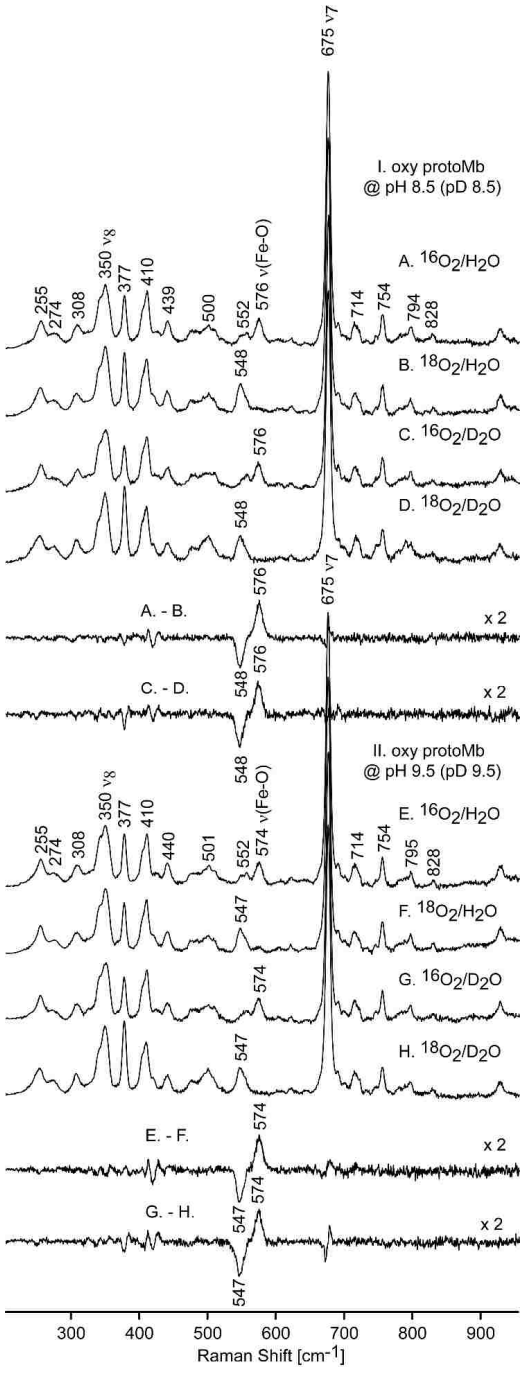

Figure 2.23 The low frequency rR spectra of oxy protoMb at different pH. Panel I – samples at pH 8.5 (pD 8.5), A) $^{16}O_2/H_2O$, B) $^{18}O_2/H_2O$, C) $^{16}O_2/D_2O$, A) $^{18}O_2/D_2O$, and their difference traces. Panel II – samples at pH 9.5 (pD 9.5), E) $^{16}O_2/H_2O$, F) $^{18}O_2/H_2O$, G) $^{16}O_2/D_2O$, H) $^{18}O_2/D_2O$ and their difference traces. Samples were measured at 77 K, total collection time for each spectrum was 30 min, excitation line was 413.1 nm, laser power was 1.0 mW.

The rR spectra of γ-irradiated $^{16}O_2/H_2O$ samples of Mb at pH 8.5 are shown in Figure 2.24 (traces A in panel I). The $^{16}O_2$-$^{18}O_2$ difference traces in H_2O and D_2O buffers (Panel I, traces B and C, respectively) show that oxygen sensitive mode seen at 620 cm^{-1} exhibits a 25 cm^{-1} downshift upon $^{16/18}O$ exchange and a telltale 4 cm^{-1} sensitivity in D_2O buffers, i.e.; again, this mode is most reasonably associated with the ν(Fe-O) stretching mode of the hydroperoxo intermediate. Inspection of rR data of irradiated myoglobin in buffer pH 9.5 (Figure 2.24, panel II), reveals that the frequency of the ν(Fe-O) mode is not affected by increase in pH from 8.5 to 9.5. It is important to note that the frequencies of the ν(Fe-O) modes of the hydroperoxo intermediate in these higher pH (8.5 and 9.5) are only slightly higher than that observed for sample at pH 7.0 (620 vs 617 cm^{-1}, respectively), indicating only minor strengthening of the Fe-O bond at higher pH. The essential point is that the decrease in proton concentration in these high pH samples did not provide evidence for a peroxo- species.

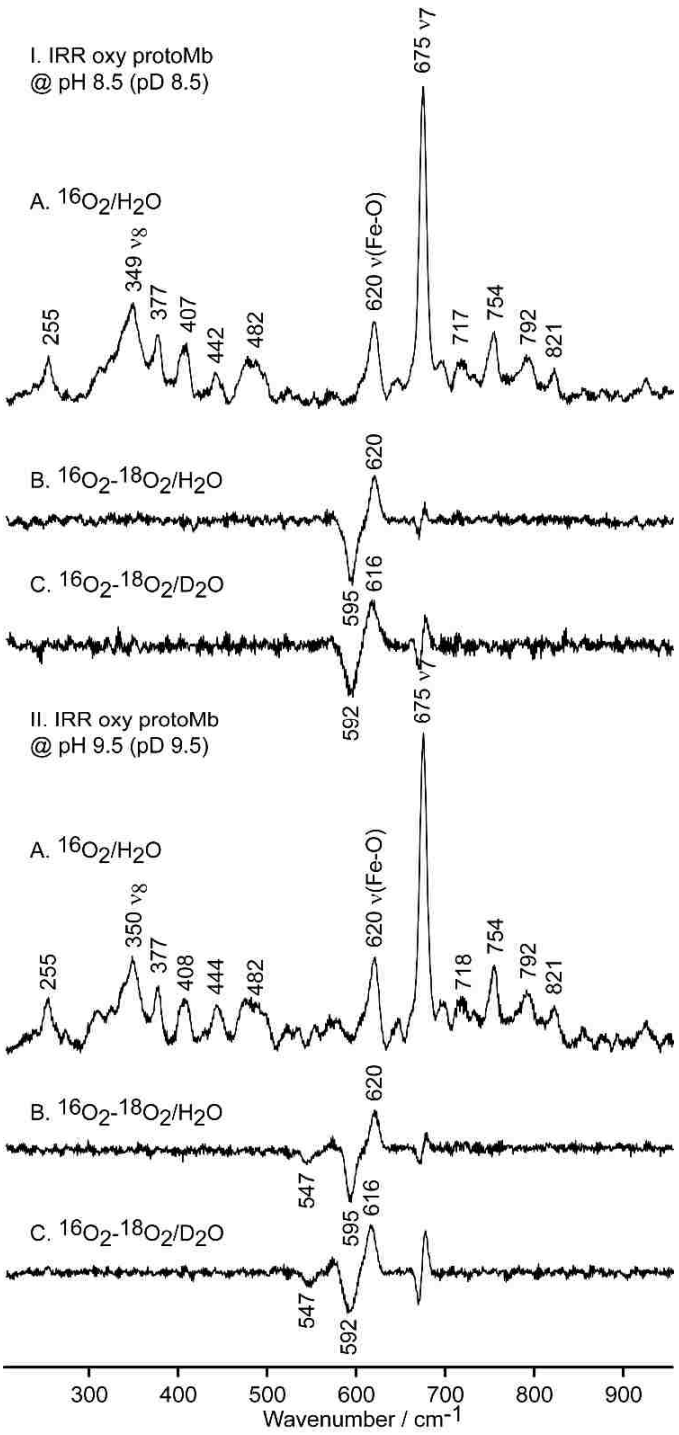

Figure 2.24. The low frequency rR spectra of irradiated oxy protoMb at different pH. Panel I - samples at pH 8.5 (pD 8.5), A) $^{16}O_2/H_2O$, B) the $^{16}O_2$-$^{18}O_2$ difference trace in H_2O buffer, C) the $^{16}O_2$-$^{18}O_2$ difference trace in D_2O buffer. Panel II – samples at pH 9.5 (pD 9.5), A) $^{16}O_2/H_2O$, B) the $^{16}O_2$-$^{18}O_2$ difference trace in H_2O buffer, C) the $^{16}O_2$-$^{18}O_2$ difference trace in D_2O buffer. Samples were measured at 77 K, total collection time for each spectrum was 1-2 hrs, excitation line was 413.1 nm, laser power was 1.0 mW

Of special interest is the fate of the trapped hydroperoxo- intermediate. The irradiated samples were annealed to higher temperatures and the rR spectra were measured. Figure 2.25 shows spectra of $^{16}O_2/H_2O$ sample annealed to 180 K and 200 K (traces A and C, respectively) and the corresponding $^{16}O_2$-$^{18}O_2$ difference traces in H_2O buffers (traces B and D). While the ν(Fe-O) mode of hydroperoxo- intermediate is still clearly seen at 180 K, its characteristic difference pattern is much weaker in the difference trace of samples annealed to 200 K (Figure 2.25, trace D). Importantly, in the latter, there is a new difference pattern emerging in the region of 750-800 cm^{-1}; e.g.; there is a weak positive feature at 803 cm^{-1} and a negative one at 766 cm^{-1}, indicating that the 803 cm^{-1} band shifts by 37 cm^{-1} in $^{18}O_2$ sample, a value close to a theoretically calculated 36 cm^{-1} shift of the Fe=O fragment of heme ferryl intermediate. These data indicate that at higher temperatures (200 K) the second protonation of the Fe-O-O^- fragment takes place leading to the O-O bond cleavage and formation of the ferryl heme intermediate. It is noted that the ν(Fe=O) stretching mode of myoglobin Compound II mode was previously observed at around 803-805 cm^{-1} in rR spectra of samples prepared using freeze-quench apparatus.[46] The acquired data clearly show that resonance Raman interrogation of cryoradiolytic produced intermediates, coupled with careful annealing procedures, is an excellent method to detect and structurally characterize successively encountered heme enzymatic intermediates, both paramagnetic and non-paramagnetic.

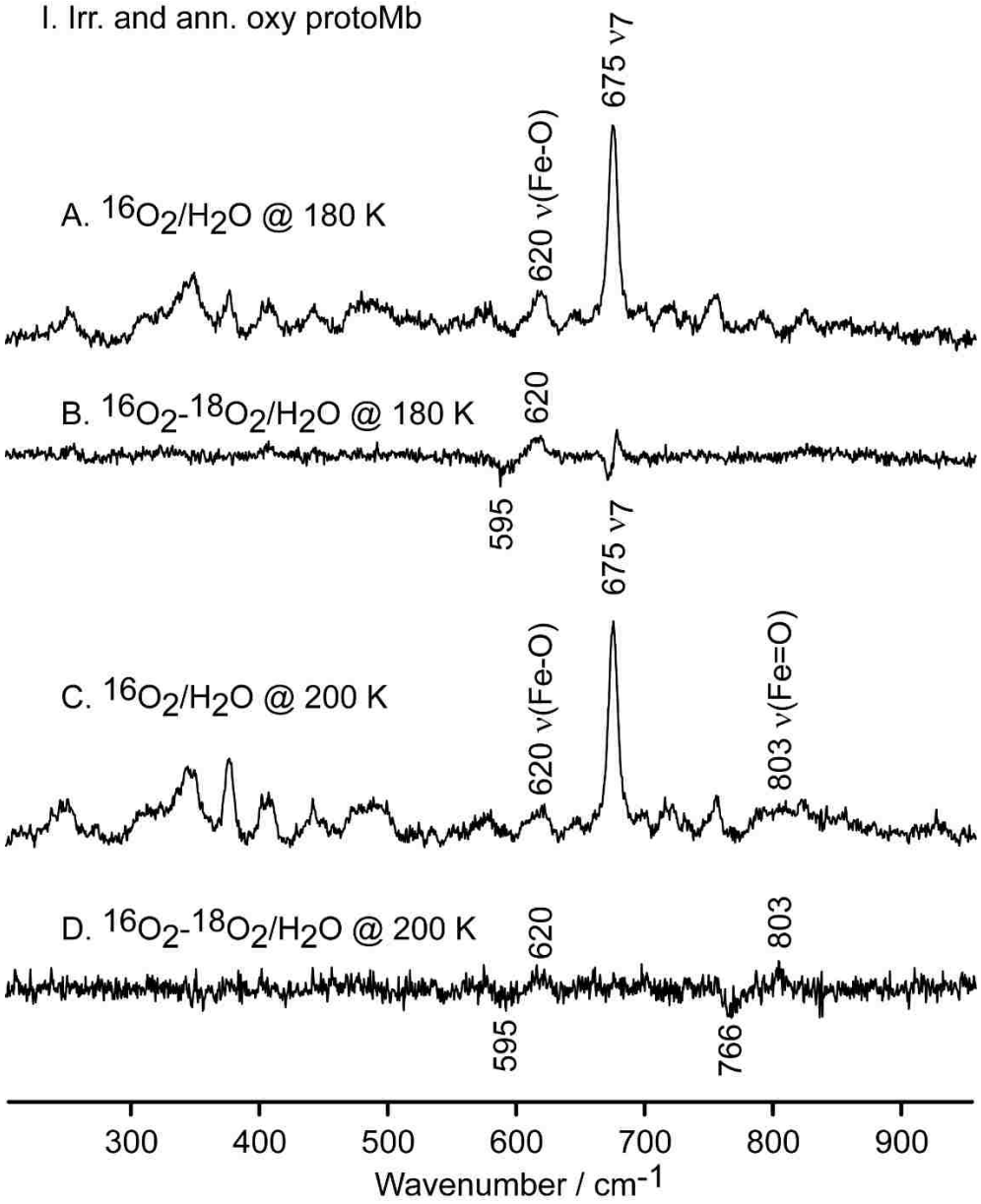

Figure 2.25. The low frequency rR spectra of irradiated and annelaed oxy protoMb at pH 8.5, A) $^{16}O_2/H_2O$ sample annealed to 180 K, B) the $^{16}O_2$-$^{18}O_2$ difference trace in H_2O buffer of samples annealed to 180 K, C) $^{16}O_2/H_2O$ sample annealed to 200 K, D) the $^{16}O_2$-$^{18}O_2$ difference trace in H_2O buffer of samples annealed to 200 K. Samples were measured at 77 K, total collection time for each spectrum was 2 hrs, excitation line was 413.1 nm, laser power was 1.0 mW.

2.4 Conclusion

Resonance Raman (rR) spectroscopy is generally useful to interrogate unstable intermediates that arise in the enzymatic cycles of heme enzymes, such as peroxo-, hydroperoxo- and ferryl species. While it is typically difficult to trap these elusive intermediates in solution, the cryoradiolysis approach offers a way to successfully overcome these obstacles. The present work employs modified derivatives of horse heart myoglobin to demonstrate the methodology and utility of a combination of resonance Raman and cryoradiolysis for detection and structural characterization of these reactive Fe-O-O, Fe-O-O-H and Fe=O fragments of such reactive species. First, the effect of active site mutations on the Fe-O-O fragments were investigated; specifically, the His64Leu, Val68Ser and Ile107Ala in the distal pocket and Ser92Ala, Ser92Leu and His97Phe on the proximal side. The current work has permitted documentation of the frequencies of the ν(Fe-O) stretching modes of the relatively unstable dioxygen adducts of these mutants, some of them previously unreported. Significantly, applying the cryoradiolysis approach has yielded previously unavailable vibrational spectroscopic data for the peroxo-, hydroperoxo and ferryl derivatives of these mutants. Of the six mutations investigated, only two, the H64L and V68S replacements had a significant effect on the structure and stability of these unstable intermediates.

Chapter 3 Resonance Raman Studies of Cytochrome P450 2B4 and its mutants

3.1 Introduction

3.1.1 The native protein

Cytochrome P450 2B4 (CYP2B4) is an example of important mammalian membrane-bound cytochrome P450 enzymes that catalyze the metabolism of pharmaceuticals and other xenobiotics [2, 118-120]. As was discussed in Chapter 1, these drug-metabolizing P450s have large and flexible distal pockets so that they can bind many different substrates. This is necessary, because this processing is efficient only if a few of these types of enzymes are necessary. For example, the human enzymes CYP3A4 and CYP2D6 metabolize over half of the drugs that are now being used. The enzyme used in our work was supplied by our collaborator, Professor Lucy Waskell of the University of Michigan. This particular enzyme was one of the first such membrane-bound, xenobiotic metabolizing P450s discovered. [118-120] CYP2B4 was extracted from rabbit hepatic microsomes, but of course now is expressed in bacteria. These kinds of cytochromes P450 in the mammalian liver microsomes can oxidize fat-soluble compounds to water-soluble compounds that can then be excreted [118-120]. The general mechanism for this type of conversion was discussed in some details in Section 1.1.3.

As we know, resonance Raman spectroscopy (rR) is a powerful tool for investigating the heme environment and it can provide information about heme co-ordination, spin and oxidation states and some resonance Raman studies of full length wild type ferric CYP2B4 have been already done in our lab in the past. The first paper dealt with characterizing the WT substrate-free form and those bound with either benzphetamine

(BZ) or butylated hydroxytoluene (BHT) [121]. Figure 3.1.1 shows the rR spectra obtained for the ferric substrate-free and substrate-bound forms. The oxidation state marker ν_4 band appears at 1372cm^{-1} consistent with the ferric form and the frequency doesn't change much as the temperature changes or when CYP2B4 binds different substrates. The ν_3, ν_2 and ν_{10} modes are the "spin state markers". If the CYP2B4 is in 5-coordinated high spin state (5CHS), the ν_3, ν_2 and ν_{10} modes are 1487, 1567 and 1625 cm^{-1}, respectively. If the CYP2B4 is in 6-coordinated low spin state (6CLS), the ν_3, ν_2 and ν_{10} modes are 1502, 1583 and 1640 cm^{-1}, respectively. The rR spectra show that in the substrate free (SF) CYP2B4 spectrum at 4^{o} C, the 5CHS and 6CLS existed in equilibrium (Figure 3.1.1 A).

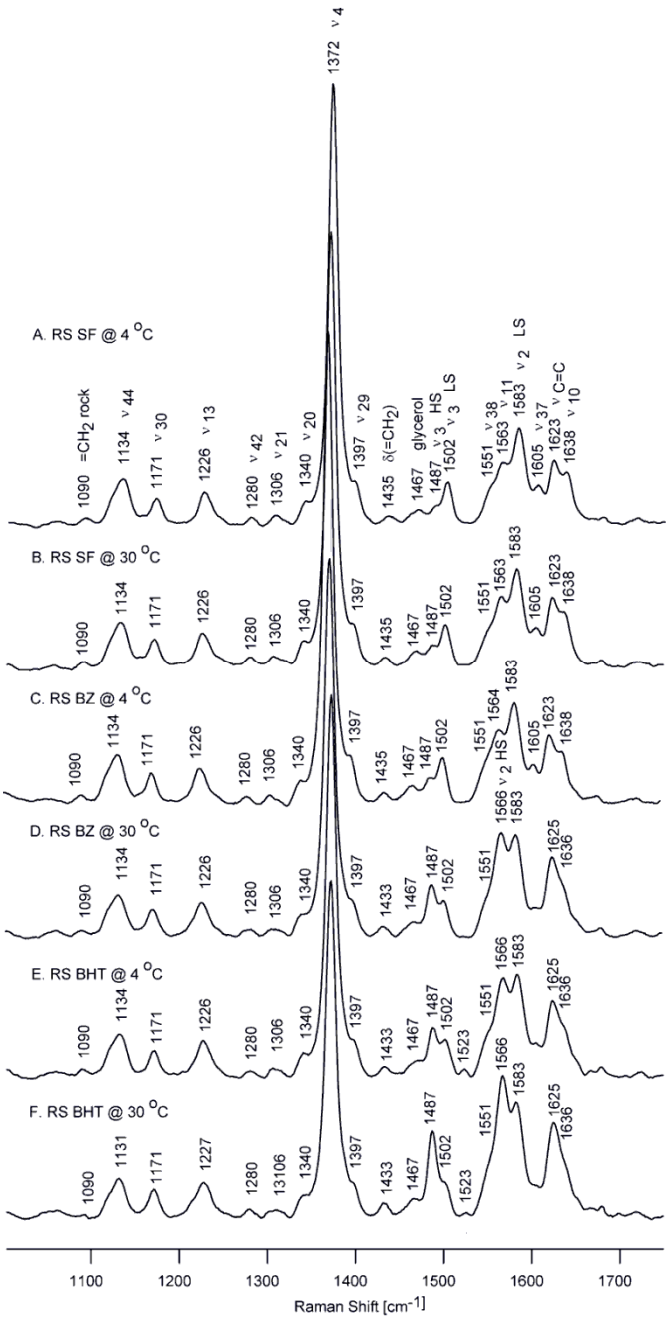

Figure 3.1.1 High-frequency resonance Raman spectra of wild-type resting state (RS) ferric P450 2B4 without substrate (substrate –free, SF) (spectra A and B) and with substrates: spectra C and D with benzphetamine (BZ); spectra E and F with butylated hydroxytoluene (BHT) at 4 and 30 °C. [121]

Usually, when studying soluble P450s, such as bacterial ones, the SF form is almost pure LS and then converts to almost pure HS when substrate is added. In a lot of the rR studies on membrane bound mammalian cytochrome P450s it is sometimes seen that

there are these mixtures of spin states, even for SF form. This is probably due to the tendency of these kind of membrane proteins to aggregate in solution, even though different kinds of substances are added to solubilize them. For example, studies of CYP3A4 done in our lab by Dr. Mak showed this problem, but it was able to be avoided by using nanodisc technology in which each CYP3A4 molecule is associated with a small "patch" of artificial membrane that is about 10nm diameter. [122]

Another reason that mixtures of spin states can occur is that substrate binding can be hindered. In some cases it is possible to improve substrate binding by increasing temperature slightly. As can be seen in Figure 3.1.1, when the temperature is increased to 30^{o} C, the spin state does not change in the case of the SF form (Figure 3.1.1 B). However, in the cases where substrate (BZ or BHT) is present, the high-spin component becomes greater at higher temperature (~30^{o} C) (Figure 3.1.1, C-F). This increase in spin state with temperature shows that the increased temperature facilitates substrate binding.

Another factor that can influence CYP2B4 function is the nature of the redox partner. [118] The primary reductase for most mammalian cytochromes P450, including CYP2B4, is cytochrome P450 reductase (here called CPR). However, the function of CYP2B4 is also influenced by cytochrome b5 (cytb$_5$). [118] As is shown in Figure 3.1.2, both of these bind on the proximal side of CYP2B4, near the heme site. Since there are functional differences between the two enzyme/redox partner pairs, there is a lot of interest in determining if the two redox partners influence active site structure of CYP2B4 differently or not. As will be shown, resonance Raman spectroscopy can be useful in this case, including recently completed studies in our lab of the effects of cytb$_5$ on the

dioxygen adduct (vide infra). Previous studies in our lab had already shown that binding of these two redox partners can have different effects on details of active site structure.

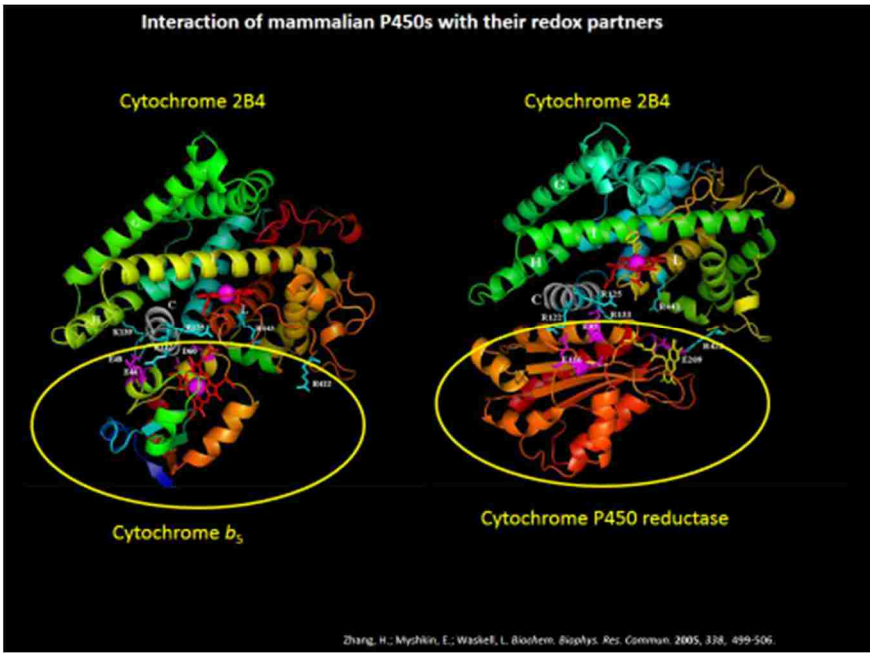

Figure 3.1.2. The binding of cytochrome b5 and CPR to CYP2B4 [123]

Considering the rR spectra shown in Figure 3.1.3, below, the presence of redox partners Mncyt b_5 and CPR does not appear to have a substantial effect on heme structure, comparing to spectra in Figure 3.1.1. However, a more careful inspection reveals actual differences in the effects of the two redox partners. This can be seen in the expanded plots shown in Figure 3.1.4, where the fraction of HS component increases slightly in the presence of cytb5, while in the presence of CPR the effects are smaller or perhaps even reversed; i.e., especially in the case of the BZ-bound form, CPR appears to *decease* the percentage of HS form.

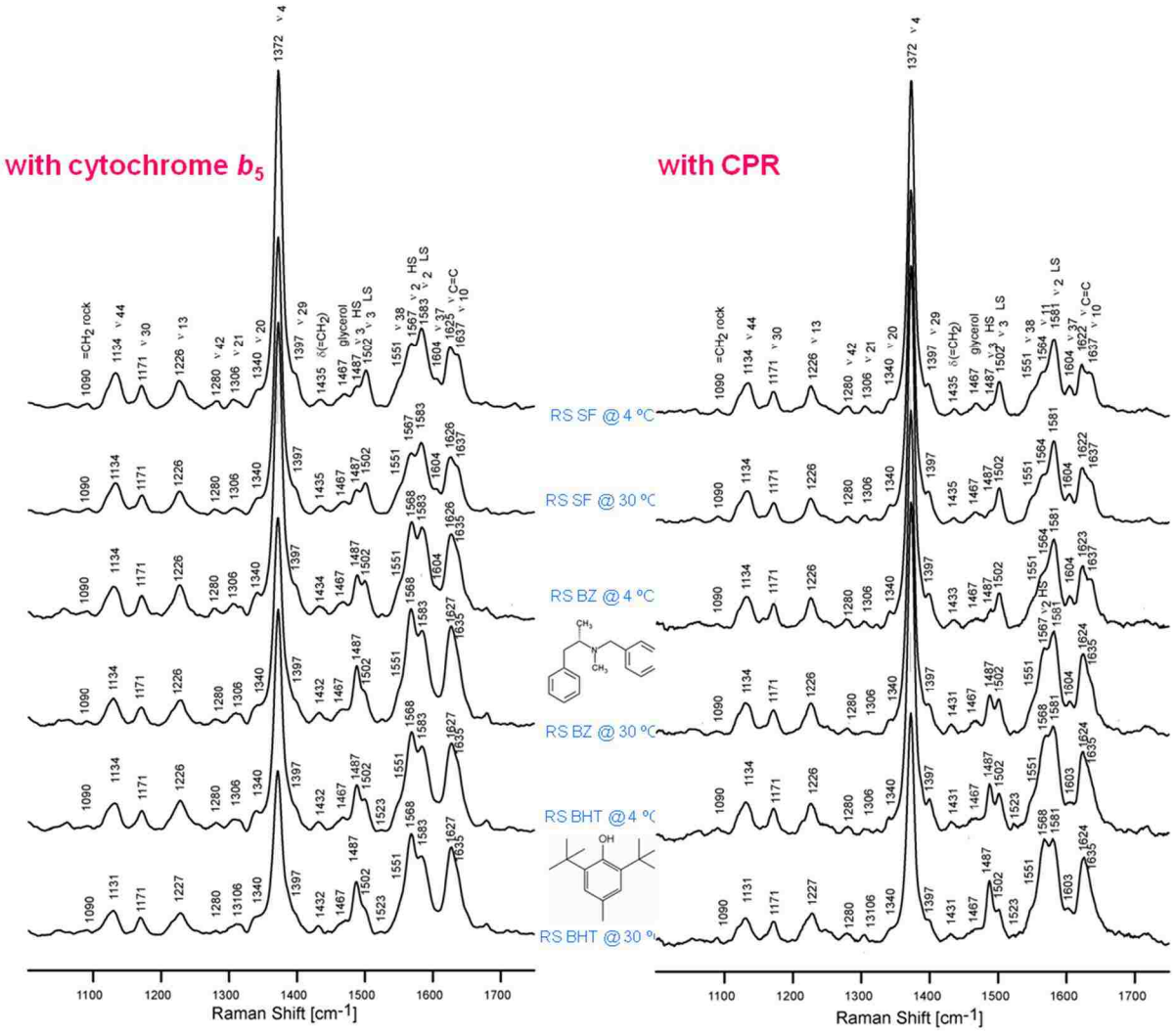

Figure 3.1.3 shows the high-frequency resonance Raman spectra of substrate free and substrate-bound forms of P450 2B4 interacting with Mn (III) cytochrome b5 (Mn cyt b_5) and rat P450 reductase (CPR), respectively. Mn (III) proteins have been used to avoid the interference from the RR lines of the native proteins (cyt b_5 is iron-containing protein). [121]

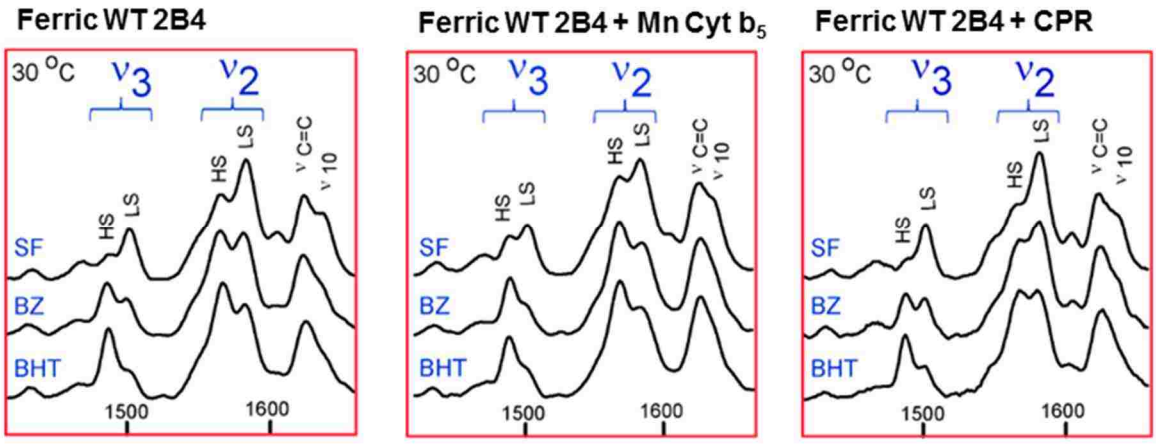

Figure 3.1.4 shows the expanded view of spin state marker region, extracted from Figures 3.1.1 and 3.1.3.

In addition to these spin state effects, changes are noted in the low frequency region. The low frequency spectra for CYP2B4, using near UV excitation, are shown in Figure 3.1.5, below; it is only with this excitation line that the ν(Fe-S) mode can be enhanced and then only for the HS ferric forms. [53] The weak band appearing near 350 cm^{-1} for the SF sample with no redox partner present (trace C) is a heme mode (ν_8). The data show that the ν(Fe-S) is enhanced only for the substrate-bound (HS) forms; although binding of substrates can activate the ν(Fe-S) mode, without any redox partner present, the ν(Fe-S) modes have the same frequency (354cm^{-1}) for the two different substrates, BHT and BZ. Since the substrates are in the distal pocket, there is little effect on the status of the Fe-S bond, which is on the proximal side. Each of the redox partners, the natural CPR and cytb_5, bind to the proximal side of CYP2B4 and might be expected to have some effect. As seen in Figure 3.1.5, binding of Mn cyt b_5 causes the ν(Fe-S) mode to downshift to 352cm^{-1} (traces D and E), but after adding CPR, the ν(Fe-S) modes don't change

significantly (traces G and H). The decrease in the ν(Fe-S) stretch is consistent with an increase in the HS population. Since both two redox partners are negatively charged, the electrostatic arguments cannot be used to explain why the ν(Fe-S) downshift in CYP2B4 with Mn cytb$_5$ but stays the same in CYP2B4 with CPR. The most reasonable explanation is that Mn cytb$_5$ induces some degree of structural change in the CYP2B4 active site that affects the Fe-S linkage [124].

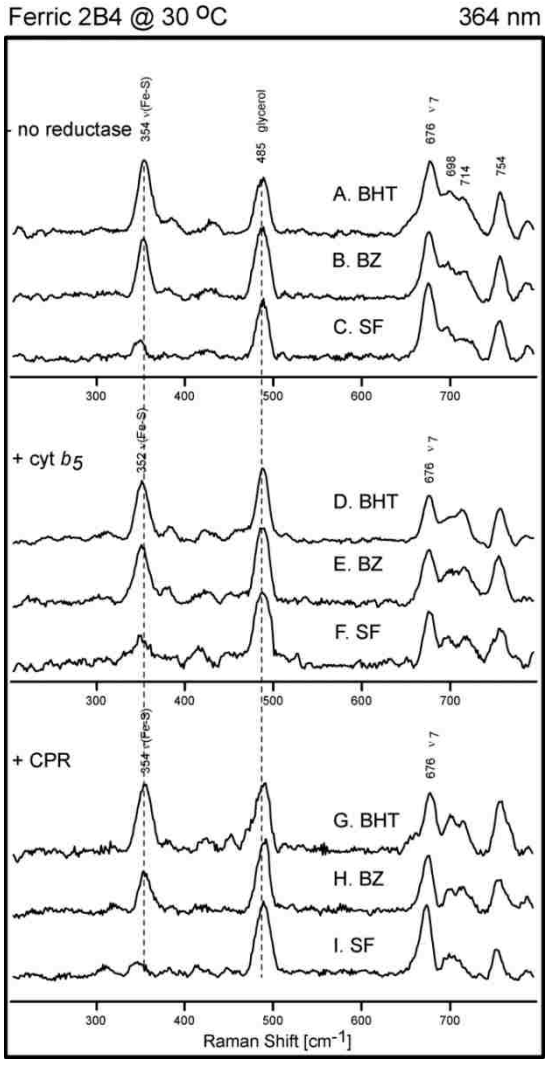

Figure 3.1.5: The low-frequency rR spectra of ferric BHT and BZ bound as well as substrate-free 2B4 without redox partner, with Mn cyt b_5, and with P450 reductase present. Excitation line 364 nm, total collection time for each spectra 30 min [121].

3.1.2 Mutants of CYP2B4

To get insight into the mechanisms of CYP2B4 function, our collaborators prepared two interesting mutants (Figure 3.1.6). The E301Q variant is comparable to the D251N mutant of CYP101 that was discussed in Chapter 1; that mutation affects the proton delivery shuttle, to stabilize the peroxo- intermediate of the enzymatic cycle. This will be very useful for planned future studies of the cryoreduced dioxygen adducts of CYP2B4. The other mutant prepared is on the proximal side, where an H-bond donor residue (histidine) is introduced in a position to permit interaction with the Fe-S linkage. So, the F429H replacement is expected to decrease the autoxidation rate because the proximal push effect would be decreased. [84, 85].

Actually, recent studies by Dr. Mak provide convincing evidence that this new H-bond interaction definitely impacts this linkage. [54]Thus, as shown in Figure 3.1.7, the presence of this new H-bond causes a significant weakening of the Fe-S linkage, as shown by a 6 cm^{-1} shift of the ν(Fe-S) mode.

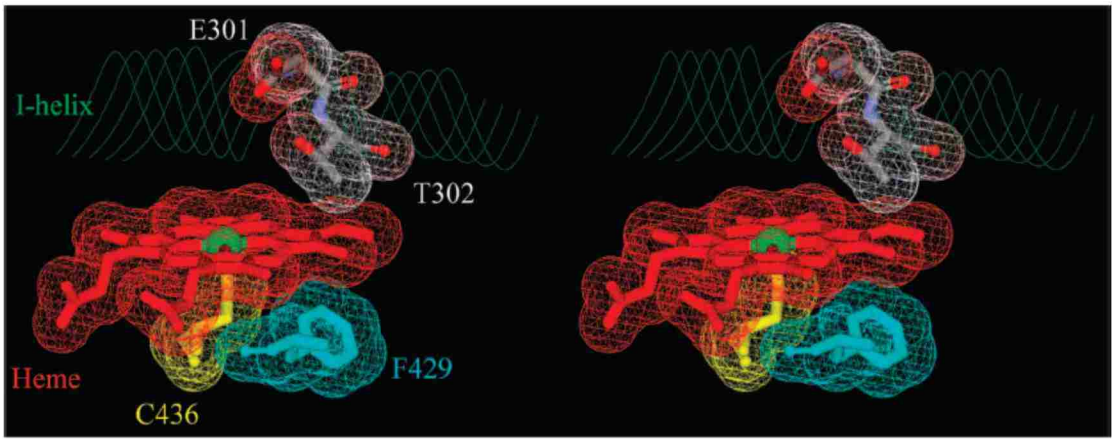

Figure 3.1.6 Stereo view of CYP2B4 active site showing the heme and positions of mutated residues (pdb: 1SUO). Iron is the green ball in the center of heme; the negatively charged surfaces of E301 and T302 are shown in red, positively charged surfaces are in blue, and neutral surfaces are in white. The figure was generated with DS viewer Pro [125].

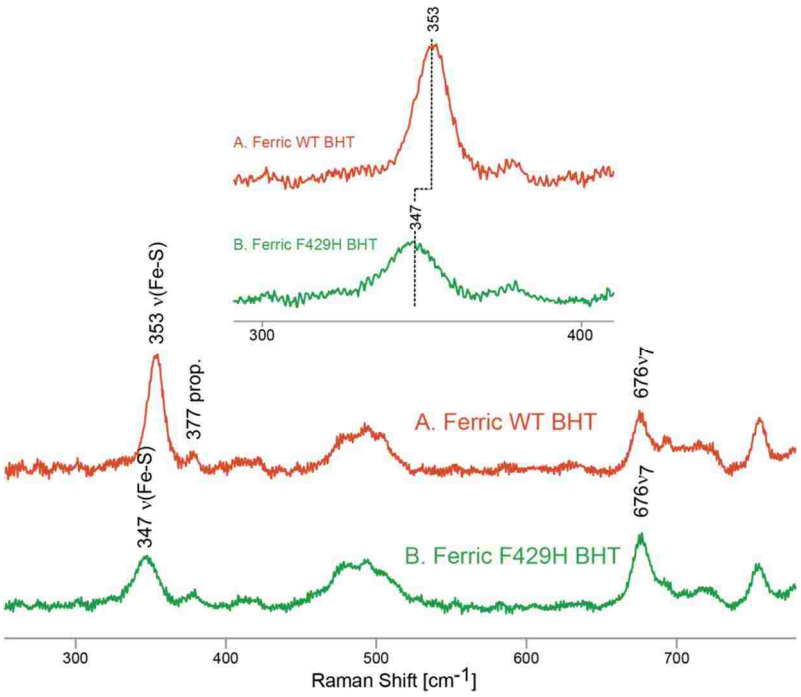

Figure 3.1.7 The low frequency rR spectra of ferric CYP2B4 and its F429H variant with 356.4 nm excitation showing a shift of the ν(Fe-S) stretching mode.[54]

3.1.3 Specific Plans

The original plan for this part of my dissertation was to prepare the dioxygen adducts of CYP2B4 and its mutants and characterize them with rR spectroscopy and then to use these samples for rR studies of the intermediates in the P450 enzymatic cycle by employing the cryoradiolysis methods describe in Chapter 2. However, the fact that dioxygen adducts of these membrane-bound, drug metabolizing P450s are so unstable, autoxidizing so quickly, has resulted in spending a very long time to prepare and trap these dioxy-precursors. In fact, the only report we are aware of is that the oxy complex of WT CYP2B4, but not mutants, was trapped by using solutions that have a very high concentration of glycerol (70% by weight) that allowed mixing at very low temperatures (-50 C).[126,127]. As will be seen, after a long time developing our techniques, we have succeeded in trapping the dioxygen adduct of WT CYP2B4 using only 30% glycerol at a temperature of -25C. Furthermore, we have also succeeded in generating and trapping the dioxygen adduct of the E301Q mutant of CYP2B4. We have been able to successfully acquire good quality rR spectra of these. Of special importance is that, very recently, we have been able to acquire high quality rR spectra of the dioxygen adduct of WT CYP2B4 in complex with a variant of the $cytb_5$ redox partner; i.e., apo-$cytb_5$.

3.2 Materials and methods

The wild-type CYP2B4 and its mutants E301Q and F429H were kindly provided by the Dr. Waskell's group. Sodium dithionite, boric salt and glycerol were obtained from Sigma Aldrich.

3.2.1 Oxygen-complex Samples preparation

3.2.1.1 Oxy-complex of WT-CYP2B4 samples provided by Dr. Waskell's group

The first series of samples are sent by Sang-Choul Im (University of Michigan), from Dr. Waskell's lab in University of Michgan and VA Medical Center.

List of the samples:

Sample 1 &2. WT P450 2B4-16O2 + BHT in H2O buffer (BHT+16H), 100μL;

Sample 3 &4. WT P450 2B4-18O2 + BHT in H2O buffer (BHT+18H), 100μL;

Sample 5 &6. WT P450 2B4-16O2 + BHT in D2O buffer (BHT+16D), 100μL;

Sample 7 &8. WT P450 2B4-18O2 + BHT in D2O buffer (BHT+18D), 100μL;

Sample 9 &10. WT P450 2B4-16O2 + BZ in H2O buffer (BZ+16H), 100μL;

Sample 11 &12. WT P450 2B4-18O2 + BZ in H2O buffer (BZ+18H), 100μL;

Sample 13 &14. WT P450 2B4-16O2 + BZ in D2O buffer (BZ+16D), 100μL;

Sample 15 &16. WT P450 2B4-18O2 + BZ in D2O buffer (BZ+18D), 100μL.

CYP2B4 proteins are dissolved in 50mM boric buffer (pH 8.2) with 60% glycerol, 0.3M NaCl and substrates. The concentration of substrates to CYP2B4 is 1:5. The concentration of protein in each solution is 150μM. The oxy-CYP 2B4 was prepared by bubbling O_2 gas at -60°C. All the samples were stored and measured in liquid nitrogen. The rR spectra acquired for both the BZ and BHT bound samples (Figures 3.3.1.1.1 through 3.3.1.1.4, vide infra) showed no evidence for a dioxygen adduct.

3.2.1.2 The WT-CYP2B4 samples and mutants prepared by new vacuum system

Since the rR measurements of supposedly oxy complexes prepared by our collaborators failed we decided that we could try to prepare the oxy complexes in our laboratory. As described in Chapter 2, part 2.2.2, a new vacuum system was developed to prepare these oxy samples of CYP2B4 by addition of oxygenated buffer to the reduced protein.

The ferric CYP2B4 samples, supplied to us by our collaborators, were in very limited quantities. Therefore a more convenient protein, myoglobin, was chosen to practice preparation of oxy-form. As will be explained later, there are some differences in preparation of oxy-Mb comparing to preparation of oxy-CYP2B4, e.g., myoglobin oxygen adduct is much stable than oxyCYP2B4.

The protein samples in the NMR tubes (WG-5M-ECONOMY-7, Wilmad Glass Co., Beuna, NJ) were connected to a vacuum line system and were degassed twice at first. The ferrous protein was obtained by titration with sodium dithionite solution under an argon atmosphere. The formation of the ferrous protein was confirmed by UV-vis. The O_2 saturated buffer or gas was added to the ferrous CYP2B4 solution at low temperature and mixed completely. The operation temperature of Mb and CYP2B4 are ~0 ºC and ~- 26 ºC, respectively. The formation of oxy-CYP2B4 were confirmed by rR spectroscopy.

The key of the experiment was to separate the air from the cooled sample during addition of oxygen into protein sample. In our new design, argon flow is been used to make sure each sample is anaerobic. At the beginning, all the valves were closed. The procedure of degassing was 3 steps. The first step was turn on valve 1 for a few second

then turned off. The system was on evacuated. The second step was to turn on valve 3 for a few seconds. Since the valve 3 connected to NMR tubes, protein solution was degassed. The third step was open valve 2 to let argon air to saturate the solution. This process repeat several times until all the oxygen was gone. For 50-100μL protein sample, this process is repeated 2-3 times to make sure it is completely degassed.

3.2.2 Resonance Raman measurement

Resonance Raman spectra were obtained using a Spex 1269 spectrometer equipped with a CCD detector (Spec 10 from Princeton Instruments), at liquid N_2 temperatures (77 K). The excitation lines employed for the oxyferous samples before and after irradiation was 413 nm or 415nm**.** Fenchone was used to calibrate all spectra, which were processed with Grams 32/AI (Galactic Industries, Salem, NH). Rayleigh scattering was removed by use of an appropriate Notch filter from Kaiser Optical. The power at the sample was approximately 1.0 mW. The NMR tube containing the sample was spun and the rR spectra were collected at liquid N_2 temperature using 180° (back scattering) geometry in combination with a cylindrical lens, which focuses the laser beam on the sample as a line image to avoid local heating (Figure 2.3). The width of slit was 150μm. Total collection time for each spectrum was 2 hrs in high frequency region and 4 hrs in low frequency region.

3.3 Results and discussion

3.3.1 The samples from Dr. Waskell's group

3.3.1.1 High frequency rR of P450 2B4+dioxygen+ BHT or BZ (oxy-samples from Dr. Waskell's group)

The Figure 3.3.1 and 3.3.2 show the rR spectra of oxy-CYP2B4 with BHT in high frequency region. The band at ~1376cm^{-1} is assigned ν_4. The band at ~1261cm^{-1} is an emission line form the fluorescent lights in the lab. The ν_3 mode (expected at ~1500 cm^{-1}), ν_2 mode (expected at ~1580 cm^{-1}) and ν_{10} mode (expected at ~1630 cm^{-1}) are not obvious in Figure 3.3.1. The band around 1130cm^{-1} might have been assigned as the heme mode or stretching mode of O-O [138, 143]. However, the isotope difference trace Figure 3.3.2, shows there was no clear evidence for a stretching mode of O-O in the area ~1100cm^{-1}.

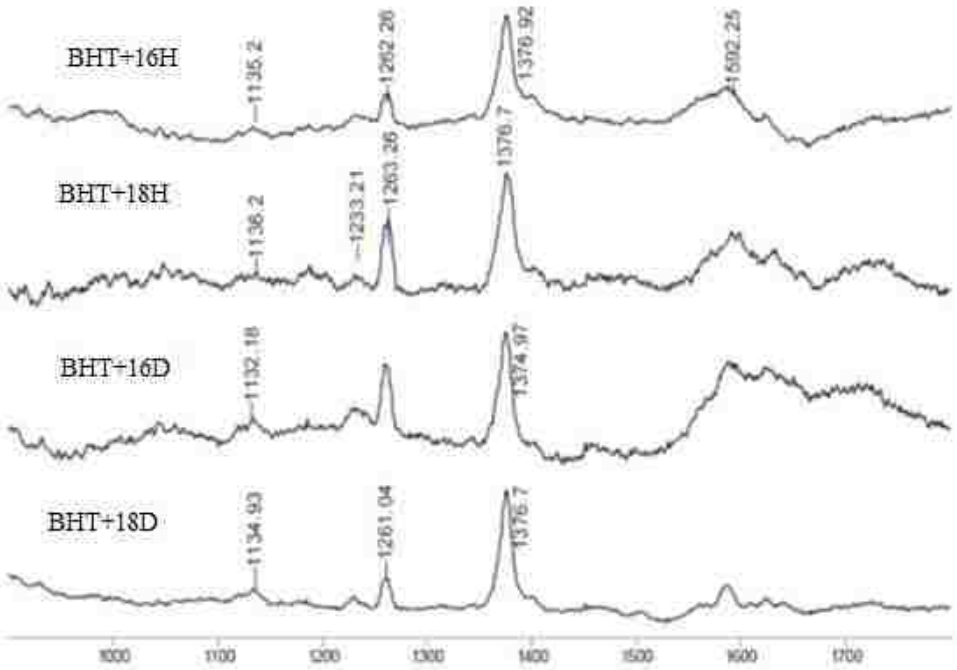

Figure 3.3.1 High frequency spectra of oxy P450 2B4 containing BHT in boric buffer, the $^{16}O_2/H_2O$ (S1), $^{18}O_2/H_2O$ (S3), $^{16}O_2/D_2O$ (S5) and $^{18}O_2/D_2O$ (S7). Note: Si indicated sample number.

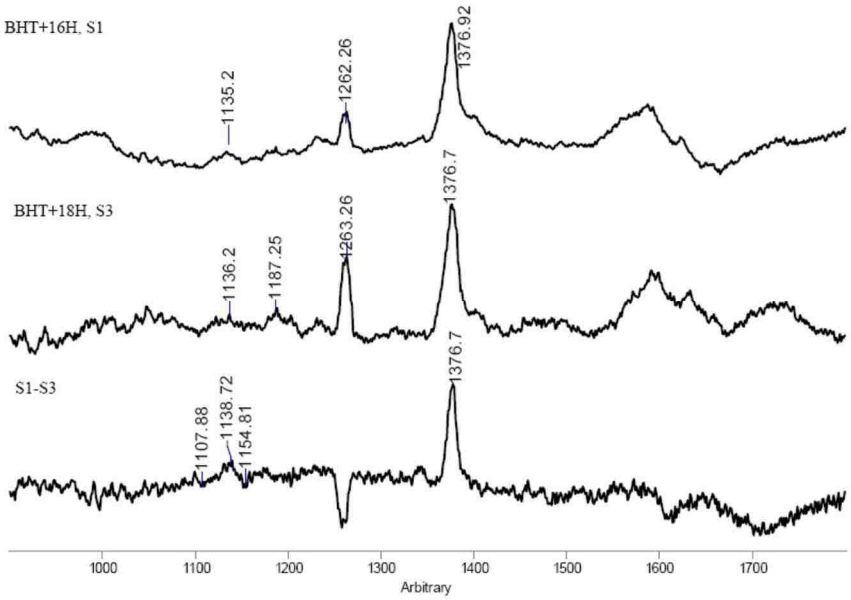

Figure 3.3.2 High frequency spectra of oxy P450 2B4 containing BHT in boric buffer, the $^{16}O_2/H_2O$ (S1), $^{18}O_2/H_2O$ (S3) and difference trace (S1-S3)

The Figure 3.3.3 was the high frequency rR spectra of Sample 9, Sample 11, Sample13 and Sample 16 of series 1. They were the P450 2B4+dioxygen +BZ in boric buffer. The spectra of these samples were similar to the spectra of P450 2B4+dioxygen+BHT sample. The bands at ~1130cm^{-1} was also very small. As a result, the qualities of the spectra of protein with different substrate were different. In the isotope difference traces of these samples, as shown in Figure 3.3.4, there was no evidence to show the stretching modes of oxygen-oxygen at ~1130cm^{-1}. The ratio of intensity of ν_4 to ~1135cm^{-1} is 1/6 or 1/7 in Figure 3.3.3 and Figure 3.3.4. But in the difference trace, there is no expected difference pattern with bands near 1135 and 1070 cm^{-1}. So, there is no evidence for the stretching mode of O-O band.

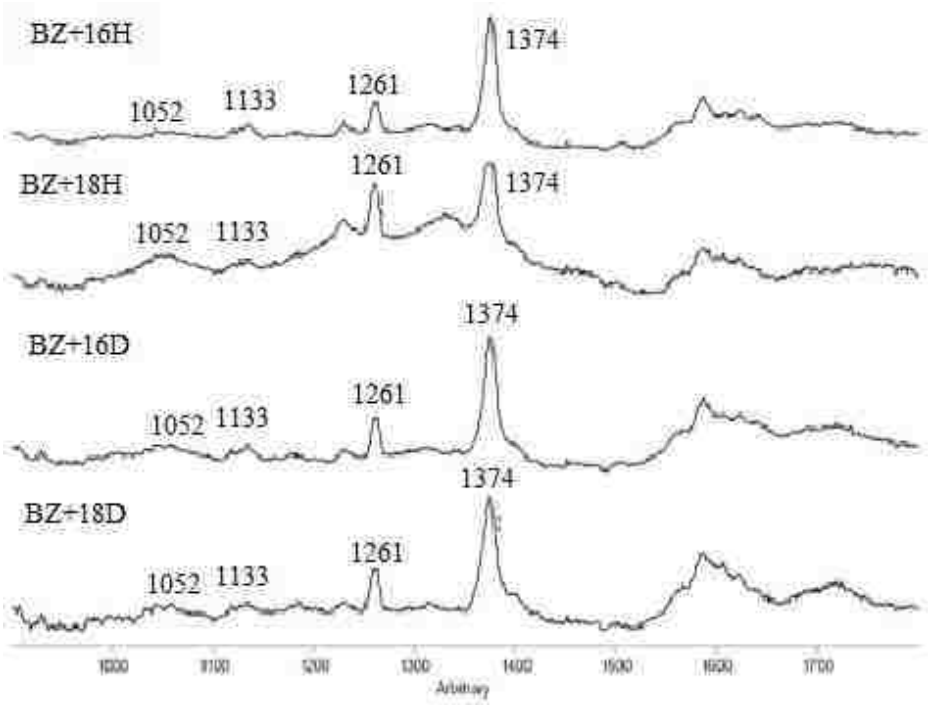

Figure 3.3.3 High frequency spectra of oxy P450 2B4 containing BZ in boric buffer, the $^{16}O_2/H_2O$ (S9), $^{18}O_2/H_2O$ (S11), $^{16}O_2/D_2O$ (S13) and $^{18}O_2/D_2O$ (S16).

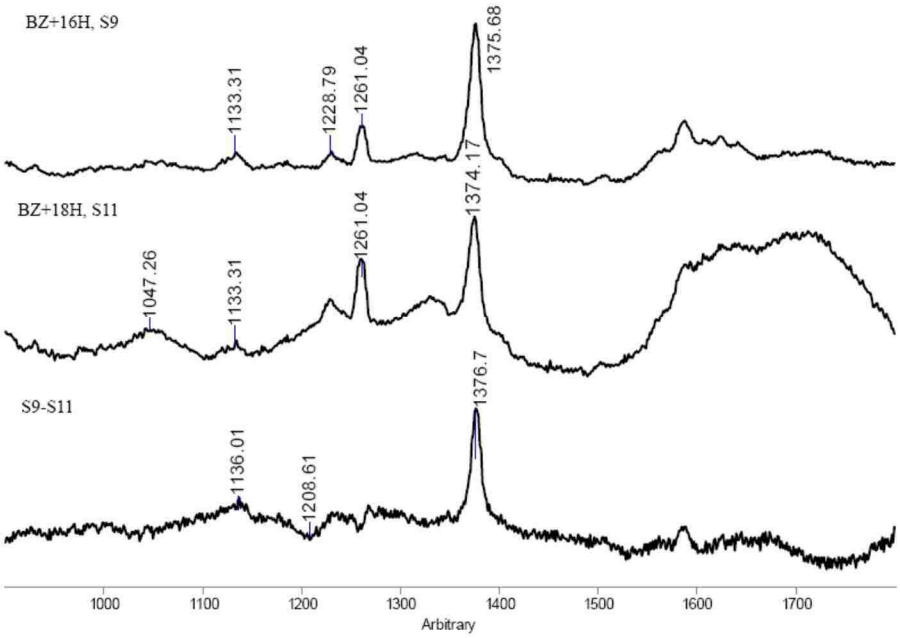

Figure 3.3.4 The high frequency spectra of oxy P450 2B4 containing BZ in boric buffer , the $^{16}O_2/H_2O$ (S9), $^{18}O_2/H_2O$ (S11) and difference trace.

3.3.1.2 Conclusion (oxy-samples from Dr. Waskell's group)

The samples of oxy- P450 2B4 with two substrates, BHT and BZ, were made in Prof. Waskell lab. Resonance Raman spectroscopy was employed to measure these samples. Spectra of these samples show there were no evidence for ν(O-O) stretching modes.

The possible reasons why there was no oxy-form in these samples are as follow:

a. Photolysis

The laser may photo-dissociate the protein samples. However, when the P450 2B4 samples were measured, the laser power was always below 1.0 mW, the power that is usually employed for measurements of cytochromes oxy complexes at cryogenic temperatures. Thus it is rather unlikely to conclude that the protein samples were photo-dissociated due to the laser power.

In order to double check whether the samples are photo-dissociated or not after several hours' measurements, some experiments have been done. Assuming that the surface of the sample might be photo dissociated or warmed up, we tried to mix the sample so that the fresh and hopefully oxy content in the center of bulk sample could be transferred to the surface of the NMR tube. In order to do so, the samples were warmed up to approximately – 55 °C, at which temperature the sample become soft while potential oxy is complex still stable. The samples were mixed using the thermocouple. Then, samples were frozen in liquid nitrogen again and RR spectra were measured. The RR spectra were the same as before, i.e., the spectra show no oxygen sensitive modes.

b. Defreeze

The other possibility which could make these samples autooxidize is their accidental thawing. However, as far as I know, the samples were never thawed.

c. Something happened during transport

It is possible, that the protein samples were warmed up during transportation. However, when we received the samples, the tank was sealed and there is some liquid nitrogen left in the bottom of the tank. So the transport was appropriate.

d. Something went wrong before the samples are sent

The samples might have been autooxidized before they are frozen.

3.3.2 Optimization of preparation oxy-CYP2B4

3.3.2.1 Test of the vacuum system below -20°C

Mb solution was employed to test the air tightness of new system. If the system was air-tight, the ferrous Mb wouldn't change even if the degassed buffer or argon added. In order to test the gas-tightness of the new vacuum system, one procedure was been made: degas the met-Mb solution, reduce and add degassed buffer. In each step, the Mb was checked by the UV-Vis spectra. For 50μL met-Mb sample, was degassed 3-4 times before it was reduced. Then 10mM $Na_2S_2O_4$ solution (~80%) was added to reduce ferric Mb or CYP 2B4 to ferrous form.

In the UV-Vis spectra, the bands at 505 nm and 635 nm were the "Q-band" of met-Mb. The bands at 543 nm and 581 nm are the "Q-band" of oxy-Mb. The band at 556 nm is the "Q-band" of deoxy-Mb. When sodium dithionite was added in 10% excess, the met-Mb was completely reduced. The UV spectra are shown in Figure 3.3.5b. As shown in Figure 3.3.5c, the deoxy-Mb was still present and no oxy-Mb is in the solution after adding degassed buffer. The UV-Vis spectra were checked every half min after the degassed buffer was added. Even after 2 min later, the oxy-Mb wasn't formed. Thus, it was concluded that the new vacuum system was sufficiently air-tight.

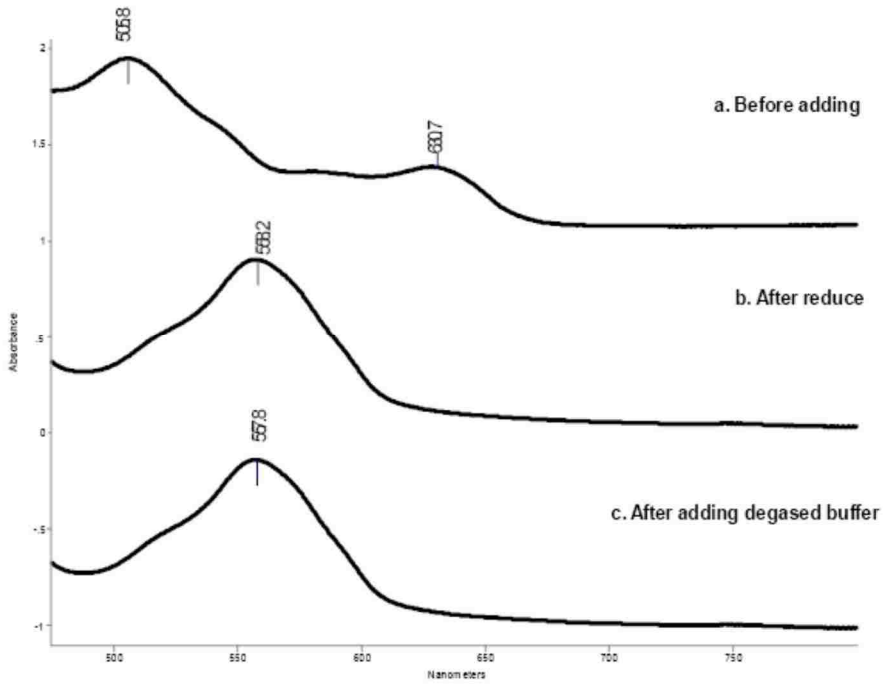

Figure 3.3.5 The UV-Vis spectra of Mb samples

3.3.2.2 Optimization of mixing time

After the air-tightness of the vacuum system was confirmed, we tried to optimize the mixing time of samples. Theoretically, the longer the mixing time, the better it is for preparation of oxy-protein because it allows better mixing. However, longer mixing time means also increased risk of protein auto-oxidation.

After the protein solution was degassed and reduced completely, the 50μL oxygen saturated buffer solution was added the ferrous Mb solutions and mixed them by a vortex. The mixing time of Mb was tested at 0s, 5sec, 10sec and 15sec. After mixing, these NMR tubes were cooled in liquid nitrogen and ready to be measured by rR spectroscopy. Not surprisingly, 15second was the best mixing time for deoxy-Mb and oxygen saturated

buffer because the amount of ferrous form was the smallest of all tested samples. However, similar tests were needed for CYP2B4, where autoxidation effects are important.

For CYP2B4, the best mixing time might need to be quite short in order to avoid the fast auto-oxidation of oxy-CYP2B4, which wouldn't happen with myoglobin, whose oxy form is quite stable. Based on the result of Mb, three different mixing times have been chosen for mixing time optimization, 3sec, 5sec and 10sec. The rR spectra of these CYP 2B4 samples are shown in Figure 3.3.6. The ν_4 mode of ferric and ferrous oxy-CYP 2B4 is at 1373cm^{-1}and at 1340cm^{-1} for ferrous form of CYP 2B4. The band around 1130cm^{-1} assigned as ν(O-O). The rR spectra of ferrous oxy-CYP 2B4 have 1373cm^{-1}and 1130cm^{-1} band. All the test samples of CYP 2B4 contained at least two forms: ferrous CYP 2B4 and oxy-CYP 2B4. The mixing time could not be too long although longer mixing time allows better mixing with oxygen and ferrous CYP 2B4. The RR spectra of samples prepared at three different mixing times **(**3sec, 5sec and 10sec) showed the same results, which has no ferrous component in the sample. Thus, considering issues of reproducibility in mixing times, 10sec was decided as optimal mixing time for CYP 2B4

and oxygen saturated buffer.

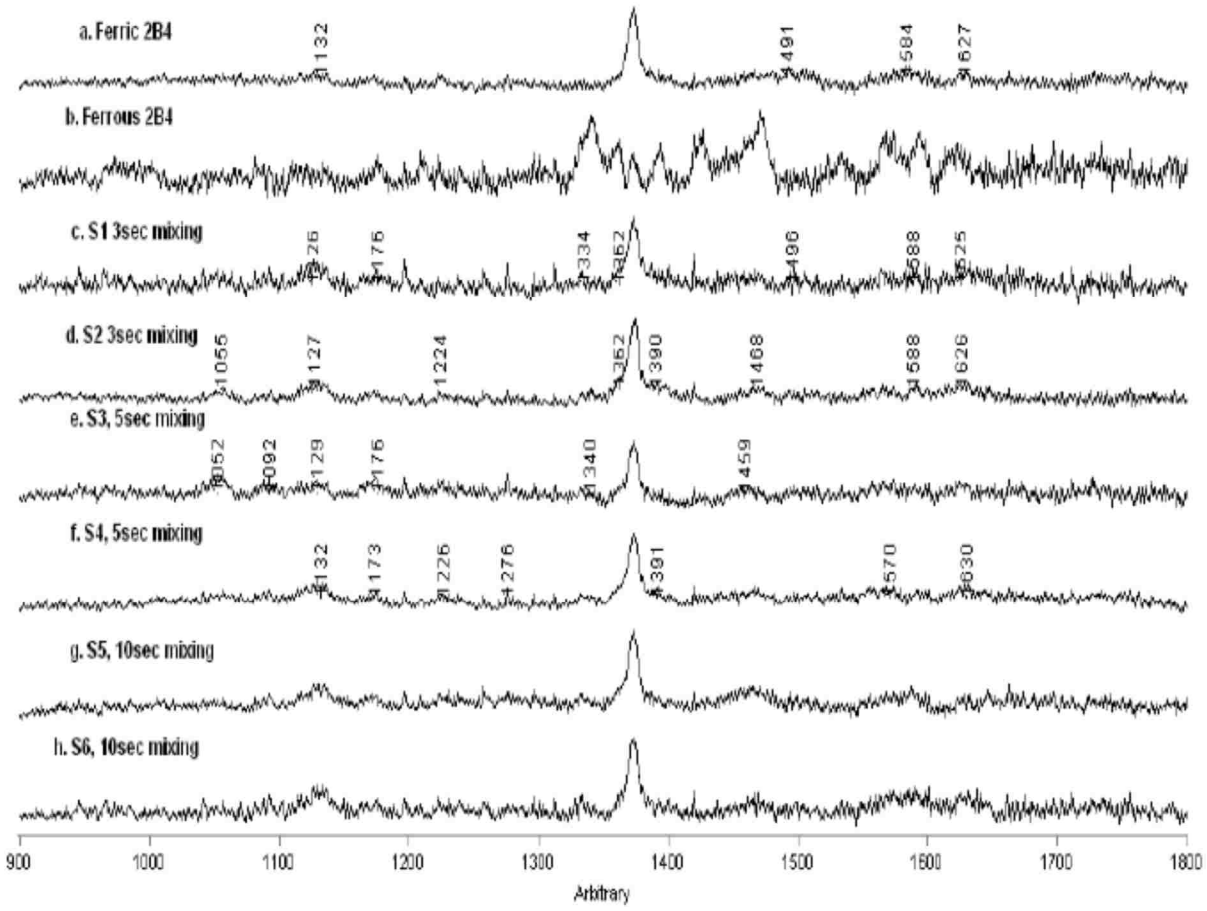

Figure 3.3.6 The high frequency RR spectra of CYP2B4 samples with different mixing time. The excitation wavelength is 413nm.

3.3.2.3 Optimization of adding dioxygen

Two options were considered for adding dioxygen, by mixing with oxygenated cold buffer solutions or exposing the solution to room temperature gaseous oxygen.

a. Adding oxygen saturated buffer

In order to avoid bubbling the protein solution and to possibly allow faster mixing, it was decided to add oxygen saturated buffer into the ferrous protein solution rather than direct bubbling of oxygen into the solution. Glycerol was used as a biological cryoprotectant, since it could help biological macromolecules maintain their structure in aqueous solutions of glycerol. Thus, all the solutions we used included 30% glycerol. The volume of the oxygen saturated buffer to protein solution was 1:1. The mixing time was 10sec by vortex. The oxy-CYP2B4 was successfully made. The RR spectra of oxy-CYP2B4 were shown in Figure 3.3.7. In the Figure, the stretching modes of O-O are seen 1138 and 1128cm^{-1} for $^{16}O_2$ sample in H_2O buffer which down shift to 1070 and 1060 cm^{-1}, in the spectrum of $^{18}O_2$ sample. The band at ~1340cm^{-1} corresponded to the ν_4 of ferrous CYP2B4 or P420 protein. Since the intensity of ν (O-O) band is smaller than expected, we think is there enough oxygen in the buffer.

The glycerol in buffer decreased the solubility of oxygen. The two tables shown in Table 3.1 showed the solubility of oxygen in glycerol solutions. The α_0 is the solubility of oxygen in water and the α_i is the solubility of oxygen in glycerol solution. For example, if the glycerol is 15.23% (wt) in the solution, the relative oxygen solubility is 0.8 at 15^o C. When the temperature decreases, the solubility of oxygen gas should increase. So the relative solubility of oxygen in 15% (wt) in the low temperature solution should be higher than 0.8[145]. In our case, 30% glycerol was employed. Thus, there was not enough oxygen dissolved in the buffer for making oxy-CYP2B4.

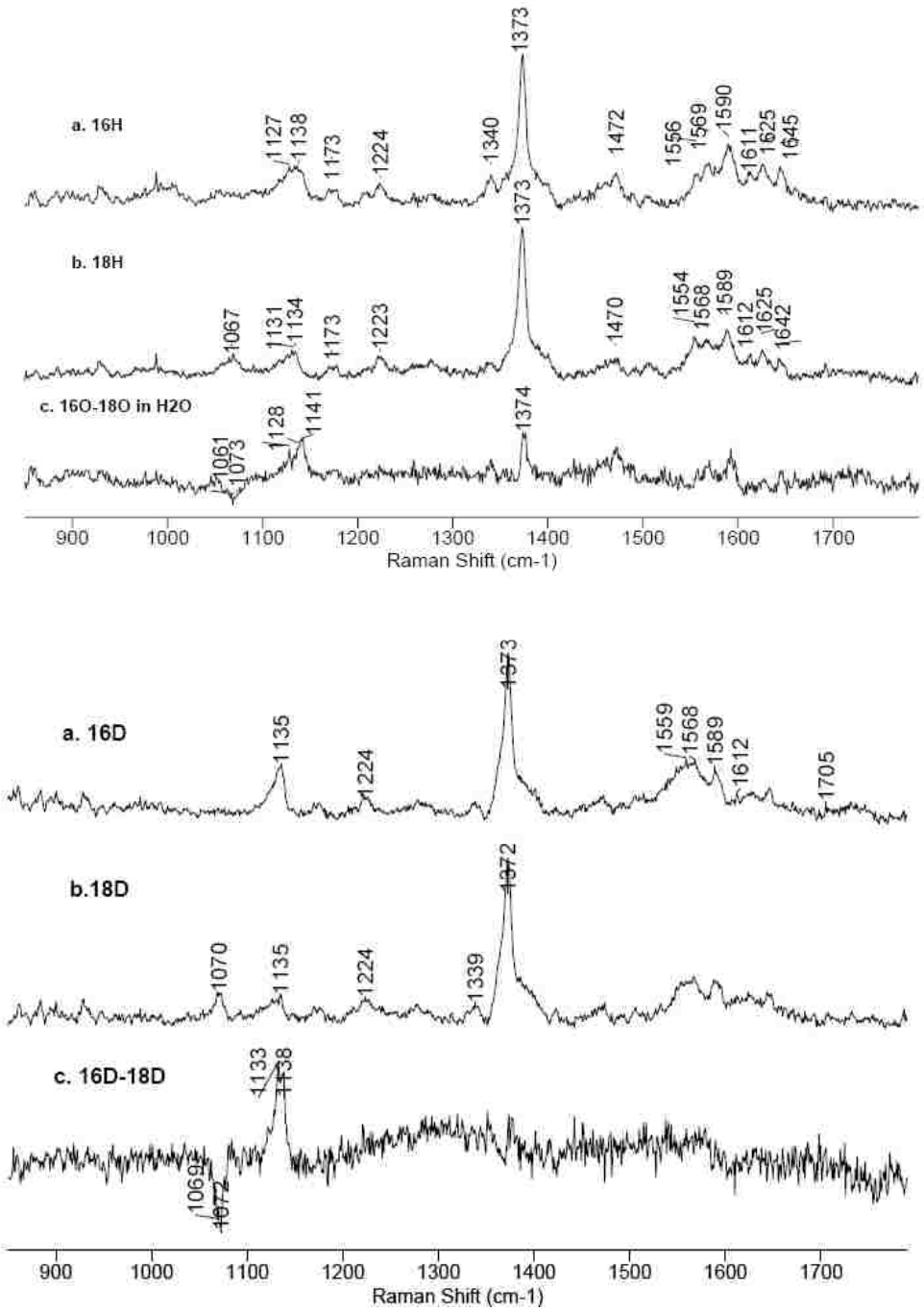

Figure 3.3.7 The high frequency RR spectra of oxy-CYP2B4 samples made by adding oxygen saturated buffer. The excitation wavelength is 413nm.

Table 3.1 The solubility of oxygen in water and glycerol solution [145]:

Table I. Oxygen Solubilities in Water

temp, °C	α_0 obsd[a]	α_0 lit.[b]	rel dev, %
15.0	0.0338	0.0342	−1.2
25.0	0.0279	0.0284	−1.8
37.0	0.0235	0.0240	−2.1

Table III. Relative Oxygen Solubilities (α_i/α_0) in Glycerol Solutions and Coefficients K_i (Eq 2)

concn, wt %	α_i/α_0 15.0 °C	25.0 °C	37.0 °C
1.31	0.982	0.971	0.983
2.52	0.973	0.967	0.978
3.74	0.973	0.953	0.961
6.16	0.943	0.931	0.935
9.18	0.880	0.902	
12.21	0.847	0.873	
15.23	0.808	0.844	
18.26	0.770	0.815	0.853
10^4K_i, L g^{-1}	5.77	4.74	4.07[a]

b. Adding oxygen gas

In order to increase the yield of oxy-CYP2B4, 5mL oxygen gas was added to the chilled ferrous CYP2B4 directly. The oxy-samples were measured by RR spectroscopy and the spectra are shown in Figure 3.3.8 left. As discussed under results, these conditions were the optimum found.

3.3.3 Spectroscopic results for oxy-CYP2B4

3.3.3.1 Wild-type CYP2B4

Figure 3.3.8 and 3.3.9 are the rR spectra of the oxygenated wild-type CYP2B4 with BHT in high- and low- frequency region, respectively. The band at ~1375cm^{-1} is assigned

ν_4 mode in the Figure 3.3.8. The $\nu(^{16}O\text{-}^{16}O)$ mode seems broad and can be seen as an overlap of two modes upon expansion (right), with frequencies estimated as 1130 and 1136cm^{-1}. They downshift to 1065 and 1071cm^{-1} in the ^{18}O samples. One ν(O-O) mode is sensitive to the H_2O/D_2O buffer exchange since the band at 1065 cm^{-1} upshift to 1067cm^{-1} upon D_2O buffer exchange. The finally obtained high-quality data for oxygenated wild-type CYP2B4 are similar in behavior with that of CYP101 and its D251N mutant.

The ν(Fe-O) mode of wild-type CYP2B4 appears at 535cm^{-1} and downshifts to 507 cm^{-1} upon $^{18}O_2$ substitution as shown in Figure 3.3.9. It shows the expected 28 cm^{-1} shifts upon $^{18}O_2$ substitution. Thus, the data of ν(Fe-O) mode are in reasonable agreement with other oxygenated P450s; i.e., comparable to the low frequency data for CYP101 and its D251N mutant, the ν(Fe-O) mode is at ~537cm^{-1} in D251N mutant and ~540 cm^{-1} in P450cam, respectively [30,128].

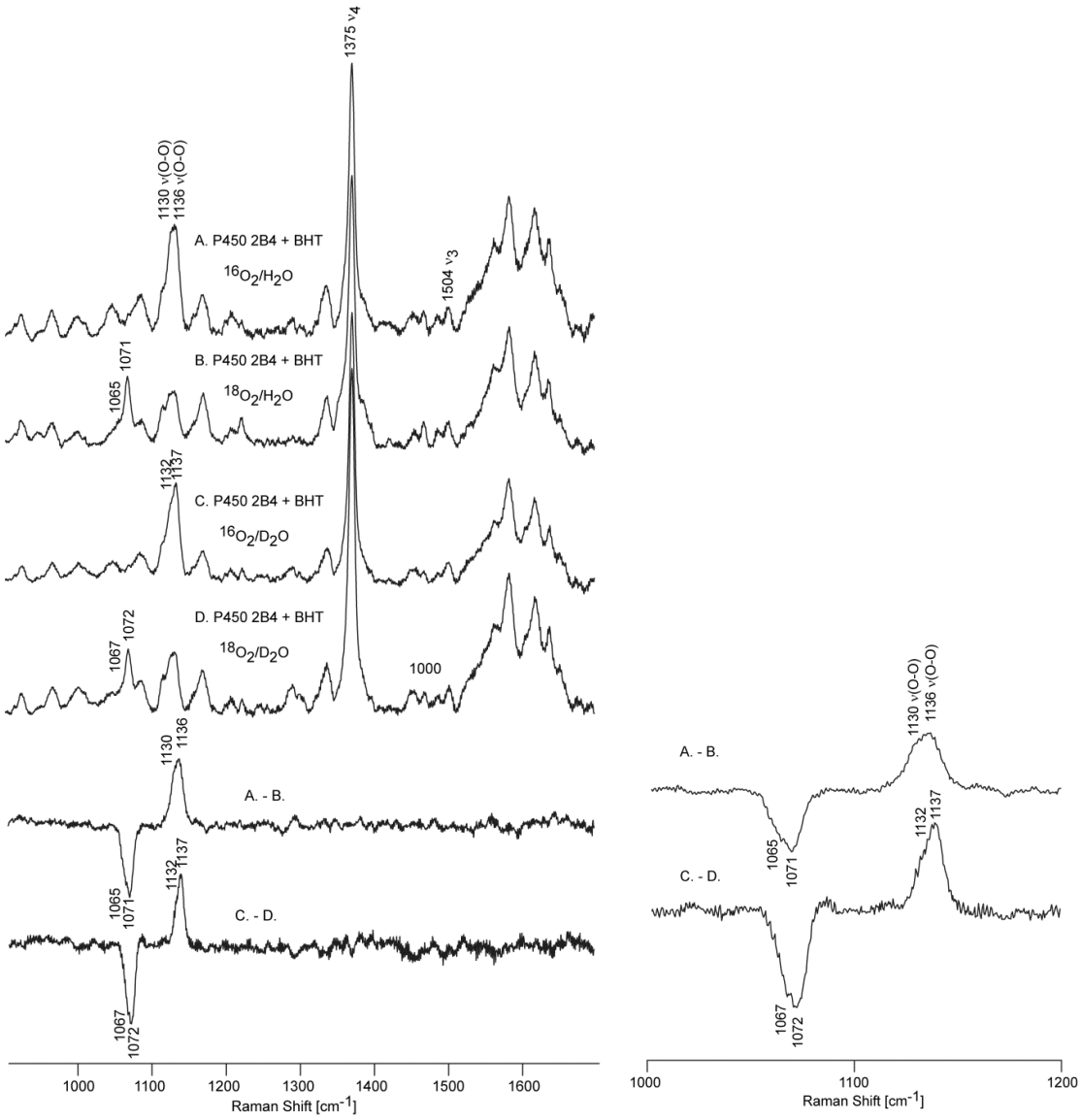

Figure 3.3.8 The high frequency rR spectra of oxy-CYP2B4 samples which made of adding oxygen gas. The excitation wavelength was 415nm.

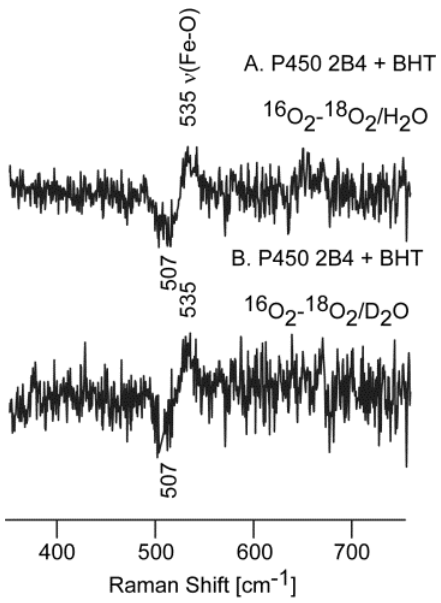

Figure 3.3.9 The low frequency different spectra of oxy-CYP2B4 samples which made of adding oxygen gas. The excitation wavelength was 415nm.

3.3.3.2 Results for oxygenated CYP2B4 mutants

As mentioned in the induction part, two CYP2B4 mutants were selected to study the oxygen activation intermediates, E301Q and F429H. These two mutants are unstable and easily denature in reduced form even at -25ºC. Even at -25ºC, more than 50% of F429H mutant evidently became P420 within 2 minutes [126]. It is more difficult to prepare oxygenated E301Q and F429H mutant of CYP2B4 than the wild-type.

The E301Q mutant was more stable than F429H mutant but less stable than wild-type CYP2B4. The oxy-complex spectra are shown in Figure 3.3.10. One ν_4 mode was at 1375 cm^{-1}, with a shoulder at 1367cm^{-1}, likely unresolved 1362 cm^{-1} feature, the latter indicating some conversion to P420 in the mutants. The presence of the ν(O-O) mode in the mutant is evident, but the intensity was less than it in wild-type CYP2B4. Thus, the

concentration of oxygenated protein was much less than expected. However, in the isotope difference spectra, the *v*(O-O) modes were more clear. There are also two modes, 1137 and 1126 cm^{-1} which exhibited the expected ~65 cm^{-1} shift upon $^{18}O_2$ substitution.

The ferrous F429H mutant is unstable and converted to P420 very quickly, even at -25ºC, up to now preventing preparation and rR characterization of its oxy-complex. Very recently it has been considered that in previous efforts in our lab to prepare oxygenated F429H mutant misinterpretations of the absorption spectra may have led to the false conclusions about the contents of the P420 form of the reduced ferrous derivative. Further efforts to secure oxygenated samples of the F429H mutant are ongoing in our laboratory.

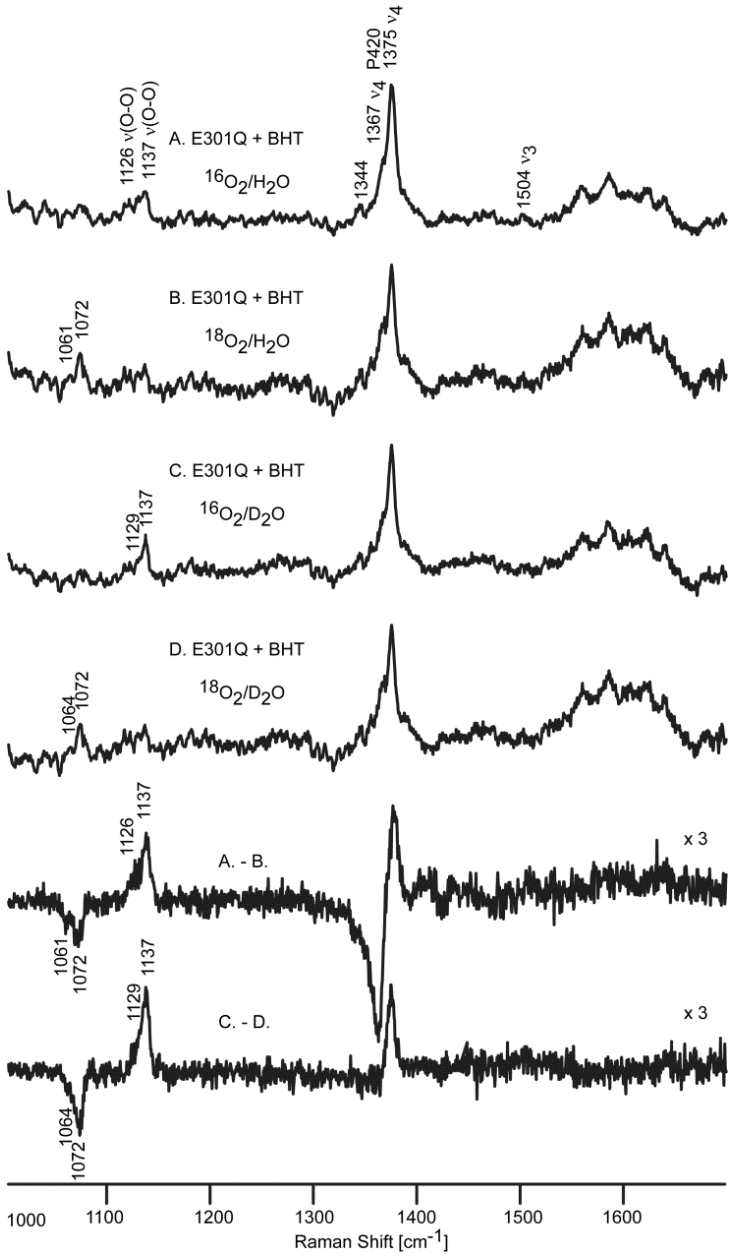

Figure 3.3.10 High frequency rR spectra of oxy-CYP2B4 E301Q mutant samples which made of adding oxygen gas. The excitation wavelength is 415nm.

3.3.3.3 The effects of cytochrome b5 binding to the dioxygen adduct of CYP2B4

As summarized in Section 3.1.1, the interaction of CYP2B4 with cytochrome b5 impacts function, raising interest in determining the structural basis for such effects. Earlier studies by our group showed that rR spectroscopy is well suited to explore these effects and studies are undertaken here to interrogate the dioxygen adduct. The rR spectra acquired for the oxygenated CYP2B4/apo-cytb5 complex are shown in Figure 3.3.11.

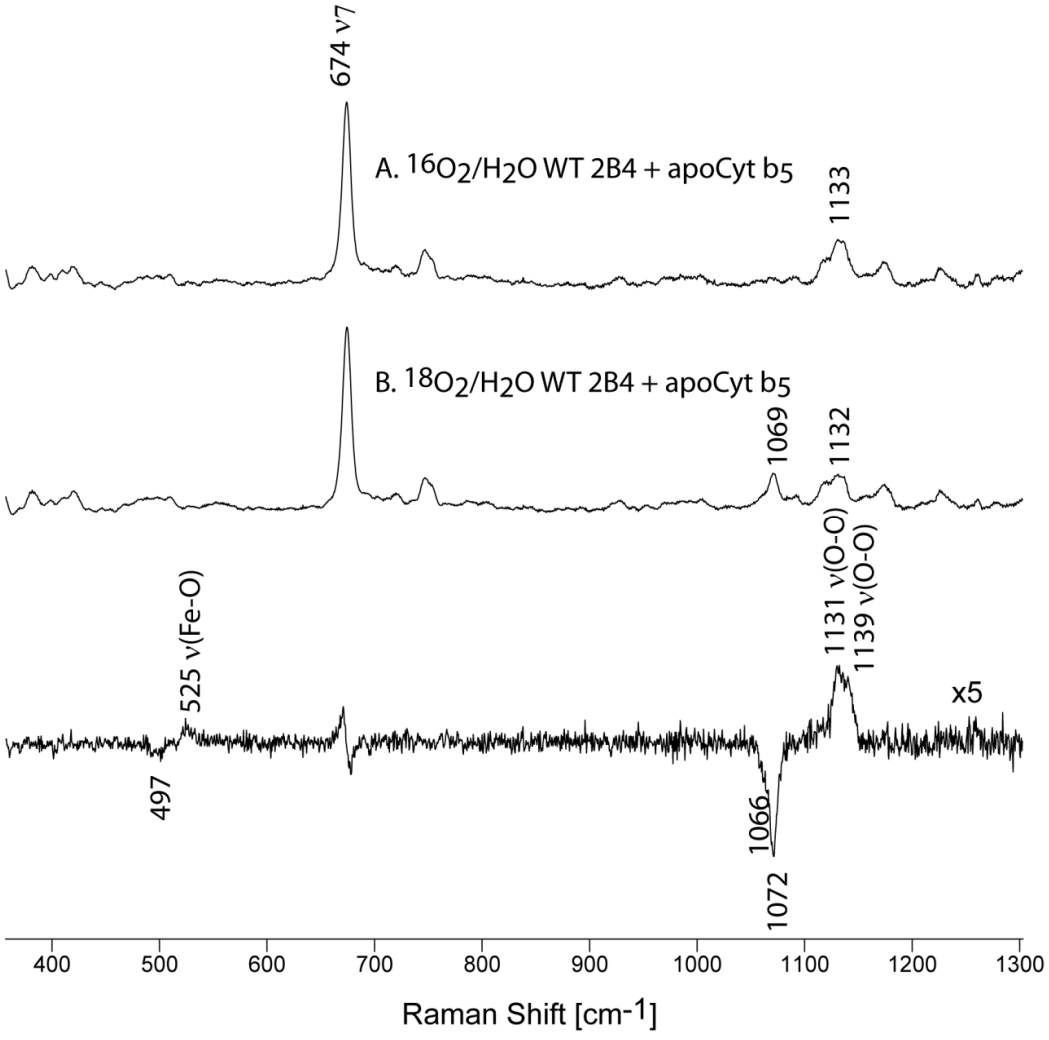

Figure 3.3.11 RR spectra of the oxygenated adduct of CYP2B4/apocytb5 complex

In comparison to the rR spectra acquired for the dioxygen adduct of free CYP2B4 (Figure 3.3.11), the lower frequency ν(O-O) mode is more intense for the CYP2B4/apocytb5 complex. While this can possibly be attributed to a stronger H-bonding interaction in the distal pocket, it is important to consider that cytb5 binding is on the proximal side and may exert its influence through changes in the proximal Fe-S linkage. In fact, it is noted that this interaction causes an ~ 10 cm^{-1} lowering of the ν(Fe-O) mode, from 535 cm^{-1} (Figure 3.3.3..1.2) to 525 cm^{-1}.

3.4. Conclusions

The rR measurements of oxygenated wild-type CYP2B4 samples provided by collaborators failed because of quick auto-oxidation. Methods were made in our laboratory to maximize mixing efficiency, resulting in successful preparation and rR spectral characterization of the WT CYP2B4 and one mutant. To our knowledge, these are the first successful rR measurements for drug metabolizing P450s. Building on that success, it also proved possible to acquire rR spectra of the oxygenated adduct of CYP2B4 in complex with cytochrome b5 redox partner, which showed a significant effect on the status of the Fe-O-O fragment. The next step is cryoreduction of oxy-complexes of these important compounds.

Bibliography

1. Bertini, I.; Gray, H. B.; Stiefel, E. I.; Valentine, J. S.; *Biological Inorganic Chemistry*, University Science Book; 1 edition; October 30, **2006**.
2. Shaik .S.; Visser, S. P. D.; *Cytochrome P450: Structure, Mechanism, and Biochemistry;* Montellano P. R. O. D. Ed.; Kluwer Academic/ Plenum Publishers, New York, **2004**, pp. 45-85.
3. Antonini, E.; Brunori, M.; *Hemoglobin and myoglobin in their reactions with ligands*, North-Holland, Amsterdam, **1971**.
4. Collman, J.P.; Boulatov, R.; Sunderland, C. J.; Fu, L.; *Chem. Rev.,* **2004,** *104,* 561-588.
5. Springer, B. A.; Olson, J. S.; Phillips, Jr., G. N.; *Chem. Rev.* **1994**, *94,* 699-714.
6. James P. Collman, Roman Boulatov, Christopher J. Sunderland, and Lei Fu, *Chem. Rev.* **2004,** *104,* 561-588.
7. Batabyal, D.; Yeh, S.-R.; *J. Am. Chem. Soc.*, **2007**, *129*, 15690-15701.
8. Evgenov, O. V.; Pacher, P.; Schmidt, P. M.; Hasko, G.; Schmidt, H. H. H. W.; Stasch, J-P..; *Nature Reviews Drug Discovery,* **2006**, *5*, 755-768.
9. Knowles, R. G.; Palacios, M.; Palmer, R. M. J.; Moncada, S.; *Proc. Natl. Acad. Sci. USA*, **1989**, *86*, 5159-5162.
10. Deinum, Geurt; Stone, James R.; Babcock, Gerald T.; Marletta, Michael A.; *Biochemistry*, **1996**, *35*, 1540-7.
11. Rosca, Florin; Kumar, Anand T. N.; Ye, Xiong; Sjodin, Theodore; Demidov, Andrey A.; Champion, Paul M.; *J. Phys. Chem. A* ; **2000**, *104*, 4280-4290.
12. Ikuta, Tohru; Ausenda, Sabrina; Cappellini, Maria D.; *Proc. Natl. Acad. Sci. USA,* **2001**, *98,* 1847-1852.
13. Hussain, M.B.; MacAllister, R. J.; Hobbs, A. J.; *American Journal of Physiology*, **2001**, *280*, 1151-1159.
14. Denninger J. W., Marletta, M. A.; *Biochim. Biophys. Acta*, **1999**, *1411*, 334-350.
15. Graham-Lorence, S.; Peterson, J. A.; *FASEB*, **1996**, *10*, 206-14.
16. Proniewicz, L. M.; Kincaid, J. R.; *Coordination Chemistry Reviews*, **1997**, *161*, 81-127.
17. Shimada, H.; Sligar, S.G.; Yeom, H.; Ishimura, Y.; *Catalysis by Metal Complexes*, **1997**, *19*, 195-221.
18. Denisov, I. G.; Makris, T. M.; Sligar, S. G.; Schlichting, I.; *Chemical Reviews*, **2005**, *105*, 2253-2277.
19. Loew, Gilda H.; Harris, Danni L.; *Chemical Reviews*; **2000,** *100*, 407-419.
20. Sun, Y.; Zeng, W.; Benabbas, A.; Ye, X.; Denisov, I.; Sligar, S. G.; Du, J.; Dawson, J. H.; Champion, P. M.; *Biochemistry*; **2013**, *52*, 5941-5951.
21. Yoshioka, S.; Tosha, T.; Takahashi, S.; Ishimori, K.; Hori, H.; Morishima, I.; *J. Am. Chem. Soc.,***2002**, *124*, 14571-14579.
22. Garfinkel, D.; *Arch. Biochem. Biophys.* **1958**, *77*, 493–509.
23. Klingenberg, M.; *Arch. Biochem. Biophys,.* **1958**, *75*, 376–386.
24. Lewis, D. F. V.; Eddershaw, P. J.; Dickins, M.; Tarbit, M. H.; Goldfarb, P. S.; *Chemico-Biological Interactions*, **1998**, *115*, 175-199.

25. Sigel, A.; Sigel, H.; Sigel, R. K. O.; *"The Ubiquitous Roles of Cytochrome P450 Proteins", in Metal Ions in Life Sciences*; John Wiley & Sons, Ltd, **2007**.
26. Les, A. M.; Lecomte, J. T. J. In *Protein Families*; Orengo, C.; Bateman, A., Eds.; 2014; pp. 207–235.
27. Guengerich, F. P. *Chem. Res. Toxicol.* **2008**, *21*, 70–83.
28. Oohora, K.; Hayashi, T. *Curr. Opin. Chem. Biol.* **2014**, *19*, 154–161.
29. Akhtara, M.; Wrightb, J. N.; Lee-Robichaud, P.; J. Steroid Biochemistry Molecular Biology **2011**, *125*, 2–12
30. Denisov, I. G.; Mak, P. J.; Makris, T. M.; Sligar, S. G.; Kincaid, J. R.; *J. Phys. Chem. A,* **2008**, *112,* 13172–13179.
31. Song, W. N.; Ryu, Y. O.; Ju, W. *J. Biol. Inorg. Chem.* **2004**, *9*, 654–660.
32. Montellano, O. de. *Cytochrome P450: Structure, Mechanism, and Biochemistry*; Kluwer Academic/Plenum Publisher, New York, 2005.
33. Champion, P. M. *Biological Applications of Raman Spectroscopy*; John Wiley and Sons: New York, 1988; pp. 249–292.
34. Rittle, J.; Green, M. T. *Science.* **2010**, *330*, 933–937.
35. Denisov IG, Grinkova YV, Sligar SG. Methods Mol Biol. 2012;875:375-91. doi: 10.1007/978-1-61779-806-1_20.
36. Denisov IG， Physical inorganic chemistry: principles, methods and models.2010, 109-142
37. Kappl, R.; Hoehn-Berlage, M.; Huettermann, J.; Bartlett, N.; Symons, M. C. R.; *Biochim. Biophys. Acta*, **1985**, *827*, 327-343.
38. Davydov, R.; Ledbetter-Rogers, A.; Martasek, P.; Larukhin, M.; Sono, M.; Dawson, J.H.; Masters, B.S.S.; Hoffman, B.M.; *Biochemistry*, **2002**, *41*, 10375–10381.
39. Davydov, R.; Razeghifard, R.; Im, S.-C.; Waskell, L.; Hoffman, B.M.; *Biochemistry*, **2008**,*47*, 9661–9666.
40. Davydov, R.; Sudhamsu, J.; Lees, N.S.; Crane, B.R.; Hoffman, B.M.; *J. Am. Chem. Soc.*, **2009**, *131*, 14493–14507.
41. Garcia-Serres, R.; Davydov, R.M.; Matsui, T.; Ikeda-Saito, M.; Hoffman, B.M.; Huynh, B.H. *J. Am. Chem. Soc.*, **2007**, *129*, 1402–1412.
42. Davydov, R.; Macdonald, I. D. G.; Makris, T. M.; Sligar, S. G.; Hoffman, B. M. *J. Am. Chem. Soc.* **1999**, *121*, 10654-10655.
43. Davydov, R.; Makris, T. M.; Hoffman, V.; Werst, D. E.; Sligar, S. G.; Hoffman, B. M. *J. Am. Chem. Soc.* **2001**, *123*, 1403-1415.
44. Gantt, S.L.; Denisov, I.G.; Grinkova, Y.V.; Sligar, S.G.; *Biochem. Biophys. Res. Commun.*, **2009**, *387*, 169–173.
45. Newcomb, M.; Hollenberg, P. F.; Coon, M. J.; *Arch. Biochem. Biophys.,* **2003**, *409*, 72-79.
46. Larkin, P.; *Infrared and Raman Spectroscopy: Principles and Spectral Interpretation*, **2011**, Elsevier, 15-17.
47. *Comprehensive Coordination Chemistry II From Biology to Nanotechnology*; McCleverty, J. A., Meyer, T. J., Eds.; Elsevier: New York, **2004**, *2*, 121 - 129.
48. Nakamoto, K.; *Infrared and Raman Spectra of Inorganic and Coordination Compounds*; Wiley, New York, **1997**, *Contents of Part A, Section A*, 319-318.
49. Que, Jr. L.; *Physical Methods in Bioinorganic Chemistry*; University Science Books, **2000**, 59-120.

50. Spiro, T. G.; Czernuszewicz, R. S., *Methods Enzymol*., **1995**, *246,* 416-460.
51. Champion, P. M. *Biological Applications of Raman Spectroscopy*; John Wiley and Sons: New York, **1988**; 249–292.
52. Piotr J. Mak, Daniel Kaluka, Munyaradzi Edith Manyumwa, Haiqing Zhang, Tianjing Deng, James R. Kincaid, *Biopolymers*, **2008**. *89*, *11*, 1045-1053
53. P. M. Champion, B. R. Stallard, G. C. Wagner, I. C. Gunsalus, *J.Am. Chem. Soc.* **1982**, *104*, 5469 – 5472.
54. Piotr J. Mak, Y-t Yang, S Im, L Waskell, James R. Kincaid, *Angew. Chem. Int. Ed.* **2012**, *51*, 10403-10407
55. S. A. Usanov, A. A. Gilep, T. A. Sushko*, Biochim. Biophys. Acta Proteins Proteomics* **2011**, *1814*, 200–209.
56. A. P. Mathieu, J. G. LeHoux, R. J. Auchus, Biochim. Biophys. Acta Gen. Subj. **2003,** *1619*, 291–300.
57. Y. V. Grinkova, I. G. Denisov, M. R. Waterman, M. Arase, N. Kagawa, S. G. Sligar, *Biochem. Biophys. Res. Commun*. **2008**, *372*, 379–382.
58. J. Wang, D. J. Stuehr, M. Ikeda-Saito, D. L. Rousseau, *Biol. Chem*., **1993**, *268*, 22255-22258.
59. B. Fan, J. Wang, D. J. Stuehr, D. L. Rousseau, *Biochemistry* 1**997**, *36*, 12660-12665.
60. J. Wang, D. J. Stuehr, D. L. Rousseau, *Biochemistry* **1997,** *36*, 4595-4606.
61. Piotr J. Mak, H. Zhang, P. F. Hollenberg, James R. Kincaid, *J. Am. Chem. Soc.* **2010**, *132,* 1494-1495
62. Michael Gregory, Piotr J. Mak, Stephen G. Sligar, James R. Kincaid, Angew. Chem. Int. Ed. *2013*, **52**, 5342-5345
63. T. G. Spiro, A. V. Soldatova, G. Balakrishnan, Coord. *Chem. Rev.* **2013**, *257*, 511–527.
64. Piotr J. Mak, Ilia G. Denisov, Doreen Victoria, Thomas M. Makris, Tianjing Deng, Stephen G. Sligar, James R. Kincaid , *J. Am. Chem. Soc*.**. 2007**,*129*, 6382-6383
65. Leibl, W.; Nitschke, W.; Huettermann, J.*, Biochim. Biophys. Acta*, **1986**, *870*, 20-30.
66. Yatsunyk, L. A.; Mendoza, O.; Mergny, J.-L.; *Acc. Chem. Res*., **2014**, *47*, 1836-1844.
67. TOMONAGA , T.; LEVENS, D.; Proc. Natl. Acad. Sci. USA, **1996**, *93*, 5830-5835.
68. Saiki, R. K.; Scharf, S.; Faloona, F.; Mullis, K. B.; Horn, G. T.; Erlich, H. A.; Arnheim, N.; *Science*, **1985**, *230*, 1350-1354.
69. ELISE A. R., FASEB, 1991, 5, 46-54.
70. Ravindranath, V.; Boyd, M.R. *Drug Metab. Rev.,* **1995**. *27*, 419 – 448.
71. Strobel, H.W.; Thompson, C.M.; Antonovic, L.; *Curr. Drug Metab.*, **2001**, *2*, 199 – 214.
72. Lawrie, R. A.; *Nature*, **1951**, *167*, 802-804.
73. Oldfield, T.J.; Smerdon. S.J.; Dauter, Z.; Petratos. K.; *Biochemistry*, **1992**, *31*, 8732-8739.
74. Choi, S.; Spiro, T. G.; Langry, K. C.; Smith, K. M.; Budd, D. L.; La Mar, G. N.; *J. Am. Chem. Soc.,* **1982**, 1*04*, 4345-4351.
75. Tomita, T.; Hirota, S.; Ogura, T.; Olson, J. S.; Kitagawa, T.; *J. Phys. Chem. B.,* **1999**, *103*, 7044-7054.
76. Hirota, S.; Li, T.; Phillips, G. N. Jr.,; Olson, J. S.; Mukai, M.; Kitagawa, T.; *J. Am. Chem. Soc,*. **1996**, *118*, 7845-7846.

77. Morikis, D.; Champion, P. M.; Springer, B. A.; Sligar, S. G. *Biochemistry*, **1989**, *28*, 4791-4800.;
78. Nishimura, R.; Shibata, T.; Ishigami, I.; Ogura, T.; Tai, H.; Nagao, S.; Matsuo, T.; Hirota, S.; Shoji, O.; Watanabe, Y.; Imai, K.; Neya, S.; Suzuki, A.; Yamamoto, Y. *Inorg. Chem.*, **2014**, *53*, 1091-1099.
79. Copeland, D. M.; West, A.H.; Richter-Addo, G.B.; *Protein*, **2003**, *53*,182-192.
80. Coyle, C. .; Vogel, K. M.; Rush, T. S.; Kozlowski, P. M.; Williams, R.; Spiro, T. G.; Dou, Y.; Ikeda-Saito, M.; Olson, J. S.; Zgierski, M. Z.; *Biochemistry*, **2003**, *42*, 4896-4903.
81. Ibrahim, M.; Denisov, I. G.; Makris, T. M.; Kincaid, J. R.; Sligar, S. G. *J. Am. Chem. Soc,*. **2003**, *125*, 13714-13718.
82. Terner, J.; Palaniappan, V.; Gold, A.; Weiss, R.; Fitzgerald, M. M.; Sullivan, A. M.; Hosten, C. M. *J. Inorg. Biochem.,* **2006**, *100*, 480-501.
83. Behan, R. K.; Green, M. T. J. *Inorg. Biochem*., **2006**, *100*, 448-459.
84. Hersleth, H.-P.; Uchida, T.; Rohr, A. K.; Teschner, T.; Schuenemann, V.; Kitagawa, T.; Trautwein, A. X.; Goerbitz, C. H.; Andersson, K. K.; J. *Biol.Chem.*, **2007**, *282*, 23372-23386.
85. Decatur, S. M.; Belcher, K. L.; Richert, P. K.; Franzen, S.; Boxer, S. G.; *Biochemistry*, **1999**, *38*, 11086-11092.
86. Choi, S.; Spiro, T. G.; Langry, K. C.; Smith, K. M.; Budd, D. L.; La Mar, G. N.; *J. Am. Chem. Soc.*, **1982**, *104*, 4345-4351.
87. Banushkina, P.; Meuwly, M.; *Phys. Chem. B.*, **2005**, *109*, 16911-16917.
88. Rwere F.; Mak P. J.; Kincaid J.; *Biochemistry*, **2008**, *47*, 12869-12877.
89. Morikis, D.; Champion, P. M.; Springer, B. A.; Sligar, S. G. Biochemistry, 1989, 28, 4791-4800.;
90. Nishimura, R.; Shibata, T.; Ishigami, I.; Ogura, T.; Tai, H.; Nagao, S.; Matsuo, T.; Hirota, S.; Shoji, O.; Watanabe, Y.; Imai, K.; Neya, S.; Suzuki, A.; Yamamoto, Y. Inorg. Chem., 2014, 53, 1091-1099.
91. Copeland, D. M.; West, A.H.; Richter-Addo, G.B.; Protein, 2003, 53,182-192.
92. Coyle, C. .; Vogel, K. M.; Rush, T. S.; Kozlowski, P. M.; Williams, R.; Spiro, T. G.; Dou, Y.; Ikeda-Saito, M.; Olson, J. S.; Zgierski, M. Z.; Biochemistry, 2003, 42, 4896-4903.
93. Leibl, W.; Nitschke, W.; Huettermann, J., Biochim. Biophys. Acta, 1986, 870, 20-30.
94. Bruker, E. A.; Olson, J. S.; Ikeda-Saito, M.; Phillips, G. N.; Proteins, 1998, 30, 352-356.
95. Collman, J. P.; Brauman, J. I.; Iveson, B. L.; Sessler, J. L.; Morris, R. M.; Gibson, Q. H. J. Am. Chem. SOC. 1983, 105, 3052-3064.
96. Collman, J. P.; Brauman, J. I.; Halbert, T. R.; Suslick, K. S. Proc. Natl. Acad. Sci. U.S.A. 1976, 73, 3333-3337.
97. Liao, M-S.; Huang, M-J.; Watts, J. D. Mol. Phys., 2012, 110, 3061-3076.
98. Bruker, E. A.; Olson, J. S.; Ikeda-Saito, M.; Phillips, G. N.; Proteins, 1998, 30, 352-356.
99. Sakakura, M.; Morishima, I.; Terazima, M.; Biochemistry, 2002, 41, 4837-4846
100. Li, T.; Quillin, M. L.; Phillips, G. N.; Olson, J. S.; Biochemistry, 1994, 33, 1433-1446.

101. Cameron, A. D.; Smerdon, S. J.; Wilkinson, A. J.; Habash, J.; Helliwell, J. R.; Li, T.; Olson, J. S.; Biochem., 1993, 32, 13061-13070.
102. Takano, T.; J. Mol. Biol., 1997, 110, 569-584.
103. Carver, T. E.; Brantley, R. E.;Singleton, E. W.; Arduini, R. M.; Quillin, M. L; Phillips, G. N., Jr.; Olson, J. S.; J. Biol. Chem., 1992, 267, 14443-14450.
104. Uchida, T.; Ishimori, K.; Morishima, I.; J. Biolog. Chem., 1997, 272, 30108-30114.
105. Ishikawa, H.; Takahashi, S.; Ishimori, K.; Morishima, I.; Biochem. Biophys. Res. Commun., 2004, 324, 1095-1100.
106. Smerdon, S. J., Krzwda, S., Wilkinson, A. J., Brantley, R. E., Jr., Carver, T. E., Hargrove, M. S., and Olson, J. S. Biochem., 1993, 32, 5132-5138.
107. Peterson, E. S.; Friedman, J. F.; Chien, E. Y. T.; Sligar, S. G.; Biochem., 1998, 37, 12301-12319.
108. Lloyd, E.; Burk, D. L.; Ferrer, J. C.; Maurus, R.; Doran, J.; Carey, P. R.; Brayer, G. D.; Mauk, A. G.; *Biochemistry*, **1996**, *35*, 11901-11912.
109. Shiro, Y.; Iizuka, T.; Mrubayashi, K.; Ogura, T.; Kitagawa, T.; *Biochemistry*, **1994**, *33*, 14986-14992.
110. Product manual of QuikChange II Site-Directed Mutagenesis Kit
111. Reid, L. S.; Lim, A. R.; Mauk, A. G. *J. Am. Chem. Soc.,* **1986**, *108*, 8197-8201.
112. Sherwood, C.; Mauk A. G.; Brayer, G. D.; *J. Mol. Biol.*, **1987**, *193*, 227.
113. Mauk, A. G.; Lloyd, E. *FEBS let.,* **1994**, *340*, 281-286.
114. Adachi, S.; Nagano, S.; Watanabe, Y.; Ishimori, K.; Morishima, I., *Biochem. Biophys. Res. Commun.*, **1991**, *180*, 138-144.
115. Ikeda-Saito, M.; Horill, H.; Andersson, L. A.; Prince, R. C.; Pickering, I. J.; George, G. N.; Sanders, C. R.; Lutz, R. S.; McKelvey, E. J.; Matter, R.; J Biol Chem., 1992, 267, 22843-22852.
116. Mak, P. J.; Podstawka, E.; Kincaid, J. R.; Proniewicz, L. M.; *Biopolymers*, **2004**, *75*, 217–228.
117. Wu, Y.; Chien, E. Y. T.; Sligar, S. G.; La Mar, G. N.; *Biochemistry*, **1998**, *37*, 6979-6990.

118. Coon, M. J., *Annu. Rev. Pharmacol. Toxicol.*, **2005**, *45,* 1-25.

119. Johnson, E. F.; Stout, C. D., *Biochem. Biophys. Res. Commun*., **2005,** *338*, 331–336.

120. Chen, Z; Ost, W. B; Schelvis, J. P. M. *Biochemistry* **2004**, *43*, 1798-1808.
121. Mak, P. J.; Im. S.- C.; Zhang, H.; Waskell, L. A.; Kincaid, J. R. *Biochemistry* **2008**, *47*, 3950 – 3963
122. Mak, P. J.; Denisov, I. G.; Grinkova, Y. V.; Sligar, S. G.; Kincaid, J. R. *J. Am. Chem. Soc.* **2011**, *133*, 1357-1366.
123. Zhang, H.; Myshkim, E; Waskell, L. *Biochem Biophys Res Commun* 2005 338, 499-506.
124. Zhang, H.; Im, S-C.; Waskell, L., *J. Biol. Chem.*, **2007**, *282*, 29766–29776.
125. Sheng, X.; Zhang, H.; Im, S-C.; Horner, J. H.; Waskell, L.; Hollenberg, P. F.; N. Martin, *J. Am. Chem. Soc.*, **2009**, *131*, 2971–2976.
126. Perera, R.; Sono, M.; Kinloch, R. Zhang, H.; Tarasev, M.; Im, S.-C.; Waskell, L.;

Dawson, J. H. *Biochim. Biophys. Acta,* **2001**, *1814*, 69-75.
127. Davydov, R.; Razeghifard, R.; Im, S.-C.; Waskell, L.; Hoffman, B. M. *Biochemistry,* **2008**, *47*, 9661-9666.
128. Sjodin, T.; Christian, J. F.; Macdonald, I. D. G.; Davydov, R.; Unno, M.; Sligar, S. G.; Hoffman, B. M.; Champion, P. M. *Biochemistry*, **2001**, *40*, 6852-6859.